Search for a heavy gauge boson in the decay channel $W' \to e\nu$ with the ATLAS experiment

von

Maurice Becker

Masterarbeit in Physik
vorgelegt dem Fachbereich Physik, Mathematik und Informatik (FB 08)
der Johannes Gutenberg-Univerität Mainz
am 3. September 2013

1. Gutachter: Prof. Dr. Stefan Tapprogge
2. Gutachter: Prof. Dr. Wolfgang Gradl

Ich versichere hiermit, dass ich die Arbeit selbstständig verfasst und keine anderen als die angegebenen Quellen und Hilfsmittel verwendet, sowie Zitate kenntlich gemacht habe.

Mainz, 3. September 2013

Maurice Becker
ETAP Mainz
Insitut für Physik Staudingerweg 7
Johannes Gutenberg-Universität D-55099 Mainz
mauriceb@students.uni-mainz.de

Contents

Kurzfassung

Titel der Arbeit: Suche nach einem schweren Eichboson im Zerfallskanal W'→eν mit dem ATLAS-Experiment

Das bisher erfolgreichste Modell, um den Aufbau der Materie zu beschreiben ist das Standardmodell der Teilchenphysik. Es beschreibt den Aufbau der Materie durch Quarks und Leptonen und deren Wechselwirkung durch drei fundamentale Kräfte: Die schwache Kraft, welche durch W- und Z-Bosonen vermittelt wird, die starke Kraft, übermittelt durch Gluonen und die elektromagnetische Kraft, die durch Photonen beschrieben wird. Zwar konnte es innerhalb des Standardmodells erreicht werden, dass die schwache und elektromagnetische Kraft innerhalb der elektro-schwachen Vereinheitlichung zusammen beschrieben werden, aber die große Vereinheitlichung, unter Hinzunahme der starken Kraft, ist bisher noch nicht gelungen. Theorien, die ein mögliches Modell einer solchen Vereinheitlichung bereitstellen, werden als sogenannte große vereinheitlichte Theorien bezeichnet. Einige von diesen Theorien sagen weitere, geladene, schwere Eichbosonen voraus, die auch als W'-Bosonen bezeichnet werden.
In dieser Arbeit wird eine Suche nach solchen Bosonen, die in ein Elektron und Neutrino zerfallen, präsentiert. Die dabei verwendeten Daten wurden mit dem ATLAS-Experiment im Jahr 2012 bei einer Schwerpunktsenergie von $\sqrt{s} = 8\,\text{TeV}$ aufgenommen und entsprechen einer integrierten Luminosität von $20\,\text{fb}^{-1}$. Auf die Daten werden bestimmte Selektionskriterien angewendet um sensitiv auf mögliche W'-Bosonen zu sein. Für eine Untergrundabschätzung von echten Elektronen, die nur auf Standardmodell Vorhersagen basiert, werden Monte Carlo Simulationen verwendet. Die verwendeten Monte Carlo Simulationen benutzen teilweise unterschiedliche Arten der Detektorsimulation, welche eingehend miteinander verglichen werden. Für den Untergrund, der durch falsch identifizierte Elektronen entsteht, wird eine datenbasierte Methode vorgestellt. Verschiedene Verteilungen dieser Untergründe werden mit den Daten verglichen und auf Unterschiede untersucht. Da keine signifikanten Unterschiede zwischen den Daten und dem Untergrund festzustellen sind, kann eine Ausschlussgrenze auf die Masse eines hypothetischen W'-Bosons gesetzt werden. Dazu wird ein Bayesianischer Ansatz verwendet, mit welchem die beobachtete und erwartete Ausschlussgrenze auf die Masse eines hypothetischen W'-Bosons auf 2.97 TeV bestimmt werden konnte.

1. Introduction

From the year one scientists are on the search for "whatever binds the world's innermost core together" [1]. The present model to describe the elementalary structure of matter is the Standard Model of particle physics. It does not only describe the fundamental particles, but also the interaction between them, including three of the four fundamental forces. Different predictions of the Standard Model are tested experimentally with very high precision and so far no significant differences were found. Although the Standard Model is very successful, it leaves some open questions, e.g. a description of the gravitational interaction or dark matter. Another open issue, that is not solved by the Standard Model, is the unification of the three forces, that are described by the Standard Model. Although it has been achieved to unify the electromagnetic and the weak force within the Standard Model, the great unification, that would include also the strong interaction, is not yet provided. Some of the theories, which try this unification, also called Grand Unified Theories (GUTs), predict new particles and (or) interactions at high energy scales. With the Large-Hadron-Collider (LHC), a proton-proton collider, it is possible to reach those high energies and search for physics beyond the Standard Model.
This thesis presents a search of a new, heavy, charged vector boson. Different theories predict such a vector boson, also referred as W'-boson. Some of them predict that the W'-boson couples different to quarks than to leptons, others, that it couples different to different generations, whereas this thesis focuses on a model that predicts a W'-boson with the same couplings as the Standard Model W-boson, but higher masses. The analysed data, that are used to perform the search, were taken with the ATLAS-detector from proton-proton collision at an invariant mass of $\sqrt{s} = 8$ TeV. The focus is set on the process, where the hypothetical W'-boson decays into an electron and a neutrino. In order to have a precise background estimation from Standard Model processes, Monte-Carlo simulations and also a data-driven method are used. No evidence for a W'-boson is found and therefore a limit on the mass of this hypothetical new vector boson is set.
In chapter 2 of the thesis, the theoretical fundamentals of the Standard Model and theories beyond it are shortly introduced. The third chapter provides an overview of the ATLAS-detector and relevant components for this analysis. It follows a chapter, which explains the reconstruction of electrons and missing transverse energy, the measurable quantity correspondent to the energy of the neutrino. Chapter 5 describes the criteria used to reduce the background. An explanation of Monte-Carlo simulations for the relevant processes is given in chapter 6, together with a comparison of two different methods of the detector simulation. In chapter 7 it is explained how the background of real electrons is estimated by using Monte-Carlo simulations and it is also described how the background from objects that fake electrons is estimated

by using a data driven-method. In the same chapter the comparison of data and total background is shown as well. Since no significant difference between data and background is found, in chapter 8 it is described how to set a limit on the mass of a hypothetical W'-boson.

2. Theoretical motivation

In the first section of this chapter an overview of the current Standard Model of particle physics is given, which describes the fundamental particles and their interactions. In section 2.2 the basic principles of processes, which occur at proton-proton collisions, are explained and section 2.3 gives a short summary of theories beyond the Standard Model, focusing on the so-called Sequential Standard Model (SSM).
In this thesis natural units are used, which means that $\hbar$ and c is set to one and therefore masses and momenta are given in units of energy, electron volts (eV).

2.1. The Standard Model of particle physics

At the moment the Standard Model of particle physics is the best known model to describe the structure of matter. Basically the known matter consists of two different sorts of elementary point like particles: leptons and quarks. Both of these particles belong to the family of fermions and thus have a half-integral spins. The interactions of these elementary particles are described with 3 fundamental forces: the electromagnetic, the weak and the strong force. The gravitational interaction is not described in the Standard Model, but for subatomic scales its strength is negligible compared with the other interactions. The three interactions described by the Standard Model are mediated through the exchange of a further fundamental group of particles, namely the gauge bosons, which carry an integral spin.
The photon (γ) acts as the carrier particle of the electromagnetic interaction and couples to the electric charge, but is itself uncharged. The range of the electromagnetic interaction is infinite but decreases with the distance, since the photon is a massless particle.
The weak interaction is mediated by three different gauge bosons: the electrically neutral Z-boson and the charged $W^{\pm}$-bosons, which couple to the third component of the weak isospin T_3. All three gauge bosons have a very high mass ($m_w \approx 80.4$ GeV, $m_Z \approx 91.2$ GeV) leading to a short lifetime and such to a short range of interaction.
The strong interaction is mediated by 8 different gluons, which couple to the so-called color charge. These color charge can be defined by three different colors: red, green, and blue as well as the correspondent anticolors. The gluons carry themselves color charge, which leads to self-coupling, meaning that gluons can couple to other gluons. Although the gluons are massless, the self-coupling leads to a very short interaction range. In table 2.1 an overview of all gauge bosons of the Standard Model is given.

The six leptons can be divided into three different families. Each family consists of a charged lepton and a corresponding neutrino, which does not have any electric,

Interaction	Boson	Mass [GeV]	couples to	rel. strength
strong	gluon (g)	0	color charge (r, g, b)	1
electromagnetic	photon (γ)	0	electric charge (e)	10^{-2}
weak	$W^{\pm}$	≈ 80.4	weak isospin (T_3)	10^{-6}
	Z	≈ 90.2		

Table 2.1.: Overview of the interactions and gauge bosons of the Standard Model of particle physics [2].

.

Generation	Name		T_3	el. charge	Mass
1.	electron	(e^-)	-1/2	-1	≈ 0.5 MeV
	electron neutrino	(ν_e)	+1/2	0	< 2 eV
2.	muon	(μ^-)	-1/2	-1	≈ 106 MeV
	muon neutrino	(ν_μ)	+1/2	0	< 0.19 MeV
3.	tau	(τ^-)	-1/2	-1	≈ 1777 MeV
	tau neutrino	(ν_τ)	+1/2	0	< 18.2 MeV

Table 2.2.: Overview of the three lepton families of the Standard Model. Given are the name, the third component of the isospin T_3, the charge and the masses [4].

but a weak charge. The charged leptons, electron (e), muon (μ) and tau (τ) can couple to the electromagnetic interaction as well as to the weak interaction, whereas the neutrinos only interact through the weak interaction. An overview of the leptons and their properties can be seen in table 2.2. The table shows that the mass of the charged particles increases with the family number.
In the Standard Model the neutrinos have no mass, although it is shown, for example with neutrino oscillation experiments, that they have a very small mass [3]. In addition to the shown leptons in the table, for each particle exists an antiparticle, which has the same mass but opposite (additive) quantum number.
Also the quarks can be split into three families, each containing two different flavored quarks. In table 2.3 all three families are shown together with the electric charge, the third component of the weak isospin and the mass. It can be seen that each family consists of a "up-type" quark with charge 2/3 and a "down-type" quark with charge -1/3. The masses increase with the family number but an explanation why this mass hierarchy is given as it is, is one question, the Standard Model provides no answer. Since the quarks carry charge color, they participate in the strong interaction. Quarks do not exist as free particles but as color neutral bound states, which can be split into two different groups: mesons, which contain one quark and one antiquark, and baryons, containing three quarks with three different colors. Baryons and mesons together are called hadrons.
Furthermore the heavy fermions are unstable and decay via the weak interaction into lighter fermions. The outcome of this is that the only known stable particles consist of the lightest fermions, but it is possible to produce the heavy one artificial, for example

Generation	Name		T_3	el. charge	Mass
1.	up	u	+1/2	+2/3	$\approx$ 2.3 MeV
	down	d	-1/2	-1/3	$\approx$ 4.8 MeV
2.	charme	c	+1/2	+2/3	$\approx$ 1.3 GeV
	strange	s	-1/2	-1/3	$\approx$ 95 MeV
3.	top	t	+1/2	+2/3	$\approx$ 173.1 GeV
	bottom	b	-1/2	-1/3	$\approx$ 4.2 GeV

Table 2.3.: Overview of the three quark families of the Standard Model. Given are the name, the third component of the isospin T_3, the charge and the masses. The values are taken from [4]

in accelerator experiments.

The Standard Model can be described as a gauge-invariant quantum field theory. The fermions are represented in such a theory by (dirac)-spinors (ψ), which are four-component column vectors and satisfy the Dirac equation for a free fermion:

$$(i\gamma^\mu \partial_\mu - m)\psi = 0 \ , \tag{2.1}$$

where γ_μ are the gamma matrices. This equation basically describes the dynamics of a free fermion. Using the Euler-Lagrange formalism the correspondent Lagrangian density, or short Lagrangian, is given by:

$$\mathcal{L} = \bar{\psi}(i\gamma^\mu \partial_\mu - m)\psi \, , \tag{2.2}$$

where $\bar{\psi} = \psi^\dagger \gamma^0$. If the field ψ is invariant under a symmetry then it can be transformed as (for the case of a U(1) symmetry):

$$\psi = e^{i\theta(x)}\psi \, , \tag{2.3}$$

where $\theta(x)$ is a real phase. This transformation is called global if $\theta(x)$ is constant for all x and local if $\theta(x)$ depends on x. The Dirac Lagrangian from equation 2.2 is invariant under global transformations but not under local transformation. Nevertheless it is possible to make the Lagrangian also invariant under local transformation by introducing a, ore in general case more than one, new vector field A_μ. For the case of the U(1) symmetry, this new vector field corresponds to the field representation of a photon. In principle this means, that the requirement of the Lagrangian, to be invariant under local transformation, generates new vector fields, which can be identified as the interactions described before. A beautiful characteristic of this formalism is, that the number of generators of the symmetry group, used for the local transformation, corresponds to the number of particles mediating the interaction. For example the number of generators for the $SU(3)$, which describes the strong interaction, is eight, which is the same number of existent gluons. Therefore the underlying gauge symmetry of the Standard model is a $SU(2) \times U(1) \times SU(3)$. The first part, $SU(2) \times U(1)$ describes the combination of the electromagnetic and weak interaction leading to four gauge bosons, γ, Z and $W^\pm$. The second part $SU(3)$ describes the strong interaction with eight different gluons.

2.1.1. Feynman Formalism

From the Lagrangian it is possible to derive the so-called Feynman rules [5]. These rules specify how to calculate the amplitude of a process, in which all the dynamical information is given. The reaction rate or cross-section can then be calculated by the usage of Fermi's golden Rule, which states that the probability of a process to happen is given by the product of the squared amplitude and the phase space. The phase space is thereby a purely kinematic factor, dependent on the energy, mass and momentum of the participants.
The Feynman rules can be visualized in so-called Feynman graphs. In such Feynman graphs the particles are represented by straight lines. Points, where three or more lines intersect are called vertices and lines connecting one vertex with another are called propagators. In figure 2.1 an annihilation of an electron-pair into a virtual photon is shown, which then decays into a muon-antimuon pair. In this case the propagator is a virtual one, because the photon has to "carry a mass" which is not the case for real photons. In this thesis the time axis is chosen to be the abscissa and the spacelike axis is the ordinate.
Particles are marked with arrows along the time axis. while antiparticles are marked with arrows against the time axis. At each of the two vertices an interaction takes place with an amplitude, which is proportional to the square root of the coupling constant. In this case it is an electromagnetic interaction leading to an overall amplitude, which is proportional to $\sqrt{\alpha_{em}} \times \sqrt{\alpha_{em}} = \alpha_{em}$. In general the amplitude of a process can be expressed as a series expansion of the coupling constant:

$$A = \sum_i \alpha^i A_i \tag{2.4}$$

where A_i indicates the sum of all contributing graphs to the order of $\mathcal{O}(\alpha^i)$. The graphs contributing to the lowest order of $\mathcal{O}(\alpha^i)$ are called leading order (LO), the second lowest order, next to leading order (NLO) and so on. Some contributing NLO graphs for the electron positron annihilation are given in figure 2.2. The top left of the figure shows an example of a so-called vertex correction, where a photon, emitted from the muon, is absorbed by the antimuon. The top right and bottom left show an example of real corrections, where the top right shows the final state radiation (FSR)

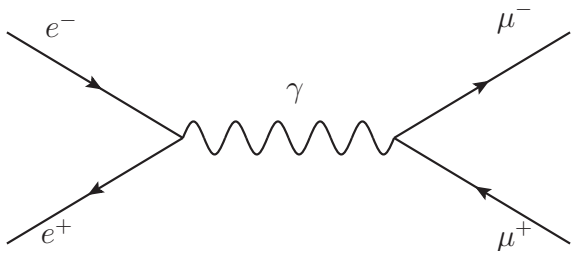

Figure 2.1.: Annihilation of an electron-positron pair into a photon, which then decays into a muon-antimuon pair.

and the bottom left the initial state radiation (ISR). An example of a (fermion) loop correction is given in the bottom, where the virtual photon decays into an fermion-antifermion pair which then again annihilates to a γ^*.
In principle the number of corrections is infinite, but higher order corrections have less influence since the terms, contributing to the amplitude will decrease with higher exponents of α.

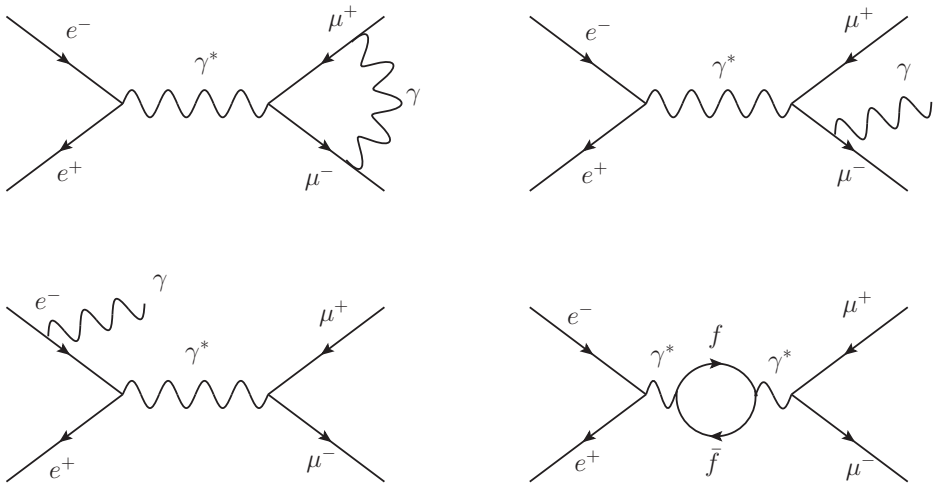

Figure 2.2.: Some of the Feynman graphs contributing to the NLO correction of the process $e^+e^- \to \gamma^* \to \mu^+\mu^-$. The top left shows a vertex correction, the top right is an example of FSR, the bottom left is an example of ISR and the bottom right a fermion loop correction.

2.1.2. The electroweak interaction

In the beginning of particle physics the electromagnetic and the weak interaction were considered separately. An unification of this theories was then given by Gashow, Salam and Weinberg [6] which described the electromagnetic and weak interaction as an manifestation of one fundamental interaction. It is based on the introduction of the weak isospin (T) as a new quantum number. It is constructed in a way, that the weak interaction only couples to the third component of the weak isospin. Taken into account that the weak interaction only couples to left handed [7] [1] particles it is possible to group the left handed fermions in doublets with $T = 1/2$ and $T_3 = \pm 1/2$ and the right handed into an isospin singlet with $T = 0$ and $T_3 = 0$. The connection between the weak and the electromagnetic interaction is done by introducing the weak hyper charge (Y). This hypercharge is connected with the electromagnetic charge (Q)

[1] The handedness is given by the chirality of the particles, which is the same as the helicity, the projection of the spin to the momentum, for massless particles.

via the Gell-Mann-Nishijima formula [8]:

$$Q = T_3 + \frac{1}{2}Y \tag{2.5}$$

The isospin operators $T_i = \sigma_i/2$, where σ_i are the Pauli matrices, generate together with the hypercharge the underlying $SU(2) \times U(1)$ group [9]. The isospin operators are associated with three bosonic vector fields $W^a_\mu, a = 1, 2, 3$ and the hypercharge with a singlet field B_μ. With the requirement of gauge invariance the Lagrangian can be formulated as:

$$\mathcal{L} = -\frac{1}{4}W^a_{\mu\nu}W^{\mu\nu,a} - \frac{1}{4}B_{\mu\nu}B^{\mu\nu} + \sum_j \bar{\psi}^L_j i\gamma^\mu D_\mu \psi^L_j + \sum_{j,\sigma} \bar{\psi}^R_{j\sigma} i\gamma^\mu D_\mu \psi^R_{j\sigma}\,, \tag{2.6}$$

where $\psi^{L(R)}$ is the left (right)-handed fermion field, j runs over the generations and σ is the component of the doublet (e.g. flavour in case of quarks). D_μ is given by the covariant derivative:

$$D_\mu = \partial_\mu - ig_2 T_a W^a_\mu + ig_1 \frac{Y}{2} B_\mu\,, \tag{2.7}$$

which contains the coupling constants g_2 for the weak interaction and g_1 for the electromagnetic interaction. The field strength tensors $W^a_{\mu\nu}$ and $B_{\mu\nu}$ contain the vector fields $W^a_\mu, a = 1, 2, 3$ and B_μ. An expression for the charged W bosons of the weak interaction is given by a linear combination of W^1_μ and W^2_μ:

$$W^\pm_\mu = \frac{1}{\sqrt{2}}(W^1_\mu \mp iW^2_\mu)\,. \tag{2.8}$$

One property of the charged bosons $W^\pm$ is that interactions where they participate can lead to a change of the quark flavour and change of the quark generation. A theoretical description of this behavior is given by the CKM-Matrix formalism [4]. The square of the absolute elements of the CKM-matrix, $|V_{ij}|^2$, yield the probability that a quark with flavour i transforms to a quark with flavour j under emission of a W boson. This holds only for the case of a charged boson and not for neutral, e.g. Z, bosons.
The connection between the Z boson, the photon and the electroweak vector fields is given through the weak mixing angle θ_W:

$$\begin{pmatrix} Z_\mu \\ A_\mu \end{pmatrix} = \begin{pmatrix} \cos\theta_W & \sin\theta_W \\ -\sin\theta_W & \cos\theta_W \end{pmatrix} \begin{pmatrix} W^3_\mu \\ B_\mu \end{pmatrix} \tag{2.9}$$

Since the $SU(2)$ is a non-Albelian group it is possible that the different W^a_μ vector fields couple with each other and thus also a coupling between the W,Z and γ bosons of the weak interaction is possible. The electroweak mixing angle is connected to the electric charge by:

$$e = g \cdot \sin\theta_W\,. \tag{2.10}$$

The local gauge invariance requires the vector fields W_μ^a to be massless. This is contrast to the experimental observation, where the W and Z bosons have a mass in the order of $\mathcal{O}(100\text{ GeV})$. In order to solve this problem it is possible to spontaneous break the $SU(2) \times U(1)$ symmetry by introducing a complex scalar doublet field:

$$\Phi(x) = \begin{pmatrix} \phi_+(x) \\ \phi_-(x) \end{pmatrix} . \tag{2.11}$$

The coupling to the electroweak gauge fields is given by the Higgs Lagrangian:

$$\mathcal{L}_H = (D_\mu \Phi)^+ (D^\mu \Phi) - V(\Phi) , \tag{2.12}$$

with the Higgs potential:

$$V(\Phi) = -\mu^2 \Phi^+ \Phi + \frac{\lambda}{4} (\Phi^+ \Phi)^2 , \, \lambda > 0 . \tag{2.13}$$

This potential is constructed in a way that Φ has a degenerated ground state. By choosing the ground state to be:

$$< \Phi > = \frac{1}{\sqrt{2}} \begin{pmatrix} 0 \\ v \end{pmatrix} \text{ with } v = \frac{2\mu}{\sqrt{\lambda}} , \lambda > 0 \tag{2.14}$$

the $SU(2) \times U(1)$ symmetry is spontaneously broken. Expanding Φ around the vacuum expectation value, v, it follows:

$$\Phi(x) \approx \frac{1}{\sqrt{2}} \begin{pmatrix} 0 \\ v + H(x) \end{pmatrix} . \tag{2.15}$$

$H(x)$ is a neutral scalar field, which can be identified as the Higgs boson [10] with a mass $m_H = \mu\sqrt{2}$. The Higgs boson was observed in July 2013 by ATLAS [11] and CMS [12]. By insertion of this field into the Lagrangian it follows for the mass terms of the bosons:

$$m_\gamma = 0 \quad m_W = \frac{1}{2} v g_2 \tag{2.16}$$

$$m_z = \frac{1}{2} \sqrt{g_1^2 + g_2^2}\, v \tag{2.17}$$

For the electroweak mixing angle it follows:

$$\cos\theta_W = \frac{M_W}{M_Z} . \tag{2.18}$$

With this relation and equation 2.10 it is possible to check if the theory matches the data. The value of the mixing angle is measured to $\sin^2\theta_W = 0.233 \pm 0.004(\text{exp.}) \pm 0.005(\text{theor.})$ [13] and so far there are no differences found to the theory prediction. The masses of the fermions can be explained in a similar way by a Yukawa coupling [14] to the scalar Higgs field.

2.1.3. Strong interaction

The theoretical description of the strong interaction is given by the Quantum Chromodynmaics (QCD). The underlying $SU(3)_C$ [2] has 8 generators, which can be represented by the Gell-Mann matrices λ^1, ..., λ^8 [8]. They satisfy the commutation relations:

$$\left[\lambda^a, \lambda^b\right] = 2if^{abc}\lambda^c \tag{2.19}$$

with f^{abc} as fully antisymmetric structure constants [15]. Under the requirement of local $SU(3)_C$ transformations it follows for the Lagrangian:

$$\mathcal{L}_{QCD} = -\frac{1}{4}G_a^{\mu\nu}G^a_{\mu\nu} + \sum_f \bar{q}_f(i\gamma^\mu D_\mu - m_f)q_f\,, \tag{2.20}$$

with the covariant derivative:

$$D^\mu = \partial^\mu - i\alpha_s\frac{\lambda^a}{2}G_a^\mu(x)\,. \tag{2.21}$$

G_a^μ represents thereby the eight different gluons. The index f of the sum runs over all quark flavours and α_s is the QCD coupling constant. In the first term of the Lagrangian the field strength tensors

$$G_a^{\mu\nu} = \partial^\mu G_a^\nu - \partial^\nu G_a^\mu + \alpha_s f^{abc}G_b^\mu G_c^\nu \tag{2.22}$$

are introduced and represent the self-coupling of gluons.

It is also possible for the QCD to visualize processes by Feynman graphs. Figure 2.3 shows in the top two leading order processes. On the top left side a $q\bar{q} \to g \to q\bar{q}$ process is shown with quarks as in- and outgoing fermions and a gluon as propagator. The top right side shows a gluon vertex, where three gluons couple with each other. In the bottom of figure 2.3 two NLO corrections are shown, where on the left side a fermion and on the right side a gluon loop is given.

By calculating such loop corrections, using the Feynman rules, divergent integrals of the form $\int d^4k(1/k^2)$, where k is the momentum can occur. In order to get these divergences solved it is possible to use the principle of dimensional regularization [16]. The calculation of the integral is expanded to $D = 4 + 2\epsilon\,, \epsilon > 0$ dimensions, which leads to a well-defined integral, that can be split in a divergent and a non divergent part. The not divergent part has a momentum (q) dependence, whereas the divergent part is momentum independent, but both parts have a dependency on an arbitrary energy scale μ.

It is possible to absorb the divergent part of the integral into the coupling constant, leading to a μ dependence. For the experiment this means that the measured coupling constant is not the bare but the *renormalized* one.[3]

[2] C stands for color

[3] In the case of QED it can be said that it is not the bare charge which is measured but the screened one due to virtual e^+e^- pairs (loop corrections).

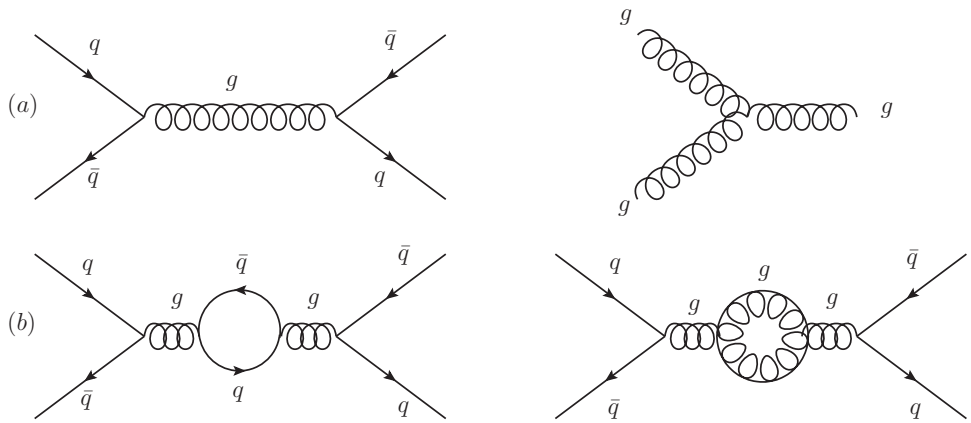

Figure 2.3.: In (a) are two leading order QCD Feynman graphs shown, where on the left side a $q\bar{q} \to g \to q\bar{q}$ process is shown and the right side is an example for the gluon gluon coupling. In (b) is on the left a NLO fermion loop correction and on the right side a gluon loop correction shown.

The introduced scale μ is arbitrary and not physically motivated so that the measurable quantities, like the cross-section, have to be μ independent. This is given if every loop correction on every order is taken into account, resulting in an infinite sum. If this is done in a finite way the μ dependence does not vanish but will get lower as more correction order are taken into account and can be interpreted as a theoretical uncertainty.
Looking at the $Q^2 = -q^2$ dependence of α_s it is given that α_s is small for high Q^2, which corresponds to small distances. This is caused by the self-coupling of the gluons and is also named "asymptotic freedom" because the quarks can act as quasi-free particles and can be described perturbatively (in orders of α_s). Going to lower energy scales (longer distances) α_s increases rapidly. It other words this means, if it is tried to separate two quarks from each other, the spent energy is transformed into the production of a new quark-antiquark pair leading to color neutral hadrons. This process is called hadronization and the fact that no free quarks are existent is called *confinement*.
Since α_s has such a Q^2 dependence it is often referred as *running* coupling constant[4]. The LO Q^2-dependence of α_s is given by:

$$\alpha_s(Q^2) = \frac{\alpha_s(Q_0^2)}{1 - \frac{\beta_1 \alpha_s(Q_0^2)}{2\pi} \ln(Q^2/Q_0^2)}\,, \qquad \beta_1 = \frac{2N_f - 33}{6}\,, \tag{2.23}$$

with Q_0 as an energy scale, where α_s is known and N_f as number of quarks with masses $m_q^2 < Q^2$. The factor β_1 is given by the lowest order coefficient of the so-called

[4]This can be applied also to the masses of particles used in the renormalization process, leading to a *running* mass. But in most time a given mass refers to the so-called pole mass, which is given by the resonance in a, for example, scattering amplitude measurement.

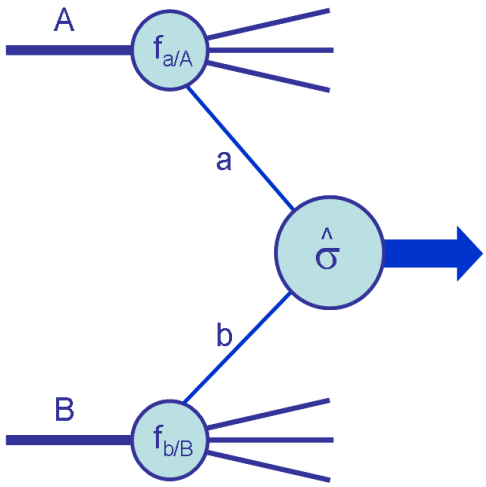

Figure 2.4.: Schematic view of a pp-collision. The incoming protons are marked with A and B. The parton distribution function of the protons is given by $f_{a/A}$ and $f_{b/B}$. The partons of the hard scattering process, a and b, interact with a cross-section $\hat{\sigma}$ [18].

β-function. The β-function predicts the energy scale dependence of α_s. Equation 2.23 demonstrates the asymptotic freedom for $Q^2 \to \infty$, where $\alpha_s \to 0$ if $N_f < 17$. For Q^2 values below $\Lambda_{QCD} \approx 200$ MeV [17] α_s rises above 1. A typical energy scale for α_s is the one of the Z-mass: $\alpha_s = 0.1184 \pm 0.0059$.

2.2. Phenomenology of proton-proton collisions

In the previous section it was explained that quarks cannot exist as free particles, they form color neutral hadrons – mesons and baryons. The proton is one of these baryons, it contains two u- and one d-quark. These, so-called valence quarks, interact through gluons with each other, whereas the gluons can convert to quark-antiquark pairs which again can annihilate into a gluon. The quarks produced due to this fluctuation are called sea-quarks. Though the proton is not a particle consisting of three static quarks but rather a dynamical formation of valence, sea-quarks and gluons. Gluons, valence and sea- quarks are also called partons.

The LHC is a proton-proton collider and thus it is more complicated to interpret the result of such a collision as it is for example for a $e^+ - e^-$ collider. Not the protons as whole collide but the partons out of the protons. The interaction of these partons is also called hard scattering process. In figure 2.4 a schematic pp-collision is shown. The incoming protons A and B contain the two partons a and b, which carry a momentum of $x_a q_A$ and $x_b q_B$, where $q_{A/B}$ is the momentum of the proton and thus x_a and x_b can be interpreted as fraction of the proton momentum, carried by the parton a, b. The probability to find partons with such an momentum fraction is given

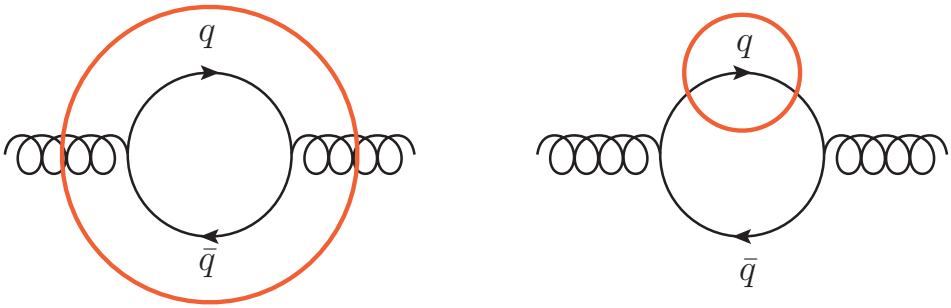

Figure 2.5.: Schematic sketch of vacuum polarization inside the proton. The red circle indicates the resolution corresponding to a certain Q^2. On the left side of the figure the resolution is not big enough to resolve the quarks from the vacuum polarization, whereas on the right the Q^2 is big enough to do so.

by the **p**arton **d**istribution **f**unction (PDF) of the protons, $f_{a/A}(x_a)$ and $f_{b/B}(x_b)$. Furthermore $\hat{\sigma}$ is the cross-section of the hard scattering process.
It was shown from S.Drell and T.-M. Yan by the factorisation theorem [19] that it is possible to separate the proton proton cross-section into two parts: one perturbative part for the hard scattering process $\hat{\sigma}_{ab\to X}(x_a, x_b)$ and the other (not perturbative) part is given through the PDFs. This is leading to a cross-section:

$$\sigma_{AB} = \sum_{a,b} \int dx_a \int dx_b f_{a/A}(x_a) f_{b/B}(x_b) \hat{\sigma}_{ab\to X}(x_a, x_b)\,. \tag{2.24}$$

Interactions between partons of the protons, that do not participate in the hard scattering process lead also to, typically low energetic, hadrons. The parts of a pp-collision containing these hadrons is an so-called *underlying event* which contaminates the hard process.

2.2.1. Parton distribution function

The parton distribution functions describe the momentum distribution inside a proton ($f_P(x, Q^2)$). They are dependent on the Bjorken's scale variable x, which is equivalent to the fraction of the proton momentum carried by a parton if the transverse momentum and rest masses is small. The Q^2 dependence of the PDFs can be explained by the higher spatial resolution which is gained with higher Q^2. A schematic picture to demonstrate this effect is shown in figure 2.5. It can be seen on the left side that the resolution, marked by the red circle, is not high enough to resolve the vacuum polarization. For a higher Q^2 it is then possible to resolve a quark from the vacuum polarization, shown on the right side of the figure.
If the PDFs are known at one scale it is possible to predict the evolution of the momentum dependence though the the so-called DGLAP-equations [20] [21] [22] . The

proton-proton cross-section can then be written as:

$$\sigma_{AB} = \sum_{a,b} \int dx_a \int dx_b f_{a/A}(x_a, \mu_F^2) f_{b/B}(x_b, \mu_F^2) \hat{\sigma}_{ab\to X}(x_a, x_b)\,. \tag{2.25}$$

with μ_F as factorization scale which can be understood as the transition from big to small distances. The cross-section is in principle independent on the choice of the scale since the scale dependence is compensated by coefficients of the DGLAP equation, similar to α_s described in section 2.1.3. If all corrections are taken into account the scale dependence would vanish completely but since this is not possible, due to limited calculation time, different choices of μ_F will lead to different PDFs, which can be interpreted as a theoretic uncertainty.

Determination of Parton Distribution Functions

It is not possible to give a theoretical prediction of the PDFs over the whole x- range. So the most common way is to determine these with fits to data including several free parameters. For the parametrization a certain Q^2 scale has to be chosen, which is often in the order of $\mathcal{O}(1\ \text{GeV}^2)$. Using the DGLAP equations the scale dependence of the ansatz can be evolved. Then it is possible to use, for example, a cross-section measurement of the Drell-Yan process ($pp \to Z/\gamma^* + X \to e^+e^- + X$) to determine the parameters of a PDF by evolving it to the scale of the Z pole mass.
The fitting is done with a convolution of the PDF and the partonic amplitude from the hard scattering process. If the amplitude includes LO (NLO,NNLO) calculations than the resulting PDF is also referred to as LO (NLO,NNLO). For this fitting data from several experiments are used in order to get a precise measurement of the PDF parameters over a large x and Q^2 range. One of the precisest measurements for predominantly low x were done by H1 [23] and ZEUS [24]. For higher x ranges fixed target experiments lead with DIS[5] measurements to precise results [25]. Since it depends on which parametrization is chosen for the PDFs it exists different sets of PDFs. Often used PDFs are provided by MSTW [26] or CTEQ [27].
The fitting procedure leads also to an uncertainty due to data uncertainties. Since the single parameters of a PDF can be correlated with each other it is not possible to propagate these parameter uncertainties to observable, for example the cross-section, without any further regard. Therefore the fit parameters are transformed into an orthogonal eigen basis using the Hessian approach [28]. Then the fit parameters can be varied independently. This variations are done by shifting each parameter up and down by a value corresponding to either 68% C.L[6] or 90% C.L. leading to a set of $2n$ PDFs per confidence level, where n represents the number of fitparameter. With these variations an uncertainty of, for example, the cross-section can be given due to the PDF fit uncertainty.
In figure 2.6 the MSTW2008NNLO PDF for a proton is shown for different scales,

[5] **D**eep **I**nelastic **S**attering
[6] **C**onfidence **L**evel

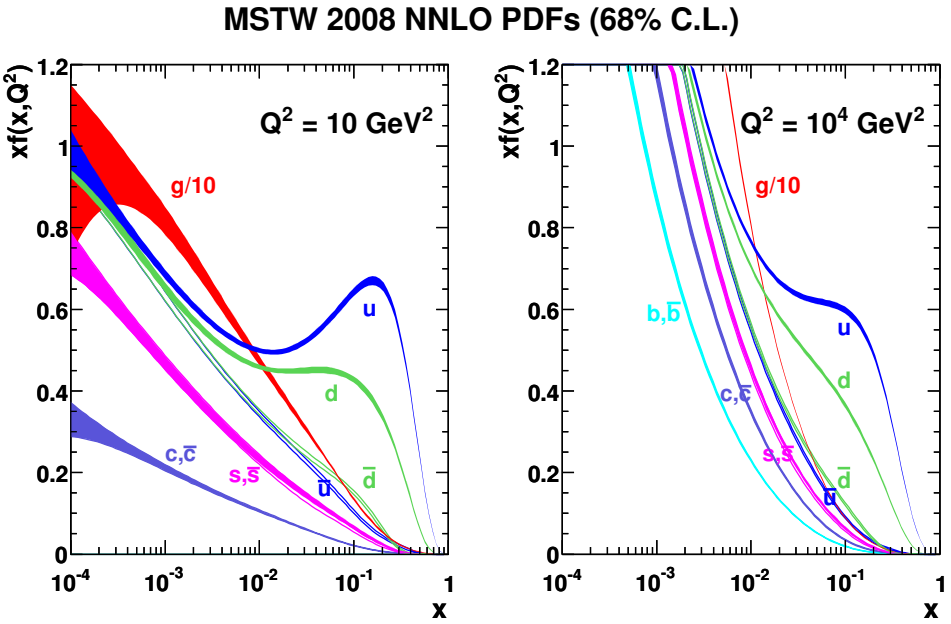

Figure 2.6.: MSTW2008NNLO PDF times x as a function of x for $Q^2 = 10$ GeV^2 on the left side and $Q^2 = 10^4$ GeV^2 on the right side.

$Q^2 = 10$ GeV^2 and $Q^2 = 10^4$ GeV^2. In both plots it can be seen that for high values of x the contribution of the valence quarks dominates, whereas for low x the sea-part dominates. It is also shown that in case of the higher scale the contribution of sea quarks increases because at this scale it is more probable to resolute the gluon splitting.

2.2.2. Charged current Drell-Yan process

The charged current Drell-Yan process is the charged analog to the neutral Drell-Yan process [19]. In this process a quark and an other flavoured antiquark annihilate into a W bosons which then decays into a lepton and a neutrino: $q_i\bar{q}_j \to W^\pm \to l^\pm \overset{(-)}{\nu}_l$. In figure 2.7 the Feynman graph for the decay into a positron and neutrino is shown. The cross-section of this process is given by [29]:

$$\hat{\sigma}(q_i\bar{q}_j \to e^+\nu_e) = \frac{G_F^2|V_{ij}|^2}{18\pi} \frac{M_W^4}{(\hat{s} - M_W^2)^2 + M_W^2\Gamma_W^2}\,, \tag{2.26}$$

where G_F^2 is the Fermi constant, V_{ij} an element of the CKM-matrix and $\hat{s}$ the squared center of mass energy of the incoming quarks. According to that, the cross-section is a Breit-Wigner-distribution with the maximum at the value of the W- boson mass and the width Γ_W.

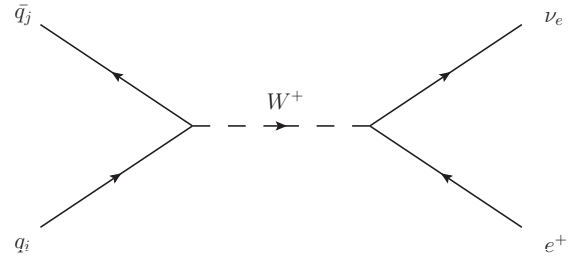

Figure 2.7.: Leading order Feynman graph for $q_i\bar{q_j} \to e^+\nu_e$.

The center of mass energy is also equal to the invariant mass of the positron and neutrino:

$$\sqrt{\hat{s}} = m_{e^+\nu_e} = \sqrt{(p_{e^+} + p_{\nu_e})^2}\,, \tag{2.27}$$

where p is the momentum four vectors of the positron or the neutrino. By usage of the relation between the partonic center of mass energy and the center of mass energy of the protons

$$\hat{s} = x_{q_i} x_{\bar{q_j}} s \tag{2.28}$$

it follows for the four momenta of the quarks:

$$p_{q_i} = \frac{\sqrt{s}}{2}\begin{pmatrix} x_{q_i} \\ 0 \\ 0 \\ x_{q_i} \end{pmatrix}, \qquad p_{\bar{q_j}} = \frac{\sqrt{s}}{2}\begin{pmatrix} x_{\bar{q_j}} \\ 0 \\ 0 \\ -x_{\bar{q_j}} \end{pmatrix}. \tag{2.29}$$

With this four momenta the so-called rapidity is given by:

$$y_{e^+\nu_e} = \frac{1}{2}\log\left(\frac{x_{q_i}}{x_{\bar{q_j}}}\right) \tag{2.30}$$

leading to:

$$x_{q_i} = \frac{m_{e^+\nu_e}}{\sqrt{s}} e^{y_{e^+\nu_e}}\,, \qquad x_{\bar{q_j}} = \frac{m_{e^+\nu_e}}{\sqrt{s}} e^{-y_{e^+\nu_e}} \tag{2.31}$$

For a certain value of $m_{e^+\nu_e}$, for example the W-boson mass, different values of y correspond to different values of x. In figure 2.8 the dependence between different (x,Q^2) pairs and the kinematic variables M (invariant mass) and y is shown for different experiments. It can be seen that the DIS experiments are able to reach low Q^2 values compared to the LHC setup. The LHC can reach high values of x and Q^2 leading to high sensitivities for cross-section measurements above the Z-resonance.

Since neutrinos interact only via the weak force, they do not interact with the detector and therefor it is not possible to reconstruct their four momenta. Nevertheless it is possible to determine the transverse component of the three momentum and the angle

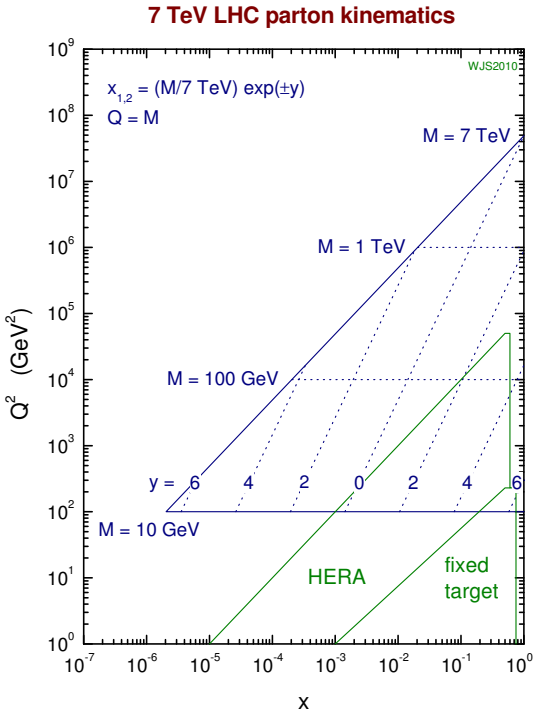

Figure 2.8.: Schematic plot to illustrate the kinematic coverage of LHC with a center of mass proton energy of 7 TeV, HERA and fix target experiments. Shown is the x, Q^2 plane together with different invariant masses and correspondent rapidity, y, values.

between the electron and the neutrino in the transverse plane. Therefore a variable is defined which consists only of these measurable quantities and has information about the invariant mass. It is called transverse mass and is defined as:

$$m_T = \sqrt{2p_T^e p_T^{\nu_e}(1 - \cos(\phi_{e\nu}))}\,, \tag{2.32}$$

where p_T is the momentum of the electron or neutrino projected to the transverse plane and $\phi_{e\nu}$ the angle between electron and neutrino also in the transverse plane. The maximum of m_T is the invariant mass and is reached if the angle between electron and neutrino is π (also called back-to-back decay). In figure 2.9 the transverse mass is shown for a simulation of the described charged Drell-Yan process. The blue distribution shows the typical rising behavior from low m_T values up to the mass of the W-boson($\approx$80 GeV). At this point the so-called Jacobian peak is visible, which has a very sharp edge to higher m_T values. Also added in the figure is in red a second distribution, where the p_T of the electron is smeared by 20% to illustrate the impact of a detector resolution. It can be seen that also the Jacobian peak is "smeard" out, leading to less events in the peak and more events in the low and high m_T tails.

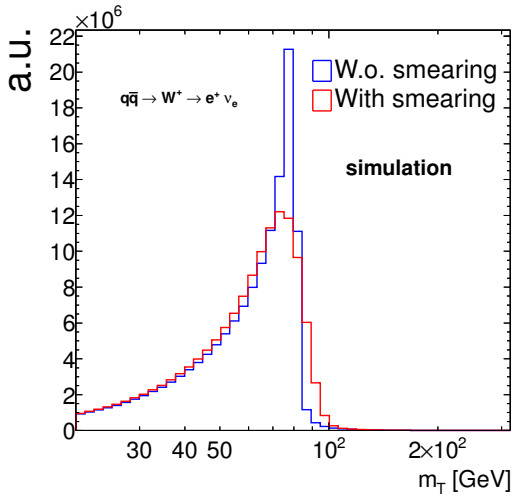

Figure 2.9.: Transverse mass of the electron neutrino pair from a W^+ decay. Shown is a simulation in arbitrary units without any further smearing in blue and with a smearing of 20% of the electron p_T in red.

2.3. Models beyond the Standard Model

The Standard Model is at the moment the best theory to describe the structure of matter and the interaction between the elementary particles but it contains also some unresolved questions. One of these challenges is the unification of the electroweak and the strong interaction. Considering that the Standard Model is based on symmetry principles such an unification would also lead to symmetry breaking similar to the electroweak interaction. This again implies the existence of new gauge bosons. Theories which try to do such an unification are called Grand Unified Theories (GUT). The new gauge bosons are often referred as W', for the charged bosons and Z', for the neutral bosons, whereas this thesis is focused on the charged bosons.
Some of the theories predict a very strongly suppressed leptonic decay. In this case right-handed charged bosons $W_R^{\pm}$ can not decay into a right-handed neutrino ν_R because the neutrino is to too heavy for the decay $W_R \rightarrow e\nu_R$ [30]. Other theories, so-called Kaluza-Klein models, which also provide models to include the gravitation, predict new gauge bosons under inclusion of extra dimensions [31].

Sequential Standard Model (SSM)

This thesis focuses on the so-called sequential Standard Model [32] as a kind of benchmark model, but this analysis is also sensitive to other models, as long the theory predicts a resonance-like excess above the Standard Model prediction. This model predicts a charged W' with spin 1 and the same couplings to the leptons as the SM W-boson. The cross-section is therefore almost the same as it is for the SM W, except

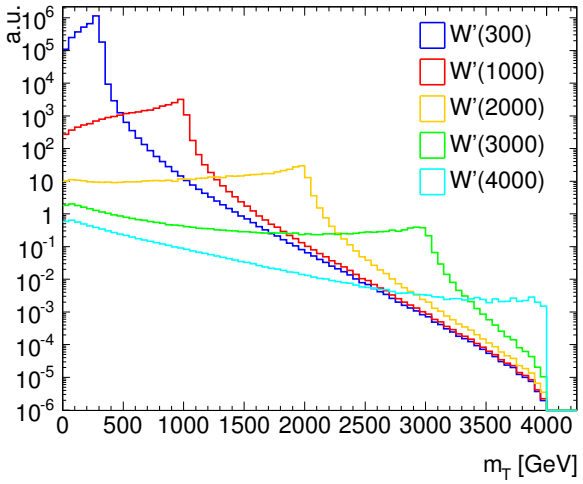

Figure 2.10.: Transverse mass distribution of simulated hypothetical SSM W' bosons with different pole masses. The ordinate is in logarithmic scale and shows arbitrary units. No charge distinction is made.

the mass of the SM W boson, which has to be replaced by the mass of the W' boson:

$$\hat{\sigma}(q_i\bar{q_j} \to e^+\nu_e) = \frac{G_F^2|V_{ij}|^2}{18\pi} \frac{M_{W'}^4}{(\hat{s} - M_{W'}^2)^2 + M_{W'}^2\Gamma_{W'}^2} \,. \tag{2.33}$$

The width of the Breit-Wigner resonance can also be calculated using the Feynman rules:

$$\Gamma_{W'} = \frac{\alpha_s}{36} \frac{M_{W'}}{\sin^2(\theta_W)} \,. \tag{2.34}$$

Figure 2.10 shows the transverse mass distribution of simulated SSM W' bosons with different pole masses up to 4 TeV. Different properties of the W' are visible in this plot.
First it can be seen that the cross-section is decreasing with higher pole masses resulting in a lower scaled distribution. Second it is shown that the width increases with rising pole masses (see equation 2.34).

At last it is also visible that the low m_T tail increases in relation to the peak. This is given, because the complete cross-section is not only given by the part of the hard process, also the hadronic cross-section, given by the PDFs gets more influence for high pole masses. This is clarified by equation 2.28. Considering a 4 TeV W' the needed $\hat{s}$ to produce that high masses is also 4 TeV. Taken into account that the center of mass energy of the protons is 8 TeV, the product $x_{q_i}x_{q_j}$ has to be 1/2. The probability to find quarks with that high x in a proton is given by the PDFs and can be seen in figure 2.6. There it is visible that the probability is very low, leading to a strong suppression of the production of 4 TeV W' and an enriched low m_T tail.

2.4. Previous results

Up to now no evidence of new heavy charged W' were found but exclusion limits on the mass of a W' were set. In table 2.4 current 95%C.L. mass exclusion limits are shown for different experiments together with the integrated luminosity L_{int}[7] and the center of mass energy $\sqrt{s}$.
The DØ and CDF experiments stationed at the Tevatron accelerator of the Fermilab performed a search with $p\bar{p}$-collision at $\sqrt{s} = 1.96$ TeV and an integrated luminosity of 1 respectively 5.3 fb^{-1}. They excluded a SSM W' up to about 1 TeV [33] [34]. The current ATLAS mass limit of 2.5 TeV [35] is calculated with 4.7fb^{-1} of data at $\sqrt{s} = 7$ TeV. The CMS collaboration has analysed the complete 20fb^{-1} of 8 TeV data from 2012 leading to a mass limit of 3.35 TeV which is currently the highest mass limit on a SSM W'.

Experiment	L_{int} [fb^{-1}]	$\sqrt{s}$ [TeV]	observed limit [TeV]
ATLAS 2011	4.7	7	2.5
DØ2007	1	1.96	1
CDF 2010	5.3	1.96	1.12
CMS 2013	20	8	3.35

Table 2.4.: Recent mass limits for a SSM W' from ATLAS [35], CDF [33], CMS [36] and DØ [34]

[7] Integrated luminosity can be seen at this point as a measure of the amount of data taken.

3. Experimental setup

In the beginning, this chapter gives an overview of the *Large Hadron Collider* (LHC) and the ATLAS experiment. Section 3.2 provides a more detailed description of the ATLAS detector, by introducing the different components of the detector. In the end a short introduction into the data processing and storing is provided.

3.1. The Large Hadron Collider

The *Large Hadron Collider* [37] is a hadron-hadron collider stained at CERN[1] in Geneva (Switzerland). It replaced the LEP[2] , which was turned off in 2000, and is build in the almost 27 km long tunnel.
Since the LHC accelerates two same charged particles it is not possible to use the same beam pipe for both beams as it can be done at $p\bar{p}$-colliders, e.g. Tevatron [38]. The advantage of using pp-collision is given by the higher instantaneous luminosity of about $10^{34}\text{cm}^{-2}\text{s}^{-1}$. The colliding protons are bundled in bunches of about 10^{11} protons. These bunches have a time distance of 50 ns and are again grouped into larger bunch trains with a much larger time distance compared with the bunches itself. The actual colliding happens with a small crossing angle, to prevent too much interactions along the beam pipe.
It is not possible to accelerate resting particles with a ring collider. Therefore a pre-accelerator complex is needed. This is done in different stages, starting with a linear accelerator (LINAC2) to bring the protons to 50 MeV. After the protons passed the Proton-Synchrotron (PS) they have an energy of 25 GeV and reach the Super Proton-Synchrotron (SPS), which accelerates them to 450 GeV. This energy is enough to inject them afterwards in the LHC. In the year 2012 the LHC managed to accelerate the protons to an energy of 4 TeV, which corresponds to a center of mass energy of 8 TeV.

Luminosity

The instantaneous luminosity connects the event rate of an experiment with the coss-section. It can be calculated with beam properties of the accelerator:

$$\mathscr{L} = \frac{nfN_1N_2}{4\pi\sigma_x\sigma_y}\,, \tag{3.1}$$

where n is the number of proton bunches per beam, f the circulation frequency, N_1 and N_2 the number of protons per bunch and σ_x and σ_y the transverse width of the

[1] Conseil Europén pour la Recherche Nucléaire
[2] **L**arge **E**lectron **P**ositron

Gaussian expected beam profile. These beam profile parameters are measured with so-called "van-der-Meer-Scans" [39], where the beams are stepwise displaced against each other. A measure of the total amount of data taken with an experiment is given by the integration of the instantaneous luminosity over the whole data taking time $L = \int dt \mathscr{L}$. The data taking with pp-collisions at 8 TeV started in March 2012 and ended in December 2012 leading to an integrated Luminosity of about 20 fb^{-1}.

3.2. The ATLAS- experiment

The ATLAS-detector [40] is a multipurpose detector and designed to measure electrons (positrons), photons, muons, τ-leptons and jets in a large kinematic range. It consists of several components which are ordered cylindrical around the beam pipe. An overview over the whole detector is given in figure 3.1. In the following the several components are shortly introduced.

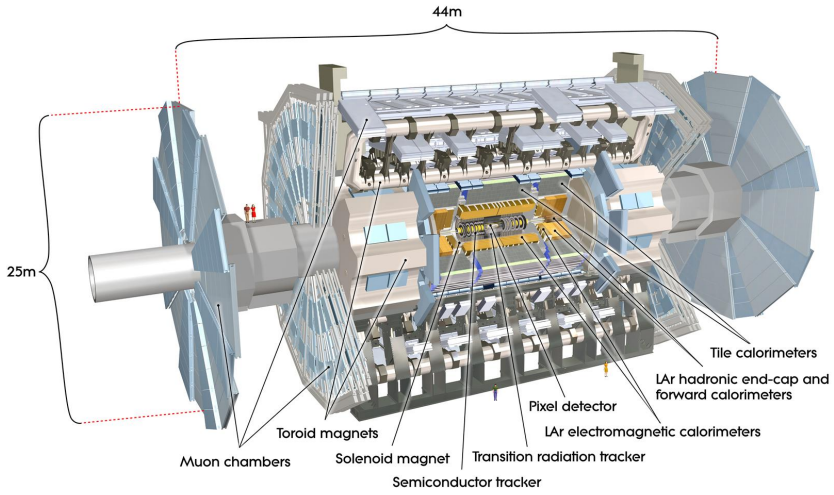

Figure 3.1.: Overview of the ATLAS-experiment. The different components are marked in different colors. The overall weight of the experiment is about 7000 t [40].

3.2.1. Coordinate system

The origin of the coordinate system is the collision point. The z-axis points in beam direction, the x-axis to the middle point of the accelerator and the y-axis in the up-direction so that it originates a right handed coordinate system. The azimuth angle φ lies in the x-y plane and measures the angle relative to the x-axis and covers a range from $-\pi$ to π. The polar angle θ measures relative to the z-axis. Instead of using the polar angle it is common to use the pseudorapidity $\eta = -\ln(\tan(\theta/2))$. For massless particles the pseudorapidity is equal to the rapdidity $y = \frac{1}{2}\ln\left(\frac{E+p_z}{E-p_z}\right)$.

The transverse momentum p_T, the transverse energy E_T and the missing transverse energy[3] E_T^{miss} are given in the x-y plane. At some points the variable ΔR is important, in order to calculate distances in the η, φ-plane. It is defined as: $\Delta R = \sqrt{\Delta\eta^2 + \Delta\varphi^2}$.

3.2.2. Principal construction

The different components of the ATLAS-detector are build shell-like around the beam pipe. The *inner detector* (ID) is nearest to the beam pipe. It contains a tracking system, which itself consists out of three components and is infiltrated by a 2 T strong magnetic field. With the tracking system it is possible to measure the vertex and the momentum of charged particles.
The next following component in radial direction is the calorimeter system. It consists of the electromagnetic liquid argon (LAr-) sampling calorimeter, which has a full φ and a $|\eta|$ coverage up to 3.2. Also a part of the calorimeter system is the hadronic calorimeter (HCAL). Up to $|\eta| = 1.7$ a *scintillator tile* calorimeter is used and for the handronic endcap region, $1.5 < |\eta| < 3.2$, also LAr calorimeters are used. For the following forward region ($3.2 < |\eta| < 4.9$) also a LAr calorimeter is used.
The whole calorimeter system is covered by toroid magnets [41] [42] [43]. They have air-cores and generate fields with big deflecting forces. Together with three layers of tracking chambers they build the muon-system [44]. The toroid system was decisive for the rest of the construction. The airy, more open, construction minimises multi-scattering and allows a precise momentum resolution ($\sigma(p_T)/p_T \approx 2.4\%$ [45] for muons in the region of the inner detector). This thesis is not focused on any muon properties, therefore no further description of the muon detector components is given.
The rate of pp-collisions is about 1 GHz for an design luminosity of $\mathscr{L} = 10^{34}\text{cm}^{-2}\text{s}^{-1}$ but the rate how fast events can be recorded is only about 200 Hz. To provide such an reduction of the rate, ATLAS has a three staged trigger system (see section 3.2.5). The first stage, namely level-1 trigger (L1), uses only parts of detector information to decide if an event should be further processed and reduces the rate to 75 kHz. The following high level trigger (HLT), level-2 (L2) trigger and event filter (EF), reduce the rate further to the needed 200 Hz.

3.2.3. Tracking system

For the investigation of physical processes a high momentum- and vertex resolution is needed. If it is taken into account that the track density is very high at ATLAS, a fine granularity is needed. The tracking system has three sub-components: The pixel detector, the semi conductor tracker (SCT) and the transition radiation tracker (TRT). An overview of the inner detector, another name for the tracking system, is shown in figure 3.2. The solenoid magnet, which generates the magnetic field for the momentum measurement with an resolution of σ_{p_T}/p_T =0.05%p_T [GeV] $\oplus$ 1%, is

[3]Missing transverse energy is given by the absolute value of the missing transverse momentum which is the negative vector sum of all reconstructed momenta: $E_T^{miss} = |\vec{p}_T^{miss}| = |-\sum_i \vec{p}_{T,i}^{rec}|$. A detailed description is given in section 4.3.

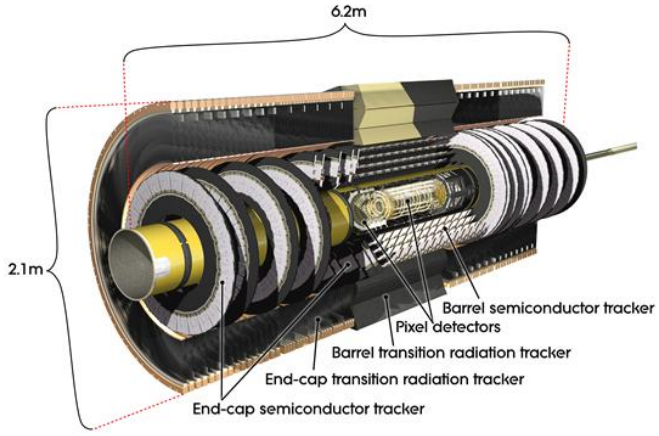

Figure 3.2.: Cut-away view of the ATLAS inner detector [40].

5.3 m long and has a diameter of 2.5 m. The several sub-components are explained in the following.

Pixel detector

The pixel detector is build next to the beam axis and covers a region of $|\eta|$ <2.5. The silicon pixel modules are arranged in layers, cylindrical around the beam axis for central regions ($|\eta| < 2.5$) and perpendicular to the beam axis for endcap regions. Every track crosses typically 3 of these layers. The purpose of the pixel detector is the very precise measurement of the track, the reconstruction of the interaction point (primary vertex) and secondary vertices from long living particles. The single pixels have a size of 50×400 μm^2 and reach a precision of 10 μm in $R - \varphi$ and 115 μm in z for central regions. The pixel layer nearest to the beam axis is called b-layer, because it has the purpose to resolute the secondary vertices from B-hadron decays. The pixel detector has the highest granularity of all detector components and about 80.4 million read-out channels.

Semi conductor tracker (SCT)

A further precision track detector is the silicon microstrip detector SCT, which also covers the region $|\eta| < 2.5$. There are strips, which are orientated parallel to the beam axis to measure the $R-\varphi$ position, and stereostrips, which are arranged with a small angle, to measure both coordinates. In the endcaps radially orientated sterostrips are used. The reached precision in the central region for the $R - \varphi$ plane is 17 μm and 580μm in z. It has 4 layers and about 6.3 million read-out channels.

Transition radiation tracker

The TRT covers a region of $|\eta| < 2.0$ and measures the intrinsic $R - \varphi$ position with a precision of 130μm. It is build with straw tubes, that have a diameter of 4 mm and

are orientated parallel to the beam-axis over a length of about 144 cm. The central straws are divided in two parts, one with $\eta < 0$ and the other with $\eta > 0$, so that only a left right information can be given. For endcap regions the straws are radial orientated. Every track leaves about 36 hits in the TRT and the number of read-out channels is about 351000.

3.2.4. Calorimeters

The calorimeters are build to measure the energy of the generated particles. Therefore so-called sampling-calorimeters are used which contain alternating active and passive material. In the dense, passive material the particles build showers, whose energy is measured in the active material.
There are electromagnetic calorimeters and hadronic calorimeters. In electromagnetic calorimeters, electromagnetic showers from electrons (positrons) and photons, are build. The energy of the ingoing particle is divided between the daughter-particles up to the point where the daughter-particles are stopped through ionization. A measure of the exponential decreasing energy loss $E(x) = E_0 e^{-x/X_0}$ is the radiation length, which is material dependent.
For hadronic showers the absorption length λ describes the average length after which it comes to inelastic scattering between hadrons and the detector material.
In figure 3.3 the calorimeter system of ATLAS is shown. It covers a region of $|\eta| < 4.9$ and combines different techniques.

An important property for an calorimeter is the energy resolution. For sampling

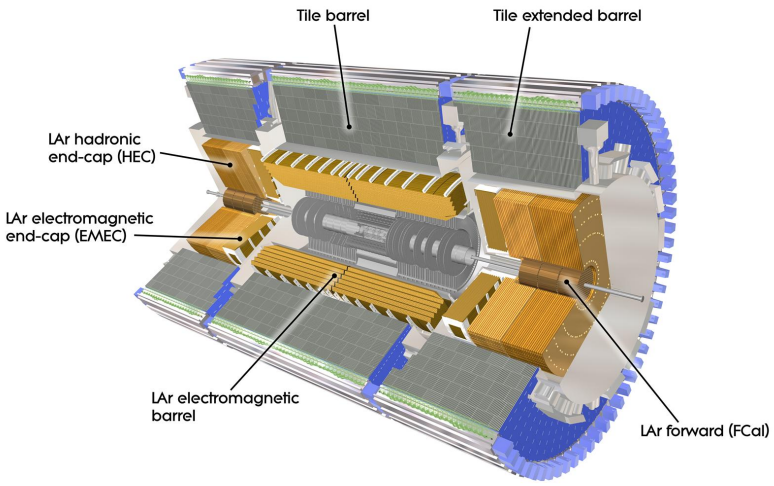

Figure 3.3.: Cut-away view of the ATLAS calorimeter [40].

calorimeters the relative energy resolution can be split into three different parts:

$$\frac{\sigma_E}{E} = \underbrace{\frac{a}{\sqrt{E}}}_{1.} \oplus \underbrace{\frac{b}{E}}_{2.} \oplus \underbrace{c}_{3.}, \tag{3.2}$$

where the first parts describes the sampling term, which rises with higher energy due to statistical processes. The second part, also called noise term, results from instrumental effects and the last term is given by calibration uncertainties, e.g. non-linearities in photomultipliers, that has a constant energy dependence.

Electromagnetic calorimeter

The electromagnetic calorimeter is a liquid argon calorimeter, which uses lead as absorber and has an accordion geometry to gain a complete and uniform φ coverage. It is split in four different regions. The first part, the region with $|\eta| < 1.475$, is called barrel calorimeter with an thickness of about $22X_0$. The region $1.375 < |\eta| < 3.2$ is covered by the endcap-calorimeter and is divided into the outer wheel ($1.375 < |\eta| < 2.5$) and the inner wheel $2.5 < |\eta| < 3.2$. An additional part of the calorimeter covers the forward region(FCAL), $3.2 < |\eta| < 4.9$, of the detector.
The region up to $|\eta| = 2.5$ is separated in three layers. In figure 3.4 the three layers are shown. The first has a very high granularity in η, to distinguish closeby particles, e.g. two photons from a π_0 decay. The second layer covers most radiation lengths compared with the other layers and has a fine segmentation in η and ϕ to provide shower shape measurements. The third layer is primarily used to give an estimate of the longitudinal leakage of a shower into the following HCAL. In order to have an estimation of the energy deposit in not instrumented regions a so-called presampler is build in front of the first layer. The resolution, that can be reached is $\sigma_E/E = 10\%/\sqrt{E}$ GeV $\oplus 0.7$ %.

Hadronic calorimeter

The hadronic calorimeter is also a sampling-calorimeter, but instead of lead, iron is used as absorber and the active material is scintillating tiles. It is divided into three different parts. The first is the tile barrel region up to $|\eta| = 1.0$, the second is the extended barrel region with $0.8 < |\eta| < 1.7$ and last is an additional liquid argon calorimeter with a coverage of $1.5 < |\eta| < 3.2$.

3.2.5. Trigger system

The trigger system can be divided into three stages. The first stage is the L1 trigger [46], that is constructed to give very fast decisions (≈ 2.5 μs) if an event shall reach the next trigger level or not. The full granularity of the electromagnetic calorimeter is to fine to come within 2.5 μs to a trigger decision. Therefore the cells are grouped in so called trigger towers, covering $\Delta\eta \times \Delta\varphi \approx 0.1 \times 0.1$. For an electromagnetic objects, it

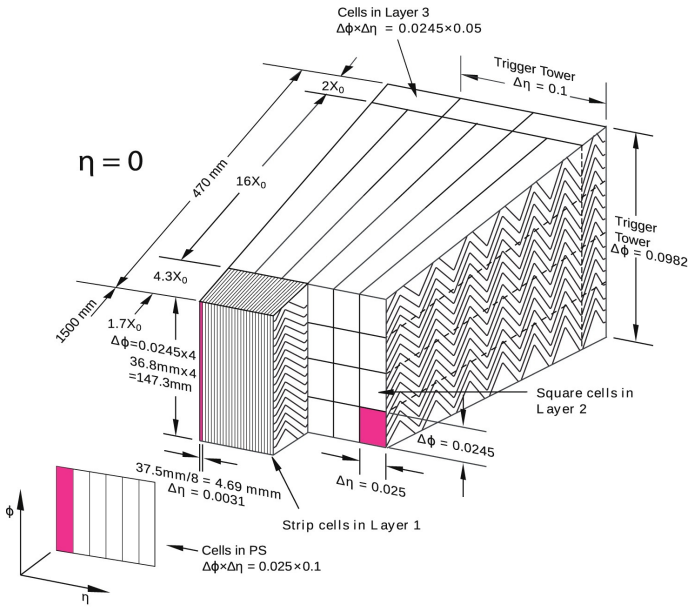

Figure 3.4.: Sketch of a module in the barrel region. The different layers and the granularities in η-ϕ are well shown [40].

is searched for energy depositions above a certain threshold in two neighboring trigger towers. If the energy deposition is above the threshold the region is called Region of interest (RoI). During the time the L1 trigger needs to come to a decision, the whole detector information is buffered and send together with the information of a RoI to the L2 trigger.
The L2 trigger uses the full granularity of the calorimeter, but only in the RoIs. In addition the L2 also takes the track information from the inner detector into account. With this information reconstruction algorithms are used to select electrons or photons, e.g. require a matched track to an energy deposition for the case of an electron. It takes the L2 trigger about 40 ms to come to a result. The rate is then already reduced below 3.5 kHz.
The last reduction of the rate to the needed 200 Hz is done by the event filter. The event filter uses the complete detector information and builds the complete event by using further reconstruction algorithms (see chapter 3).
Based on the object signature, the events are divided in (data-)streams, like the *egamma*-stream used in this analysis, which reduces the amount of data for the single analysis. This means, for example, that events that passed the jet trigger requirements are not saved in the electron stream if they not pass the electron trigger requirements.
The timing in this trigger chain is very important and is managed by the **T**iming, **T**rigger, **C**ontrol (TTC) system, which controls the timing signals an their synchronicity for the detector devices. If all trigger level give a positive decision all information of the different detector components is saved.

3.2.6. Data acquisition and computing

As mentioned before the complete detector information has to be available during the whole trigger decision chain. Therefore each detector component has a build-in buffer where the data is stored during the processing time of the L1 trigger. If the L1 trigger gives a positive result the data is digitized and send to the data acquisition (DAQ) system. There it is also saved in buffers and the L2 trigger can read out the full detector information for the RoIs. After a positive decision of the L2 trigger, the selected events are transferred to the event-building system, where the information are merged to complete events and send to the event filter for a final decision.
An event saved after a positive trigger decision is in a RAW-data format and about 1.6 MB big. The reprocessing of the data is done by different levels of a Grid-system. The principle behind Grid-computing is the usage of computing power all over the world to manage the enormous amount of data produced at the LHC [47] [48].
The first step of reprocessing is done at the Tier-0 at CERN. There the first calibration and reconstruction algorithms are applied to data. This leads to a data format called **E**vent **S**ummary **D**ata (ESD), which contains all tracks and the correspondent hits, the single calorimeter cells, groups of such cells (clusters) and the information of the muon system as well as combination of such objects. An event in ESD-format has still 1 MB.
The ESD data is then send to the Tier-1 centers which provide the needed storage and the possibility to reprocess the data again, e.g. for a new production of the ESD with a new release of the reconstruction software.
A significant reduction of the size of data to about 100 kB is done by the creation of **A**nalysis **O**bject **D**ata (AOD), which only contain information of the physics objects like electrons or jets. A further reduction is done by the creation of **D**erived **P**hysics **O**bjects (DPD), which only contain the information needed for a specific analysis. The DPDs are saved at the Tier-2 centers where they can be reached by all analysers around the world. A special format of DPD, the D3PD, is used for this analysis, where the information is stored in ROOT-Ntuples [49]. These can be stored at local Tier-3 centers, like the *maigrid* in Mainz (germany), where the D3PD, used for this analysis are stored. The data can also have additional requirements to reduce the amount of data, e.g. in this analysis a requirement is set, that at least one electron with an $p_T > 100$ GeV is present in every event. ROOT [49] is a common used analysis tool in particle physics, that provides methods for a statistical analysis and the possibility to visualize data in graphs and histograms. In this thesis all shown plots and calculations are made with ROOT if not otherwise described.

4. Reconstruction and Calibration

This chapter gives an overview of the reconstruction, identification and calibration of electrons, jets and missing transverse energy. The focus is set on central regions of the detector.

4.1. Electron candidate reconstruction

The standard electron reconstruction algorithm, called *egamma* [50], starts with the search of a *cluster* (an accumulation of calorimeter cells with energy deposition) in the electromagnetic calorimeter. The cluster is then associated with a track from the inner detector. For the search of an cluster a *slinding-window* algorithm is used. This algorithm scans with a window of 3×5 cells, with the size of one cell $\Delta\eta \times \Delta\varphi = 0.025 \times 0.025$, the second calorimeter layer, searching for energy depositions above 2.5 GeV. These clusters are then associated with a track by extrapolating from the last track point to the first layer of the calorimeter. This combination of track and cluster builds an electron candidate. The association of a track with a cluster is a strong criteria to distinguish between electron and photons, since photons themselves do not leave any track information because they are neutral. If more tracks are associated with a cluster, all are taken into account weighted with the distance to the cluster center in the η,ϕ-plane of the second layer. The number of hits in the SCT is thereby a quality attribute, because tracks without hits in the SCT have a higher probability to origin from photon conversion. At this level no direct distinction between real electrons and converted photons is made but the SCT hit information is stored. This leads in fact to a high contamination of the real electron with converted photons but ensures a high reconstruction efficiency. A rejection of the converted photons is made on the identification level explained in section 4.1.1.
After the successful assignment of a track with a cluster the energy depositions are new calculated with a bigger window of 3×7 cells in the barrel and 5×5 cells in the endcap region. After different corrections, the four momentum of the electron candidate is build with the track with the highest priority and the cluster energy.
For electrons with very low transverse momentum ($\mathcal{O}(1\,GeV)$) it is possible to improve the reconstruction efficiency if the algorithm does not start with the cluster finding but with the track finding. These algorithm are called *soft* algorithms.

4.1.1. Electron identification

The identification of electrons (EM-ID) is based on different variables containing information about the cluster shape and track information. It is divided in three stages,

loose, medium, and tight [51], which have a signal efficiency of 90% for loose, 80% for medium and 70% for tight for electrons with $p_T > 20$ GeV [51]. In the following the EM-IDs are explained in more detail with the variables used for the particular identification criteria. A summary of all cuts for the different stages is given in table 4.1.

"Loose" identification

The first stage of electron identification is given by the loose identification. In order to reduce the contribution from jets, which have typically high energy depositions in the HCAL, it is cut on the ratio, R_{had}, between the transverse energy in the electromagnetic and the hadronic calorimeter. In addition a requirement is set on the shape of the energy deposition in the first layer of the ECAL. For this the shower width variable

$$w_{stot} = \frac{\sqrt{\sum_i E_i (i - i_{max})^2}}{\sum_i E_i} \tag{4.1}$$

is defined, where i is the number of strips and i_{max} the strip with the shower maximum in the first layer. Jets typically have broader showers than electrons, so that a cut on w_{stot} will also lead in a reduction of the jet background.
Furthermore jets often contain π^0 mesons, which will decay dominantly into two photons. This would lead to two neighboring high energy depositions in the first layer. Therefore it is cut on $E_{ratio} = (E_{1st} - E_{2nd})/(E_{1st} + E_{2nd})$, which contains the energy of the highest and second highest deposition of the strips. If the values of E_{ratio} are below a certain threshold it is more likely that the deposition originates from an π^0 decay.
Also restrictions on variables including the second layer of the ECAL are done, like a requirement on the ratio $R_\eta = E_{3\times7}/E_{7\times7}$ with $E_{x\times y}$ as energy in a windows with $x \times y$ cells. This cut ensures that no broad showers are selected, like hadronic showers.
Another shower shape variable, which is introduced for the same reason, is given by

$$w_{\eta,2} = \sqrt{\frac{\sum_i E_i \eta_i^2}{\sum_i E_i} - \left(\frac{\sum_i E_i \eta_i}{\sum_i E_i}\right)^2}, \tag{4.2}$$

where i is the strip index.
In addition to the restrictions on calorimeter variables, also requirements on track properties are set. The matching between the reconstructed track and the cluster is ensured by a cut on the distance ($|\Delta\eta_1|$) between the impact point of the track in the first ECAL layer and the η of the cluster. In addition the track has to have sufficient number of hits in the pixel ($N_{Pix} \geq 1$) and pixel+SCT ($N_{SI} \geq 7$) detector and it is also required that the transverse distance between track and vertex ($|d_0|$) is below 5 mm to ensure that the track is matched with the primary vertex.

"Medium" identification

The *medium* requirements contain all cuts done in the *loose* identification. Additionally the information of the third layer is included by restricting the ratio between

the energy in the third layer and the complete cluster energy, if the p_T is lower than 80 GeV. Furthermore a requirement is set on the ratio between TRT hits above a certain energy threshold and all TRT hits and also the track-cluster matching is tightened as well the requirement of a hit in the first layer of the pixel detector.

"Tight" identification

Also the *tight* identification imposes all *medium* cuts with a couple of more requirements. For example it is cut on a distance $|\Delta\varphi|$ between the track and the cluster. For the improvement of the track-cluster matching it is required that the measured momentum from the track reconstruction matches with the cluster energy. The track quality is enhanced by the demand of a minimum number of hits in the TRT detector. In addition electrons which are tagged as converted photons are also rejected as mentioned in the beginning of section 4.1.

4.1.2. Electron energy calibration

The calibration of the calorimeter is not perfect and has η dependent miss-calibrations. Therefore η dependent correction factors are applied in the form:

$$E_{true} = \frac{E_{meas}}{1 + \alpha(\eta)}\,, \tag{4.3}$$

where E_{meas} is the measured energy and E_{true} the true energy. The correction factors are calculated by comparisons of simulations with data around the Z peak. The difference between the peak of the simulation and data is measured by fitting the invariant mass distribution of the simulation and data for different η bins. With these differences the $\alpha(\eta)$ can be calculated. They are provided by the egamma analysis group [52] and are applied by using the egamma Analysis tool kit.

4.2. Jet candidate reconstruction and calibration

For this analysis the jets play only a secondary role, namely for the calculation of the missing transverse energy. Therefore only a short overview of the jet reconstruction in ATLAS is given, a more detailed explanation can be found in [53].
The challenge of the reconstruction algorithm is to find all depositions, which contribute to the jet, by ignoring all noise terms. This analysis uses jets which are based on topological clusters. The principal of topological clustering is, to group neighbored cells of the calorimeter with significant energies, compared to the noise. This is leading to variable number of cells per cluster, different to the *sliding window* algorithm used for the electrons. After the initial building of a cluster, it is searched for local maxima inside the cluster and if a maxima is found the cluster is split into separate clusters.
These clusters are the starting point for the jet reconstruction algorithm anti $\mathrm{k_T}$ [54],

Detector component	Explanation	Cut variable
Loose identification		
HCAL and ECAL	Hadronoic leakage	R_{had}
1st ECAL layer	if $f_1 > 0.005$:	$f_1 = E_1/E$
	absolute shower width	w_{stot}
	π^0 suppression	E_{ratio}
2nd ECAL layer	Ratio of energy in 3×7 to 7×7 cells	R_η
	Lateral shower width	$w_{\eta,2}$
Tracking system	Matching between track and cluster in the 1st ECAL layer	$\lvert\Delta\eta_1\rvert < 0.015$
	Transverse distance between track and vertex	$\lvert d_0\rvert < 5$ mm
Pixel detector	Number of hits in pixel+SCT	$N_{SI} \geq 7$
	Number of pixel hits	$N_{Pix} \geq 1$
Medium identification (including loose)		
3rd ECAL layer	Ratio of energy in 3rd layer to cluster energy	f_3
Tracking system	Matching between track and cluster in the 1st ECAL layer	$\lvert\Delta\eta_1\rvert < 0.005$
TRT	Ratio between TRT above an energy threshold and all TRT hits	R_{TRT}
Pixel detector	Hit in the first pixel layer	
Tight identification (including medium)		
Tracking system	Transverse distance between track and vertex	$\lvert d_0\rvert < 5$ mm
	Ratio of cluster energy and track momentum	E/p
	Distance between track and cluster	$\lvert\Delta\varphi\rvert$
	Rejection of electrons tagged as converted photons	
TRT	Minimum number of hits in TRT	N_{TRT}

Table 4.1.: Overview of the different electron identification criteria, loose, medium and tight.

that is used in this analysis. It starts with a definition of a distance between each cluster, based on energy and the geometry of the cluster. In addition each cluster gets an parameter assigned, that describes the distance to the beam axis. Starting with the cluster with highest p_T, the four momenta of the initial and the nearest cluster are added and the distances are calculated new. This new object is then used to find the next nearest cluster and again the four momenta are added and the distances are re-calculated. This is done iteratively until the distance to next cluster is bigger than the distance to the beam axis. Then the object is removed from the list and defined as a jet. This procedure is done until no clusters are left.
Also for jets a recalibration has to be done due to different reasons. For example the response for hadronic showers in the HCAL is smaller than for electromagnetic showers[1]. In addition *dead* material[2] can cause not detectable energy depositions. Furthermore it is possible that parts of a shower escape the detector acceptance. These corrections are done with a tool provided by the ATLAS Jet and Missing Et Group[3].

4.3. Missing transverse energy reconstruction and calibration

As already mentioned in section 2.2.2 it is not possible to detect neutrinos with the ATLAS-detector directly. Therefore this sections describes how the missing transverse energy is reconstructed [56]. The reason why only the transverse component of the missing energy can be reconstructed is given by the fact, that the longitudinal momentum of the initial quarks is not known and therefore it can not be calculated how much of the energy is missing. In the transverse plane the quarks have an almost neglectable transverse momentum, so that the sum of p_T from all reconstructed particles should be zero if no neutrino is present in the event[4].
The reconstruction of the E_T^{miss} starts with the reconstructed objects like electrons, jets and muons. These object are then associated to the cluster, from which they were reconstructed and than mapped to the calorimeter cells used for the reconstruction. This mapping is done in the following order: electrons, photons, hadronically decaying tau leptons, jets and muons. If one cell belongs to more than one object the first association is taken, also called overlap removal. If one cell belongs to more than one object of the same kind both are taken into account, weighted with a geometrical weight[5]. Also included in this map are cells with no associated physic object, also

[1] Mostly due to not measurable energy losses caused by nuclear interactions
[2] Not instrumented material, where particles deposit their energy is called *dead* material.
[3] ApplyJetCalibration v. 00-03-05 [55]
[4] Also particles with a very high rapidity $|\eta| > 4.9$ are not included in the summation, but these particles have also a very small p_T.
[5] This geometrical weight is dependent on the ratio of cell energy to cluster energy, e.g. an electron, where the energy of a cell contributes largest to the cluster energy, gets a higher weight than an electron where the energy of the same cell has only a low contribution of the cluster energy.

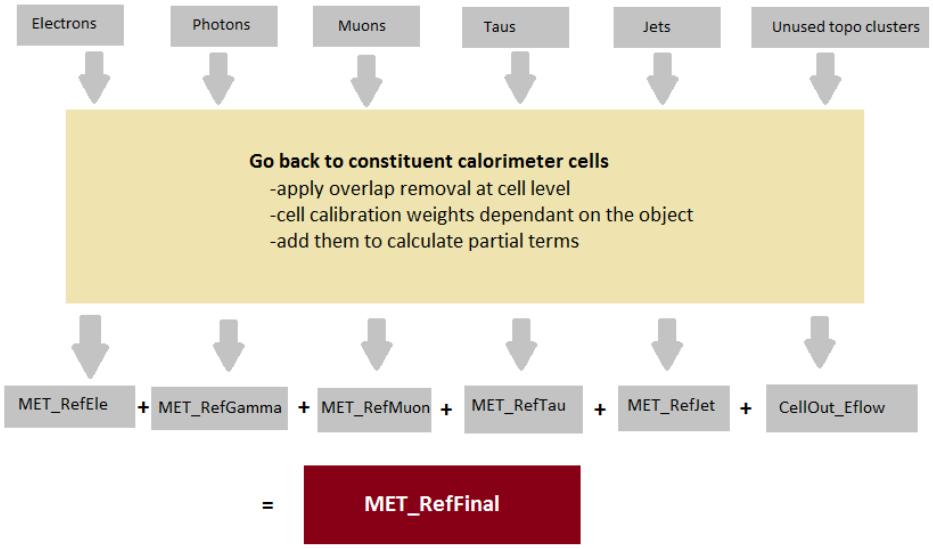

Figure 4.1.: Scheme of the E_T^{miss} reconstruction.

called *CellOut* or soft terms. The cells for each object are than grouped in so-called *MET_REF_xx* variables, where *xx* denotes the different objects. In figure 4.1 the scheme of the described reconstruction is shown. Pileup effects also the E_T^{miss}, especially the resolution, because energy depositions in the calorimeter from additional proton collisions can contribute to the terms of the missing transverse energy [57]. In order to reduce this effect, track information is used for inner detector regions, since tracks, corresponding to an energy deposition in the calorimeter, can be associated with the primary vertex.
In this analysis a tool, called *MissingETUtility* [58], is used to calculate the E_T^{miss}. It provides the possibility to propagate uncertainties for the different physical objects on the E_T^{miss} in a proper way.

5. Selection

This chapter explains the requirements, that are made on selection criteria to get rid of unwanted (background) events. The data shown here were detected 2012 with a center of mass energy of $\sqrt{s} = 8$ TeV and an integrated luminosity of about 20 fb^{-1} at the ATLAS experiment. In figure 5.1 the sum of the integrated luminosity per day is shown. The requirements which are done on electron- and E_T^{miss}-properties are clarified for data.

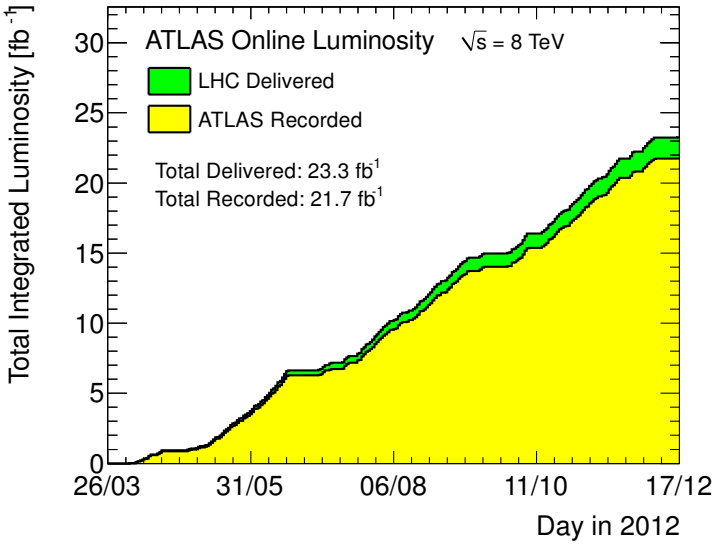

Figure 5.1.: Cumulative luminosity per day delivered to ATLAS (green) and recorded by ATLAS(yellow) [59].

5.1. Quality criteria

In the beginning it is necessary to require that the detector is in a "good condition", which means for example, that all devices operate well or the beam has stable properties. The following sections show how this is done and which quality criteria are used.

Good run list

The so-called "Good run list" (GRL) is a list provided by the Data Quality (DQ) group of ATLAS and contains information about the status of the detector for different

time periods of data taking. The time of data taking is divided into different periods (months) which are then divided into different runs (hours). These runs are then again divided into luminosity blocks (about two minutes). The decision if the data taken in such a lumi block are in a good condition is based on data quality flags for different detector components, which act basically like a traffic light. These flags are used by the combined performance groups to determine which data is good for which physics objects (electrons, photons, muons, ...). Therefore different good run lists exist for different analysis. The GRL used in this analysis [1] provides a list of lumi blocks, where everything is in good condition for all physic objects. The integrated luminosity after applying the GRL is then 20.3 fb^{-1}.

Rejecting of flawed or incomplete events

Additionally to the rejected lumi blocks from the GRL it is possible to refuse single events due to problems in some detector devices. In detail this means, events are rejected where an error flag was set for the Tile calorimeter. Furthermore it happened, that for few runs some Tile calorimeter cells get overheated, so that events are refused, where jets point to these cells and have a high energy deposition inside them. Other effects, which lead to corrupt events are so-called noise bursts, which are temporal high signals in some calorimeter cells, basically caused from electronic noise. These noise bursts are important to refuse, because they can be misinterpreted as signals from physical objects. Another incomplete event veto is included if parts of the event are not recorded completely due to a TTC system restart.

5.2. Event selection

After the quality of the data is ensured, it is necessary to set some requirements on event variables to get a further reduction of the background.

Trigger

To decrease the number of background events it is possible to require that a trigger was fired for these events. In principle the use of an unprescaled [2] trigger is preferred, in order to take all recorded events. In addition it is advisable to choose the trigger in such a way that the W-resonance is included in the sample, in order to compare the background estimate with the data in a well known kinematic region. Unfortunately the lowest unprescaled trigger, which only requires "loose" identification criteria, is the `EF_g_120_loose` trigger. This trigger requires at least one photon like object with an energy deposition in the electromagnetic calorimeter greater 120 GeV, so that the W-resonance is not completely included in the sample.

[1] `data12_8TeV.periodAllYear_DetStatus-v58-pro14-01_DQDefects--00-00-33_PHYS_StandardGRL_All_Good.xml`

[2] A prescaled trigger only records every n-th event (dependent on p_T threshold).

With the knowledge of the trigger and the GRL it is possible to calculate the integrated luminosity, which is done with a tool called "ilumicalc tool" [60] and amounts 20.3 fb^{-1} with an uncertainty of 2.8 % [61].

Jet Cleaning

Since all reconstructed physical objects contribute to the calculation of E_T^{miss}, such as jets, it is important that only events are used where all jets have well reconstructed properties.

Vertex position

In order to ensure, that only particles from pp-collision are taken into account, it is required, that there is at least one primary vertex [3] with an absolute z-position smaller than 200 mm. Also this primary vertex should have more than 3 tracks.

5.3. Electron selection

In addition to the event based selection it is also possible to set further requirements on electron properties.

Author

The so-called author cut provides, that only electrons which deposit their energy in central regions of the calorimeter are taken into account (central electrons). This is done via a bit mask called "el_author", which has the value one or three for central electrons. Additionally it is also required that a reconstructed track is matched to this central deposition. Furthermore all "soft"[4] electrons are refused by this cut.

Cut on η

To ensure the correct electron identification, the η range of the electron candidates is further narrowed down. Like mentioned before this analysis focuses on central electrons, so that all candidates with $|\eta| > 2.47$ are cut away. Also the region $1.37 < |\eta| < 1.52$ is excluded, because of a drop in energy resolution in this region due to the transition from barrel to endcap.

Object quality check

A further object quality (OQ) check can be done using a bit mask (32 bits) for each electron. This bit mask holds information for every cluster cell. If there are any

[3] Primary vertex is the one with the highest sum of p_T for the outgoing particles.
[4] "Soft" basically means electrons with p_T smaller than 15 GeV

problems with one of the cells, the corresponding bit is set to 1 and the electron candidate is refused in the selection.

Track

To reduce background from electron candidates, that do not originate from a primary vertex, it is required that the smallest distance (measured in the x-y plane) between the extrapolated track and the reconstructed position of the primary vertex is below 1 mm. In addition it is required, that the distance along the beam axis is smaller than 5 mm.

p_T cut

Like mentioned before it is not possible to keep the W-resonance in the sample due to the used trigger. Since the trigger has a "turn-on" effect, which means that it has not reached its full efficiency at 120 GeV, the p_T cut is set to 125 GeV. The p_T is calculated out of the scale corrected energy and a corrected η. This corrected η is either the track η if more than 4 hits in the pixel detector and SCT exist or the cluster η if this is not the case. The exact calculation of p_T is given by:

$$p_T = \frac{E_{corr}}{\cosh(\eta_{corr})} \,. \tag{5.1}$$

Electron ID

Another requirement for background reduction and better assurance of the quality of the selected electron candidates is the insistence of an electron identification criteria (see chapter 4). In this analysis a medium identification is required, which has a efficiency of about 70% to 80% for real electrons and a background reduction efficiency of about 95% [50].

Isolation

To reduce the background from fake electrons, like jets, it is possible to set an requirement on the isolation variable Etcone20. This variable is build by the sum of all energy deposition in cone of $\Delta R < 0.2$ around the central deposition of the electron candidate (excluding the central part of the electron) as it is shown in 5.2. Since it can happen that energy from a soft process is deposit in this cone, a correction for this effect is applied. Also the central energy deposition from the electron can leak into the surrounding cone. Therefor a further correction is applied using the `CaloIsolationCorrections` tool [62]. For this analysis the cut value on the corrected Etcone20 variable is p_T dependent so that the efficiency for real electrons does not drop below 90%.

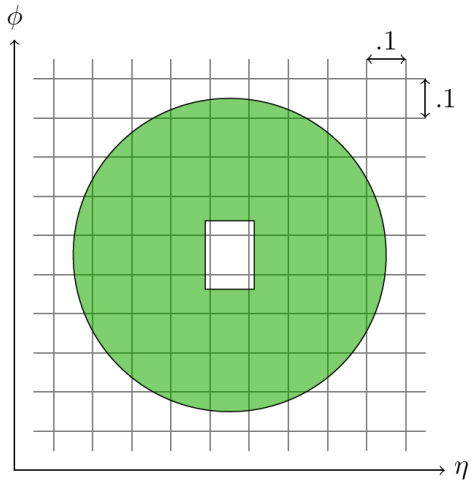

Figure 5.2.: Illustration of the calculation of the EtCone variable. Shown here is a cone size of ΔR <0.4 [63].

Trigger matching

To ensure that the electron candidate, which passed the selection up to this point is, the one, which fired the trigger a matching between the trigger object and the selected electron candidate is made. For this matching a $\Delta\ R\ =\ \sqrt{\Delta\eta^2 + \Delta\phi^2} <\ 0.15$ between the selected electron candidate and the trigger object is required. Since the used trigger is a photon trigger, the trigger objects have no track information, which is the reason why the cluster variables are used for this matching.

Additional electron veto

After the electron selection events are refused where a second, isolated, medium electron with an p_T >20 GeV is present. This cut is mostly to reduce background where more than one high p_T electron can occur, with simultaneously high E_T^{miss}.

5.4. Selection based on kinematic event properties

E_T^{miss} cut

Another cut is made if events have a reconstructed and calibrated E_T^{miss} smaller than 125 GeV. This cut value is chosen symmetric to the electron p_T cut (see section 5.3), since the transverse momentum distribution of the neutrino is expected to be symmetric to the one of the electron.

m_t cut

The last requirement set is a cut on the transverse mass, which should be above 252 GeV. This cut is chosen because it is not expected to find any new physics below this m_T and also because the high p_T and E_T^{miss} cut distort the shape in lower mass regions.

The impact of the single cuts can be seen in table 5.1 where the number of events, which pass the single cuts are shown. The percentage values refer to the amount of events before one cut. This table shows that only very view events have bad quality, since the quality cuts only refuse less than 1% of events per cut. The majority of events are refused by some of the electron cuts like the requirement of a medium electron or the isolation, which shows that up to these cuts some of the electron candidates are likely to be fakes (for example from jets). Also the E_T^{miss}-cut leads to a high number of refused events, which are mostly events with an Z decay, where no high E_T^{miss} values are expected, since the Z mostly decays in charged leptons.

Cut	Number of events passed	fraction [%]
Event cuts		
trigger	29406310	78.2
Vertex pos.	29398232	100.0
Hot Tile Error	29398231	100.0
Jet Cleaning	29303331	99.7
Tile Error	29303328	100.0
LAr Error	29241030	99.8
TTC restart	29241004	100.0
Tile trip	29241002	100.0
Electron cuts		
Author	29236007	100.0
η cut	29208730	99.9
OQ-check	29206664	100.0
Track	28964325	99.2
p_T cut	20104586	69.4
Electron ID	1485184	7.4
Isolation	712120	47.9
Trigger match	711950	100.0
Add. electron veto	671470	94.3
Event kinematic cuts		
E_T^{miss} cut	25853	3.9
m_T cut	13086	51

Table 5.1.: Impact of the selection on the number of events, which pass the single cuts. The column, fraction, shows the part of events which passes the cut compared to the previous number of events.

6. Monte-Carlo simulation

For an analysis it is essential to compare the results of the experiment with theory predictions. In order to get these, Monte-Carlo simulations are used. The generation of such Monte-Carlo (MC) (pseudo-)data can be done in three stages, which are described in this chapter: The generation of the processes, the detector simulation and the transformation of detector signals to a storable format. The reconstruction can then be done in the exact same way as it is done for data. It is also described how small differences between data and simulation are corrected. Furthermore a comparison between two different methods for the interaction with the detector is given.

6.1. Generation of events

The generation of events can be split into different steps. It starts with the cross-section calculation of the hard process, like the charged Drell-Yan process. This cross-section is convoluted with the parton density functions, as it can be seen in equation 2.24 in section 2.2 and therefore dependent which PDF is used. This convoluted cross- section is then used by random generators to calculate the four vectors of the outgoing particles. It is also possible to apply kinematic requirements on the outgoing particles (also called *event filters*). The generation of the cross-section can be done on LO, like it is done by `PYTHIA8` [64], or at NLO. Often the NLO generators, e.g. `PowHeg` [65] or `MC@NLO` [66], are specialized on the calculation of the NLO matrix elements and do not provide a calculation of the outgoing particles and have to be combined with other generators. Interferences between NLO and LO Fenyman diagrams are handled by some generators by providing weights (*mcevt_weight*) for each event. The value of this weight is either 1 or -1, which, in the sum of the events, is leading to the fact, that parts of the events cancel out in order to care about the interferences.
The electromagnetic FSR mentioned in chapter 2.2 is simulated by the usage of `PHOTOS` [67]. The colored incoming and outgoing particles can radiate gluons. These gluons can split again, into a $q\bar{q}$-pair, which also can radiate further gluons, leading to an so-called *parton shower*. This showering can be simulated iteratively up to the energy scale, where the perturbation breaks down. For NLO generators it is important to match the QCD final or initial state radiation with the matrix element of the NLO generator, which itself also includes Feynman diagrams for QCD initial and final state radiation. The transition between the still color charged particles of the parton showers to color neutral particles is described by *hadronization* models, which can be different for different generators. Also the outgoing particles of the *underlying event*,

mentioned in section 2.2, have to be simulated by the event generator. Many of the generated particles are not stable and therefore also the decay of these particles has to be simulated. After that, the four vectors of the particles can be given to the detector simulation.

6.2. Simulation of detector response

The generation of events described in the previous section is independent from the detector. The next step is the simulation of the interaction between the generated particles and the detector. To do this in a precise way it is necessary to have a very detailed model of the detector. In principle the response of every detector component has to be simulated which can be very time consuming, especially for the calorimeters. Since many Monte-Carlo samples are needed for the ATLAS collaboration it is feasible to use approximations for some of the detector responses. In this analysis two different methods of simulating the calorimeter response are used: One is using a full and detailed simulation of all interactions in the calorimeter and the other one uses parameterizations of shower shapes.

Full simulation

A full detector simulation is done with `GEANT 4` [68]. This software package simulates the transition of particles getting through all of the detector material, including interactions with it and secondary particles from these interactions. Not only the interaction with the material has to be taken into account but also the interaction with the magnetic field is important. Detector inefficiencies, like dead channels or misalignments are also included in the simulation. The resulting signals from the detector components are then treated the same way as i is done for data. This has the advantage, that the same selection algorithms can be used for data and MC. Also added to the event information of the simulation are the so-called truth properties of the generated events, which are the properties without the detector simulation. As mentioned before a disadvantage of the full simulation is the big amount of time needed to simulate the shower development in the calorimeters.

Fast simulation

A fast detector simulation, which does not simulate all interactions between the generated particles and the detector material is the so-called Atlfast-II [69] simulation. This simulation uses the full (`GEANT 4`) track simulation but a fast simulation (`FastCaloSim` [70]) for the calorimeters. For this kind of simulation some simplifications are made: The geometry of the calorimeter cells is described as cuboids in η, ϕ and r. The development of the particle showers in the calorimeters is replaced by a parameterization of the longitudinal and lateral shower shape. The longitudinal shower development is parametrized as a function of the shower depth for different particle

energies and η including fluctuations and correlations between the calibrated energy response and the longitudinal shower depth. The lateral shower is parametrized with a radial symmetric function centered on the expected impact point of the particle without fluctuations and correlations. Furthermore only three types of particles are parametrized: photons, electrons (positrons) and charged pions (used for all hadrons). The time reduction by using this kind of simulation is an order of magnitude compared to the full simulation, which is a strong argument to use the fast simulation even if it is less accurate. Since the output of the fast simulation is in the same format as the full simulation, it is possible to combine the different simulated MC samples.

6.3. Monte-Carlo samples used

Background Monte-Carlo samples

As mentioned before, Monte-Carlo simulations can be used to simulate pseudo data and compare them with data. The samples used for this analysis are listed in table 6.1. This list shows the samples from background processes, which will be discussed in detail in chapter 7.1 as well as the signal samples used for a hypothetical W' (SSM). The W, Z and $t\bar{t}$ background MCs are simulated with `PowHeg+Pythia8` at NLO and the CT10 PDFs [27]. The diboson background samples are generated with `SHERPA` [71] which is a LO generator and also with the CT10 PDFs. For the Wt and single top s-channel background samples it is used a combination of: `MC@NLO` for generating events at NLO, JIMMY [72] for modeling multi-particle scattering and HERWIG [73] for simulating particle showers. The single top t-channel process is simulated with `AcerMC` [74] together with `PYTHIA8` on LO and the CTEQ6L1 PDF [75]. The same PDF is used for the Wγ samples along with a combination of different generators: ALPGEN [76] (LO) for the hard process and JIMMY and HERWIG for multi-particle scattering and particle showers.
As described in chapter 6.1, the W and Z Monte-Carlo samples are generated in different mass windows of the W or Z to have enough statistic over the whole mass spectrum. Additionally samples are added, which are filtered by different p_T thresholds during the event generation. It has to be taken into account that these samples have a filter efficiency.
In order to compare distributions from the simulation with data, it is necessary to weight the simulated distribution to the data luminosity. This is done by multiplying a weight to the resulting distributions of each sample which is given by:

$$w = \frac{\sigma \epsilon_{filt}}{N_{gen}} \ , \tag{6.1}$$

with σ as cross-section of the simulated process, ϵ_{filt} the filter efficiency and N_{gen} the number of generated events, which are also given in table 6.1. In the following this weight is called luminosity weight. Table 6.1 shows also the correspondent luminosity of each sample, that is given by dividing the number of generated events with the product of cross-section, branching ratio and filter efficiency.

Process	N_{evt} [k]	$\sigma B \varepsilon_{filt}$ [pb]	L_{int} [fb^{-1}]	Process	N_{evt} [k]	$\sigma B \varepsilon_{filt}$ [pb]	L_{int} [fb^{-1}]
$W \to \tau\nu$				$Z \to \tau\nu$			
$W^+ \to \tau\nu$	3999	$6.89{\cdot}10^{3}$	0.58	$Z \to \tau\tau$	5000	$1.11{\cdot}10^{3}$	4.5
$W^- \to \tau\nu$	2995	$4.79{\cdot}10^{3}$	0.63	$Z(250,400) \to \tau\tau$	20	$5.4{\cdot}10^{-1}$	36
$W^+(200,500) \to \tau\nu$	45	2.51	18	$Z(400,600) \to \tau\tau$	20	$8.9{\cdot}10^{-2}$	220
$W^-(200,500) \to \tau\nu$	45	1.45	31	$Z(600,800) \to \tau\tau$	20	$1.5{\cdot}10^{-2}$	1300
$W^+(500,1500) \to \tau\nu$	45	$7.6{\cdot}10^{-2}$	590	$Z(800,1000) \to \tau\tau$	20	$3.7{\cdot}10^{-3}$	5300
$W^-(500,1500) \to \tau\nu$	45	$3.4{\cdot}10^{-2}$	1300	$Z(1000,1250) \to \tau\tau$	20	$1.2{\cdot}10^{-3}$	15000
$W^+(1500,2500) \to \tau\nu$	45	$3.2{\cdot}10^{-4}$	140000	$Z(1250,1500) \to \tau\tau$	20	$3.5{\cdot}10^{-4}$	56000
$W^-(1500,2500) \to \tau\nu$	45	$9.9{\cdot}10^{-5}$	450000	$Z(1500,1750) \to \tau\tau$	20	$1.1{\cdot}10^{-4}$	180000
$W^+(2500,3000) \to \tau\nu$	45	$4.3{\cdot}10^{-6}$	10000000	$Z(1750,2000) \to \tau\tau$	20	$3.8{\cdot}10^{-5}$	520000
$W^-(2500,3000) \to \tau\nu$	45	$1.4{\cdot}10^{-6}$	31000000	$Z(2000,2250) \to \tau\tau$	20	$1.3{\cdot}10^{-5}$	1400000
$W^+(3000,3500) \to \tau\nu$	45	$5.5{\cdot}10^{-7}$	81000000	$Z(2250,2500) \to \tau\tau$	20	$5.2{\cdot}10^{-6}$	3800000
$W^-(3000,3500) \to \tau\nu$	45	$2.1{\cdot}10^{-7}$	210000000	$Z(2500,2750) \to \tau\tau$	20	$2.0{\cdot}10^{-6}$	9900000
$W^+(>3500) \to \tau\nu$	45	$7.7{\cdot}10^{-8}$	580000000	$Z(2750,3000) \to \tau\tau$	20	$7.8{\cdot}10^{-7}$	25000000
$W^-(>3500) \to \tau\nu$	45	$3.4{\cdot}10^{-8}$	1300000000	$Z(>3000) \to \tau\tau$	20	$5.0{\cdot}10^{-7}$	40000000
Inclusive and mass binned $W \to e\nu$				Inclusive and mass binned $Z \to ee$			
$W^+ \to e\nu$	22993	$6.89{\cdot}10^{3}$	3.3	$Z \to ee$	9995	$1.11{\cdot}10^{3}$	9
$W^- \to e\nu$	16999	$4.79{\cdot}10^{3}$	3.5	$Z(250,400) \to ee$	100	$5.4{\cdot}10^{-1}$	180
$W^+(200,500) \to e\nu$	45	2.51	18	$Z(400,600) \to ee$	100	$8.9{\cdot}10^{-2}$	1100
$W^-(200,500) \to e\nu$	45	1.45	31	$Z(600,800) \to ee$	100	$1.5{\cdot}10^{-2}$	6600
$W^+(500,1500) \to e\nu$	45	$7.6{\cdot}10^{-2}$	590	$Z(800,1000) \to ee$	100	$3.7{\cdot}10^{-3}$	27000
$W^-(500,1500) \to e\nu$	45	$3.4{\cdot}10^{-2}$	1300	$Z(1000,1250) \to ee$	100	$1.2{\cdot}10^{-3}$	77000
$W^+(1500,2500) \to e\nu$	45	$3.2{\cdot}10^{-4}$	140000	$Z(1250,1500) \to ee$	100	$3.5{\cdot}10^{-4}$	280000
$W^-(1500,2500) \to e\nu$	45	$9.9{\cdot}10^{-5}$	450000	$Z(1500,1750) \to ee$	100	$1.1{\cdot}10^{-4}$	890000
$W^+(2500,3000) \to e\nu$	45	$4.3{\cdot}10^{-6}$	10000000	$Z(1750,2000) \to ee$	100	$3.8{\cdot}10^{-5}$	2600000
$W^-(2500,3000) \to e\nu$	45	$1.4{\cdot}10^{-6}$	31000000	$Z(2000,2250) \to ee$	100	$1.3{\cdot}10^{-5}$	7200000
$W^+(3000,3500) \to e\nu$	45	$5.5{\cdot}10^{-7}$	81000000	$Z(2250,2500) \to ee$	100	$5.2{\cdot}10^{-6}$	19000000
$W^-(3000,3500) \to e\nu$	45	$2.1{\cdot}10^{-7}$	210000000	$Z(2500,2750) \to ee$	100	$2.0{\cdot}10^{-6}$	50000000
$W^+(>3500) \to e\nu$	45	$7.7{\cdot}10^{-8}$	580000000	$Z(2750,3000) \to ee$	100	$7.8{\cdot}10^{-7}$	130000000
$W^-(>3500) \to e\nu$	45	$3.4{\cdot}10^{-8}$	1300000000	$Z(>3000) \to ee$	100	$5.0{\cdot}10^{-7}$	200000000
p_T binned $W \to e\nu$				p_T binned $Z \to ee$			
$W^+(100,150) \to e\nu$	400	$1.38{\cdot}10^{1}$	28.9	$Z(100,150) \to ee$	1398	8.25	170
$W^-(100,150) \to e\nu$	500	$1.32{\cdot}10^{1}$	37.8	$Z(150,200) \to ee$	299	1.31	230
$W^+(150,200) \to e\nu$	100	2.16	46.2	$Z(200,300) \to ee$	100	$4.1{\cdot}10^{-1}$	240
$W^-(150,200) \to e\nu$	100	2.08	48.2	$Z(>300) \to ee$	20	$6.7{\cdot}10^{-2}$	300
$W^+(200,300) \to e\nu$	50	$6.6{\cdot}10^{-1}$	75				
$W^-(200,300) \to e\nu$	50	$6.3{\cdot}10^{-1}$	78				
$W^+(>300) \to e\nu$	10	$1.1{\cdot}10^{-1}$	88.6				
$W^-(>300) \to e\nu$	10	$9.9{\cdot}10^{-2}$	100.5				
Diboson				Top			
$WW \to \ell\ell\nu\nu$	2700	5.50	490	$t\bar{t} \to \ell X$	14968	$1.14{\cdot}10^{2}$	130
$WZ \to \ell\ell\ell\nu$	2700	9.75	280	s-channel $t \to W\tau\nu$	200	$5.6{\cdot}10^{-1}$	350
$ZZ \to \ell\ell\ell\ell$	1800	8.74	210	$Wt \to X$	1000	$2.07{\cdot}10^{1}$	48
$ZZ \to \ell\ell\nu\nu$	900	$4.9{\cdot}10^{-1}$	1800	t-channel $t \to \tau X$	293	8.58	34
$VV \to \tau\tau qq$	200	1.70	120	s-channel $t \to We\nu$	200	$5.6{\cdot}10^{-1}$	350
$VV \to \tau\nu qq$	1000	9.56	100	t-channel $t \to eX$	300	8.59	35
$VV \to eeqq$	200	1.70	120				
$VV \to e\nu qq$	890	9.56	93				
				Wγ			
				$W\gamma + 0p$	14296	$7.21{\cdot}10^{1}$	200
				$W\gamma + 1p$	5394	$2.67{\cdot}10^{1}$	200
				$W\gamma + 2p$	2899	$1.16{\cdot}10^{1}$	250
				$W\gamma + 3p$	860	4.48	190

Table 6.1.: Monte-Carlo samples used for the background estimation. The number in braces indicate the boson mass range, respectively p_T range of the electron (in GeV) in which the samples are produced. The samples without any requirements on the mass or p_T are called inclusive. The label $+xp$ (for the $W\gamma$ samples) indicates, that the sample was produced requiring x additional partons in the final state. All listed W-boson samples are simulated with the fast simulation. In addition also full simulated W$^+$-boson samples for the mass bins: 200 GeV-500 GeV, 2500 GeV-3000 GeV and >3500 GeV are used in this analysis for comparisons.

Signal Monte-Carlo samples

In order to have a description of a hypothetical (SSM) W'-boson, signal samples are produced. On the one hand there is a sample for a SSM W' with a pole mass of 3 TeV, shown in table 6.2 and on the other hand there is a so-called flat sample. This sample is not simulated for a dedicated pole mass but flat up to 4 TeV. It is possible to get the mass distribution for W' signals with certain pole masses by applying a reweighting function. This function has dependencies of the pole mass, which is intended to generate, and the mass of the flat sample. The exact mathematical function can be found in the appendix A.1. For each event the flat invariant mass is given together with the polemass one wants to have into this function and the resulting number is applied to the event as a weight. The signal samples which are used in this analysis are listed in table 6.2, where also the number of generated events, the cross-section and the kind of simulation is given. A further reweighting to the data luminosity is of course also needed if any comparisons with data are made.

Mass				Generator		
$[GeV]$	Γ [GeV]	B($W' \to \ell\nu$)	N_{evt} [k]	σB [pb]	L_{int} [fb^{-1}]	Simulation
Flat			1646	2.525E+01	22	AFII
3000	106.46	0.0818	180	3.870E-03	16000	Fast Sim
3000	106.46	0.0818	180	3.870E-03	16000	Full Sim

Table 6.2.: Monte-Carlo signal samples used in this analysis. Beside the number of generated events, cross-section and correspondent luminosity also the kind of detector simulation, that is used, is shown.

6.4. Corrections applied to simulation

In order to correct small differences between the Monte-Carlo simulation and data, some correction (scale) factors are applied.

k-factor

As described before, the events are generated at LO or NLO. To get the process in the next higher order so-called k-factors are applied. These k-factors are the ratio of the NLO (NNLO) cross-section and the LO (NLO) cross-section. They are calculated for QCD and electro-weak interaction separately. For most of the Monte-Carlo samples used, this factor is applied inclusive (not in dependence of any kinematic variable). For the signal ($pp \to W' \to Xe\nu X$) and the W Monte-Carlo a k-factor is applied to each event depending on the generated mass and charge of the W (W') boson. The values of the k-factors for the W background sample are in the range of about 1.05 to 1.10.

Energy smearing

The detector resolution is underestimated in the simulation, so that a further smearing of the electron energy is applied. This smearing is done by calculating a random variable following a normal distribution with the detector resolution as width, which is then applied to the energy of the electron. This correction factor is applied to all simulated processes and has a value of a few percent.

Vertex z position reweighting

For data the z position of the primary vertex is in principle a normal distribution around zero. It is not possible to simulate this with the same width of the normal distribution without knowing the exact number [1]. To correct these differences an event weight is applied in such a way, that the vertex z position distribution from the simulation matches the one from data. The weights are provided by a tool from the ATLAS- collaboration [52]. A comparison of the vertex z position for data and MC is shown in figure 6.1. Here the Monte-Carlo simulation includes all simulated backgrounds (shown in table 6.1). As the figure shows, the distribution follows a Gaussian like shape for data and MC having a different width without the re-weighting, but this is fixed after weights are applied. The effect of the re-weighting on the selection described in chapter 5 is only 0.03%.

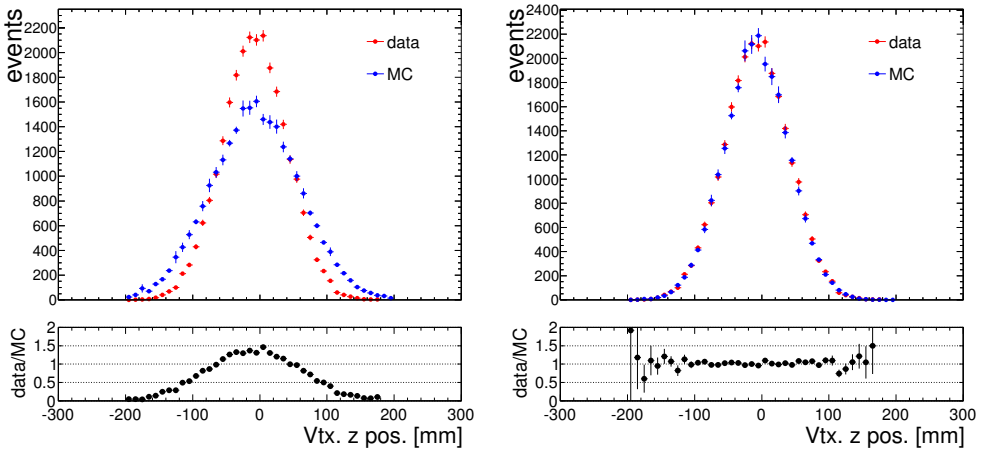

Figure 6.1.: Comparison of vertex z position between data and Monte-Carlo simulation after the selection. Left: Without applied weights. Right: With applied weights

PileUp-reweighting

Since the protons are bundled in bunches, it can happen that more than one pp-collision happens per bunch crossing, which is also called *in-time-pileup*. A good

[1] The Monte-Carlos are typically generated before data taking

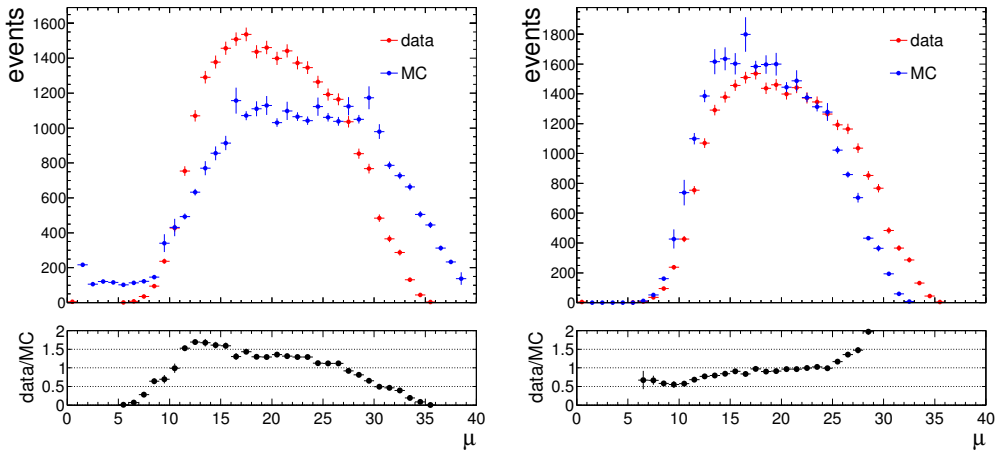

Figure 6.2.: Comparison of average interactions of bunch crossing (μ) between data and Monte-Carlo simulation after the selection. Left: with applied weights. Right: without applied weights

variable to measure this, is the number of primary vertices N_{vtx}. It is also possible that signals from previous bunch crossings occur in later ones, leading to the so-called *out of time pileup*, which can be quantified by the number of interactions averaged over one bunch train and a luminosity block (μ). Both variables are strongly dependent on the setup of the accelerator and the detector. Initially the Monte-Carlo samples are generated with a generic function, that is not well adjusted to data because the simulation takes place before or while data taking. The pileup weights, which are then applied to MC, are provided by a tool from ATLAS ("Extended PileUp Reweighting Tool" [77]) and are optimized to reweight the μ distribution in such a way that it agrees with the one from data. In figure 6.2 the unweighted μ distribution is shown on the left side, where it can be seen that the generic MC function does not match to the data distribution. The reweighted MC distribution compared to data is shown on the right side and it is visible that the agreement between data and MC is much better.
A comparison of the N_{vtx} distributions between data and MC with and without weights is shown in figure 6.3. Also here the reweighting leads to a much better agreement between data and MC.

Trigger scale factors

Differences in the trigger efficiency are corrected by applying a p_T and η dependent scale factor. These scale factors are provided by the egamma working group and are also used for the official W' analysis. The method used to calculate this scale factors is the so-called "tag and probe" method. The idea of this method is to "tag" one electron by applying very tight cuts and almost no requirements on a second electron ("probe") except a cut on the invariant mass of the "tag and probe" pair to be within

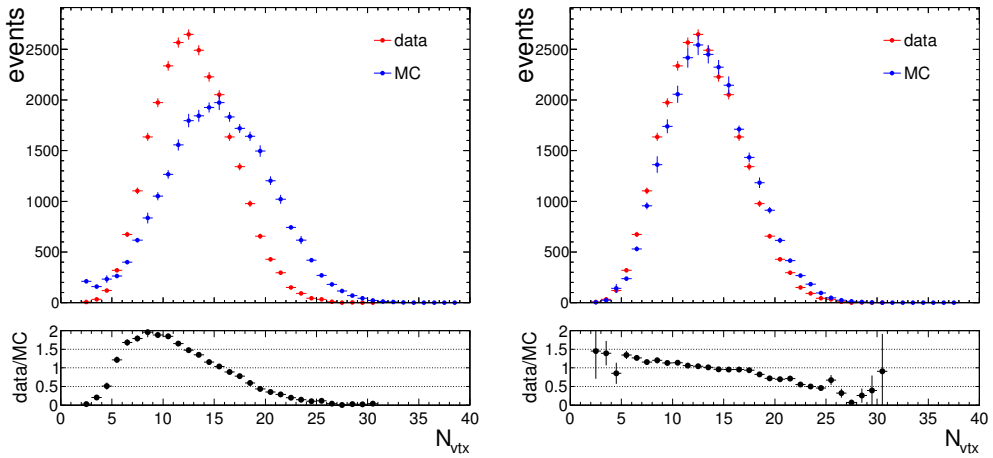

Figure 6.3.: Comparison of number of primary vertices (N_{vtx}) between data and Monte-Carlo simulation after the selection. Left: with applied weights. Right: without applied weights

the Z peak region (e.g. 80-100 GeV). This invariant mass cut makes it possible to be more sure that the "probe" electron is an actual electron (the second one from the Z decay), without applying any identification cuts. Then the efficiency can be calculated by simply dividing the amount of probe events after the trigger cut by the events before the trigger cut. The actual influence of this scale factor on the selected number of events is in the order of 0.05 %.

Reconstruction scale factor

Corrections due to differences in the reconstruction are applied by using the `egamma analysis toolkit`. Basically these corrections are the ratio between the reconstruction efficiency of MC and the reconstruction efficiency of data in bins of η and p_T. Overall this has an effect of about 0.5 %.

Identification and isolation scale factors

One other scale factor is applied for discrepancies in the identification and the isolation efficiency of the electron. This is also done in a p_T and η dependent way using the "tag and probe" method and has a 1.8 % overall effect.

6.5. Comparison of fast and full simulated Monte-Carlo samples

In this analysis the p_T and mass binned W Monte-Carlo samples are generated with the fast simulation, whereas the inclusive (not mass or p_T binned) samples are generated with full simulation. To ensure the compatibility between the two kinds of simulation a comparison of fast and full simulated signal and background samples is made. The following sections will focus on the comparison of the W' 3 TeV signal sample to investigate differences at very high p_T, whereby this differences are also visible for the investigated background samples.
In order to ensure, that the differences only occur from the differences in the detector simulation, kinematic variables were compared on generator level. Exemplary the p_T distribution on generator level is shown in figure 6.4 on the left side, where it is visible that there are no differences on generator level.
In order to find differences after the selection, table 6.3 shows a comparison of the number of selected events after each cut for the fast and full simulated W' 3 TeV signal sample. Additional to the cuts that were made on data (see chapter 5.2), truth cuts on the mass generated signal samples are applied, which only keep events where the generated W' decays into an electron and not a μ or τ lepton. The differences before the isolation cut are at most 0.1 %. After the isolation cut the differences grow to about 0.5 % and rise after the E_T^{miss} cut further to $\approx 0.7\%$. The influence of the E_T^{miss} cut is clarified in figure 6.4 on the right side, where the missing transverse energy is shown with all cuts before the E_T^{miss} cut applied. The visible differences for E_T^{miss} values below 125 GeV and above 1.5 TeV leads to differences shown in table 6.3.

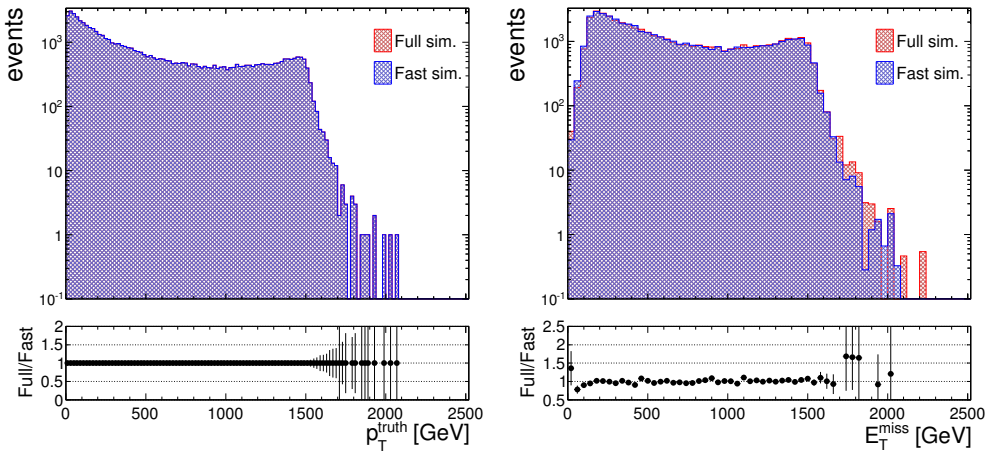

Figure 6.4.: Comparison of the p_T distribution of a W' 3 TeV signal sample between AtlfastII (blue) and full simulation (red). Left: p_T distribution on truth level. Right: E_T^{miss} after reconstruction and selection.

Cut	Fast	Full	differences [%]
gen.	180003	180001	0.00
with truth cuts	60518	60517	0.00
trigger	44708	44690	0.04
Vertex pos.	44396	44352	0.10
Jet Cleaning	44263	44271	−0.02
Tile Error	44263	44271	−0.02
LAr Error	44263	44271	−0.02
TTC restart	44263	44271	−0.02
Tile trip	44243	44257	−0.03
η cut	43740	43737	0.01
OQ-check	43710	43712	−0.00
Track	42542	42529	0.03
p_T cut	40924	40928	−0.01
Electron id	39344	39304	0.10
Isolation	38616	38434	0.47
Trigger match	38614	38433	0.47
Add. electron veto	38595	38406	0.49
E_T^{miss} cut	37667	37402	0.71

Table 6.3.: Impact of the cuts on number of events for the fast and full simulated W' 3 TeV sample.

6.5.1. Comparison of shower shape variables

Since the electron identification, described in chapter 4.1.1, cuts on several shower shapes, a comparison between fast and full simulation shower shape variables is done. Exemplary the R_η distributions for the W' 3 TeV signal samples and the mass binned (200 GeV $< m(W^+) <$ 500 GeV) W^+ background sample are shown in figure 6.5. For both samples it can be seen that fast and full simulation have a peak at about 0.97. Additionally the fast simulation has a second peak at about 0.95, which is not present for the full simulation. This peak occurs due to a high η dependence of R_η for the fast simulation. This is shown figure 6.6 where R_η of the W' 3 TeV sample is shown for different p_T and η bins. For $|\eta| < 0.8$ the fast distribution has only a small shift to lower values, but for higher η values this shift grows. Comparison of additional shower shape variables are shown in appendix A.1 and appendix A.2.

However, these differences have no large impact on the selection, as it can be seen in table 6.3, where the difference after the electron identification cut is only about 0.1 %. The reason for the small influence is given by the cut values for the single shower shape variables, which are dependent on p_T and η of the electron, but always below the regions of big differences between the fast and full simulation. For R_η this cut is, for instance, always below 0.9 which clearly is out of the region of big discrepancies.

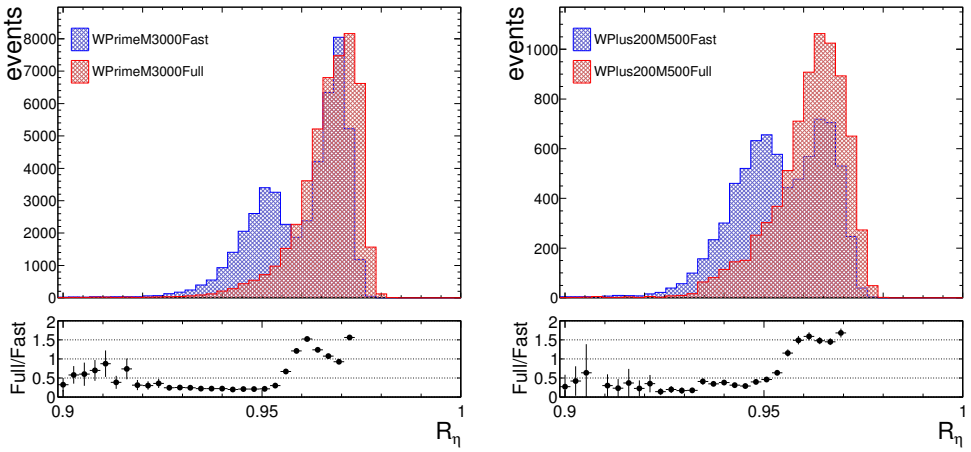

Figure 6.5.: Comparison of R_η between AtlfastII (blue) and Full simulation (red) of the W' 3 TeV (left) and W$^+$(2500 GeV$<m(W^+)<$ 3000 GeV) sample (right).

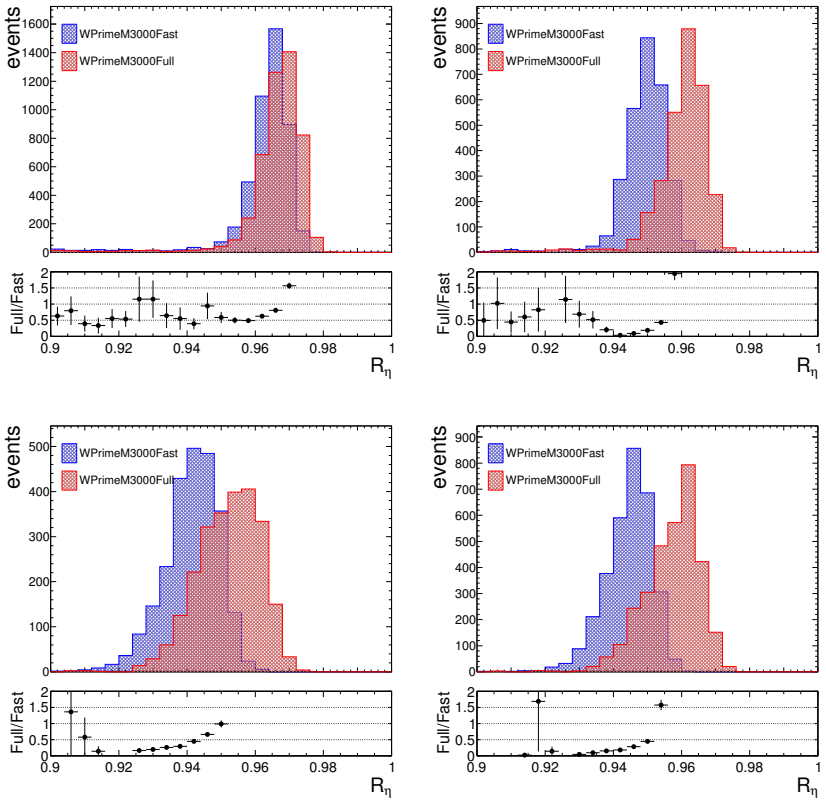

Figure 6.6.: Comparison of R_η between AtlfastII (blue) and Full simulation (red) of the W' (3 TeV) signal sample in different η and p_T bins. Top left: $|\eta| < 0.8$; 0.0 GeV$<$ p_T $<$250 GeV. Top right: 0.8$<$ $|\eta|$ $<$1.37; 0.0 GeV$<$ p_T $<$250 GeV. Bottom left: 1.52$<$ $|\eta|$ $<$2.01; 0.0 GeV$<$ p_T $<$250 GeV Bottom right: 1.52$<$ $|\eta|$ $<$2.01; 250.0 GeV$<$ p_T $<$1000 GeV

6.5.2. Isolation comparison

To investigate the differences in selected number of events after the isolation cut, figure 6.7 shows the distribution of the uncorrected (corrected) isolation variable Etcone20 on the left (right) panel. The distributions show real electrons from the W' decay, which pass the selection up to the isolation cut. Again both distributions show a shift between fast and full simulation. The reason for the double peak structure for the uncorrected distribution is given by a high p_T and η dependence, which is also visible in figure 6.8. There, the mean of the isolation distribution for several p_T bins is shown. Also it is shown, that the fast simulation has a weaker p_T dependence than the full simulation, which then leads to an overcorrection of the corrected isolation, that shows that the isolation correction is optimized for the full simulation.
Differences in the efficiency of the isolation cut are shown in figure 6.9. Efficiency in this context, is the ratio of events before the isolation cut and after the isolation cut as a function of the truth p_T (right panel) or η (left panel). The truth values are chosen here in order to be sensitive only for the isolation differences but not for any differences in η or p_T. It can be seen that the efficiency is approximately flat in p_T and always above 96 %, for which the cut was tuned to, and only small differences (<3 %) between fast and full simulation are visible, with respect to the statistical uncertainties. The η dependence of the efficiency shows also a mainly flat behavior, except for the crack region at about $|\eta| = 1.47$ due to some bin migrations and the endcap region ($|\eta| > 1.52$) where the fast simulation drops to efficiencies beneath 95 %, which is not visible for the full simulation. These differences are caused by the isolation discrepancies, that are larger for this η region as for the other regions.

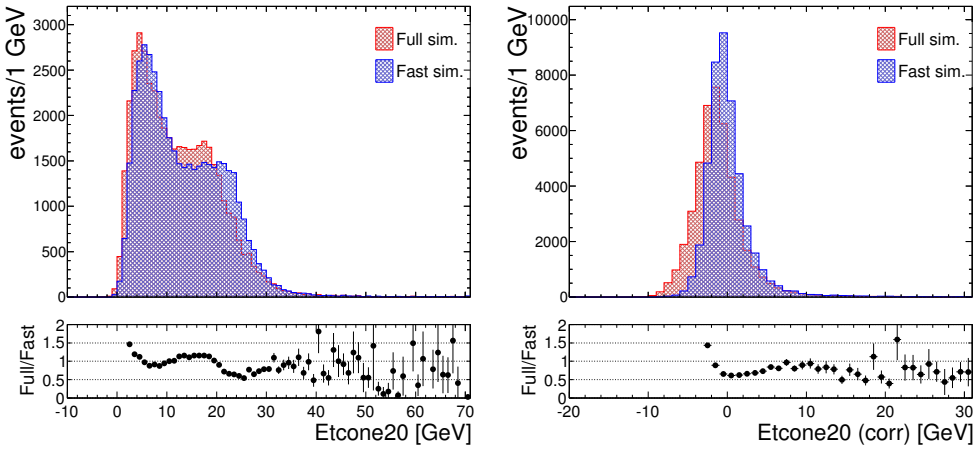

Figure 6.7.: Comparison of uncorrected (left) and corrected (right) $E_{T,Cone20}$ of the W' 3 TeV sample between AtlfastII (blue) and full simulation (red).

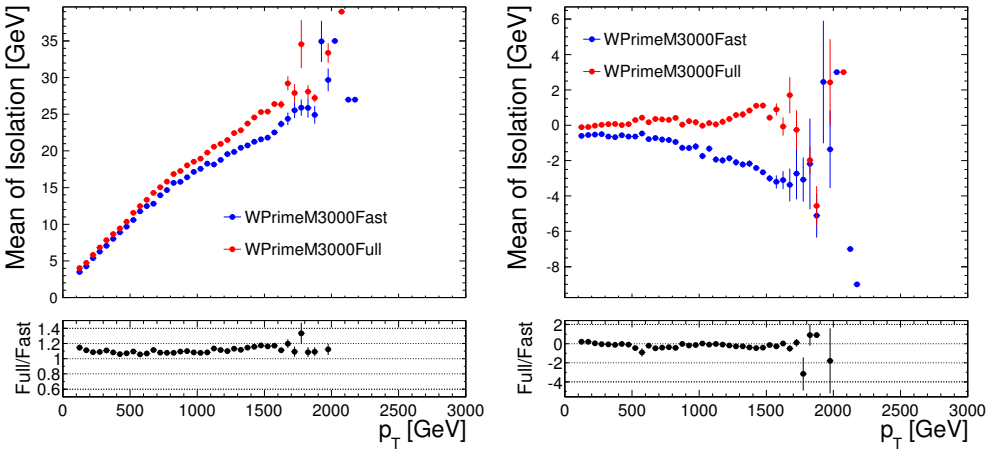

Figure 6.8.: Comparison of uncorrected (left) and corrected (right) mean of the $E_{T,Cone20}$ distribution as a function of p_T for the W' 3 TeV sample between AtlfastII (blue) and full simulation (red).

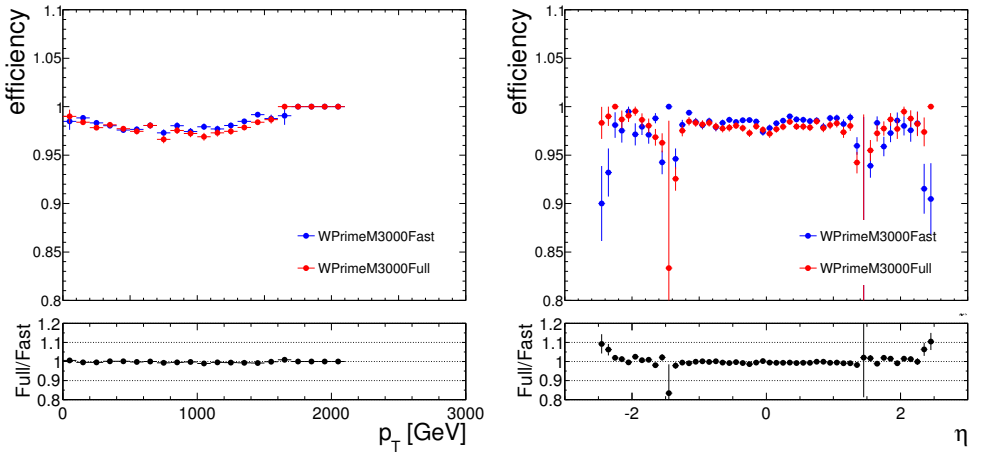

Figure 6.9.: Comparison of isolation efficiency as a function of p_T (left side) and η (right side) of the W' 3 TeV sample between AtlfastII (blue) and Full simulation (red).

The idea is to correct the isolation value of the fast simulation in order to agree with the full simulation. Therefore the p_T dependence of the uncorrected isolation is fitted for fast and full simulation in four bins of $|\eta|$ with a linear fit of the form:

$$y = ax + b \ . \tag{6.2}$$

The function to correct the isolation is then given by:

$$Iso_{full} = Iso_{fast} + n \cdot p_T + C \ , \tag{6.3}$$

$$\tag{6.4}$$

where $n = a_{full} - a_{fast}$ and $C = b_{full} - b_{fast}$ are so-called fudge factors. The results of the fits are shown in figure 6.10.

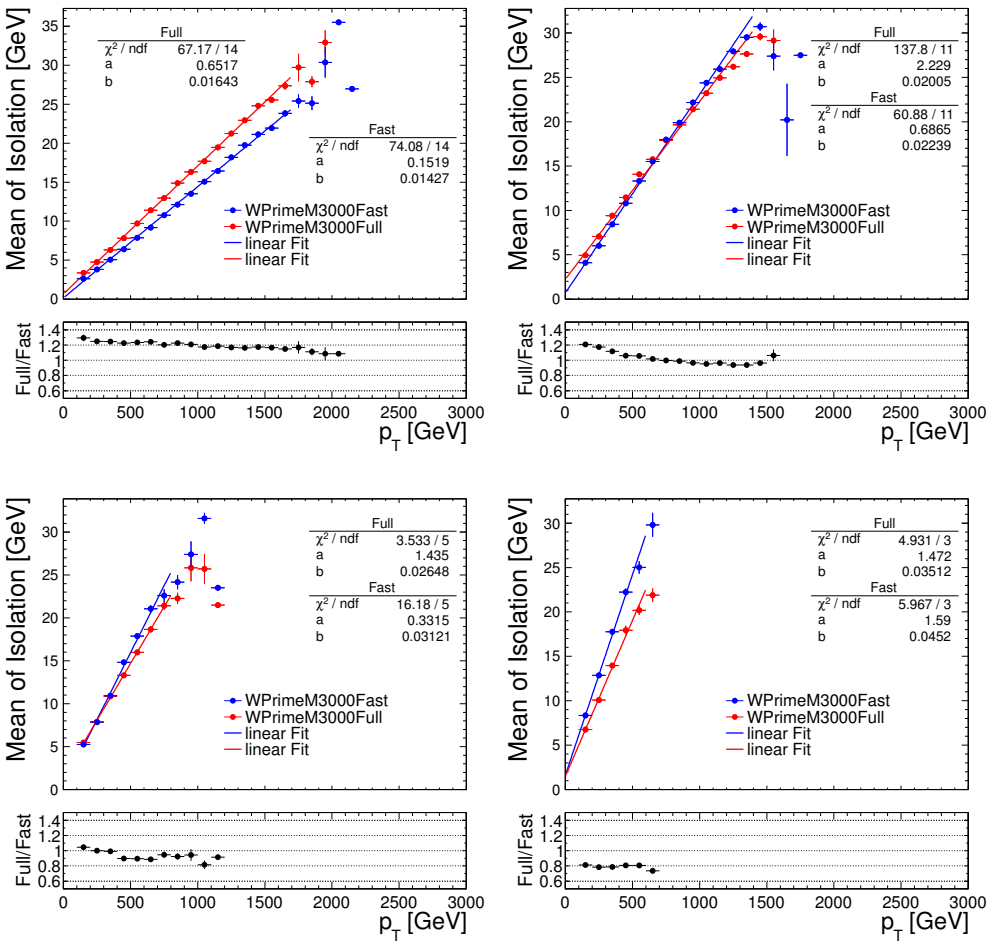

Figure 6.10.: Mean of the $E_{T,Cone20}$ distribution as a function of p_T in four bins of η with an linear fit applied. Top left: $|\eta|$ <0.8. Top right: 0.8< $|\eta|$ <1.37. Bottom left: 1.52< $|\eta|$ <2.01. Bottom right: 2.01< $|\eta|$ <2.47.

There it is also visible, that the average discrepancies between fast and full simulation grow for higher η regions. The used fit ranges are varied for the different η bins and are chosen to get sufficient entries in each p_T bin. In table 6.4 the calculated fudge factors are listed. After the fudge factors are applied to the fast simulation,

η-region	n	C
$\lvert\eta\rvert$ <0.8	0.0022	0.5
0.8< $\lvert\eta\rvert$ <1.37	-0.0023	1.5
1.52< $\lvert\eta\rvert$ <2.01	-0.0047	1.1
2.00< $\lvert\eta\rvert$ <2.47	-0.012	-0.1

Table 6.4.: Calculated fudge factors for different bins of η.

the isolation distribution for fast and full is in better agreement as it is shown in figure 6.11, even though the fudge factor only corrects the shift in the distributions and not the shape differences, which still can be seen in the corrected isolation variable. Also the p_T dependent isolation of the fast simulation matches better with the full simulation, as displayed in figure 6.12.

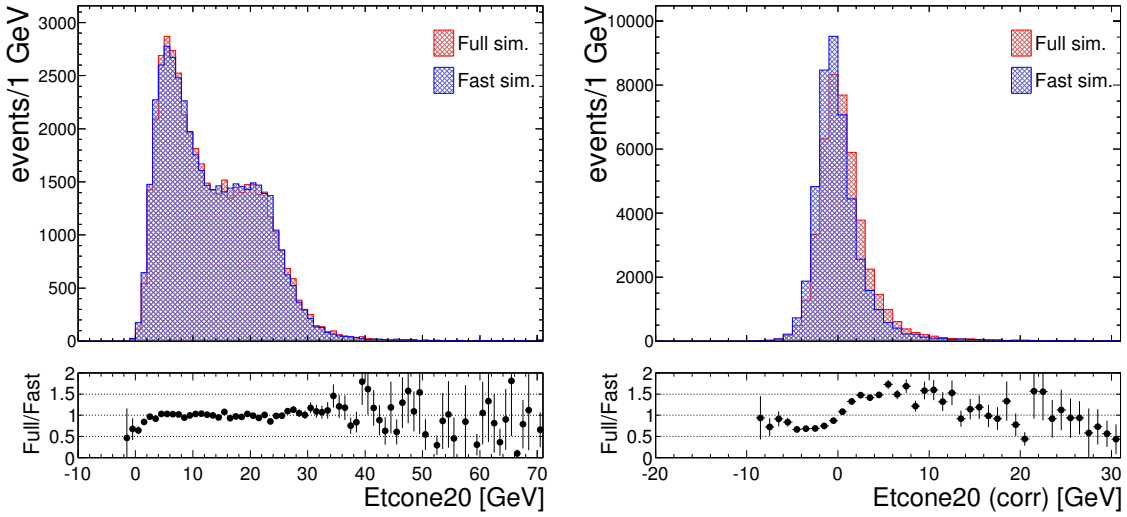

Figure 6.11.: Comparison of uncorrected (left) and corrected (right) $E_{T,Cone20}$ of the W' 3 TeV sample between AtlfastII (blue) and Full simulation (red) with applied fudge factors.

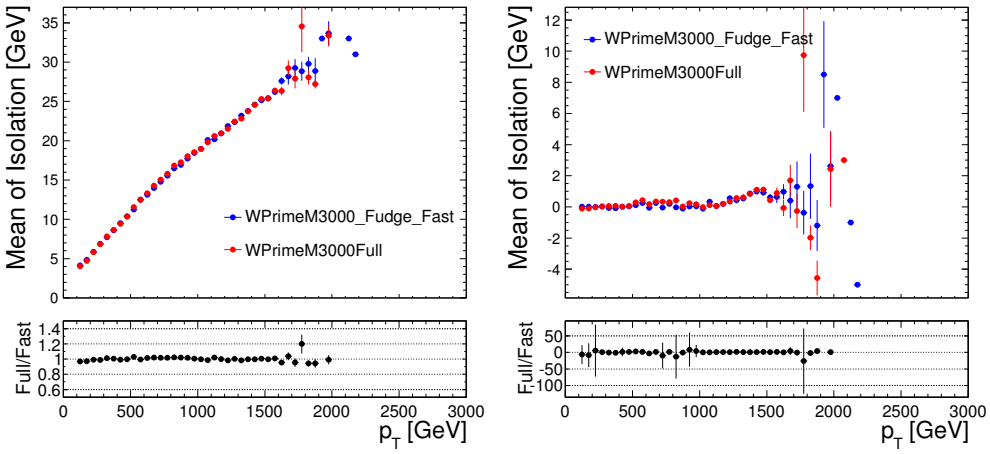

Figure 6.12.: Comparison of uncorrected (left) and corrected (right) $E_{T,Cone20}$ as a function of p_T for the W' 3 TeV sample between AtlfastII (blue) and Full simulation (red) with applied fudge factors.

To check if the fudge factors also work for the other background samples, figure 6.13 shows the isolation for the W^+(2500 GeV$< m(W^+) <$ 3000 GeV) sample with and without fudge factors. It can be seen that the differences decrease, as well.

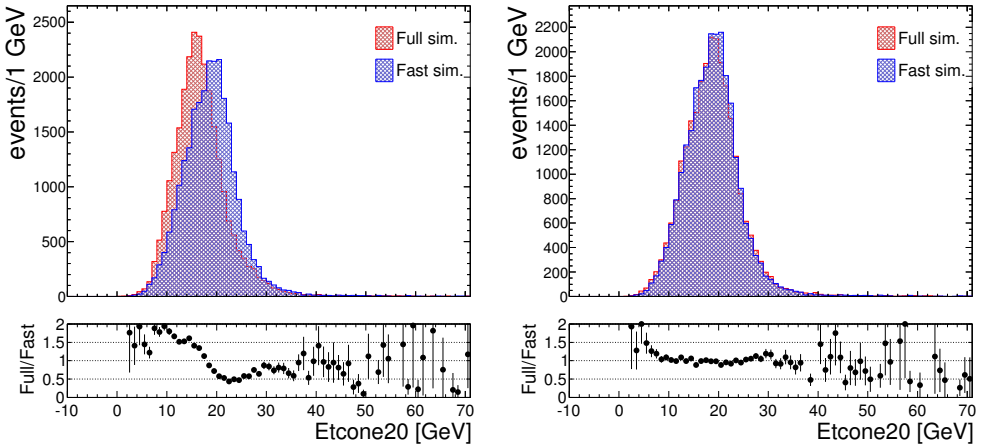

Figure 6.13.: Comparison of $E_{T,Cone20}$ for the W^+(2500 GeV$< m(W^+) <$ 3000 GeV) sample between AtlfastII (blue) and Full simulation (red). Left: without fudge factors. Right: with fudge factors.

6.5.3. Resolution comparison

A further comparison is made for the resolution. Therefore the normalized energy difference between reconstructed and generated energy ($\frac{E_{truth}-E_{rec}}{E_{truth}}$) of an electron is calculated as a function of the truth energy. This is shown in the right (left) plot in figure 6.14 for the full (fast) simulation. The sharp edge seen between the first and second E_{truth} bin is due to the p_T cut of 125 GeV. The distribution as function of $\frac{E_{truth}-E_{rec}}{E_{truth}}$ has its maximum at zero and falls to both sides. In order to extract the resolution out of these two dimensional histograms, each E_{truth} bin is projected to the y-axis, and the (arithmetic) mean and standard deviation is calculated. This standard deviation is then taken as the energy resolution. The result is shown in figure 6.15. The comparison shows, that the resolution is slightly bigger for the fast simulation. Also added in this figure is the systematic up and down variation of the energy smearing, described in section 6.4. It can be seen that the differences are covered by the uncertainty and therefore no further corrections are applied.

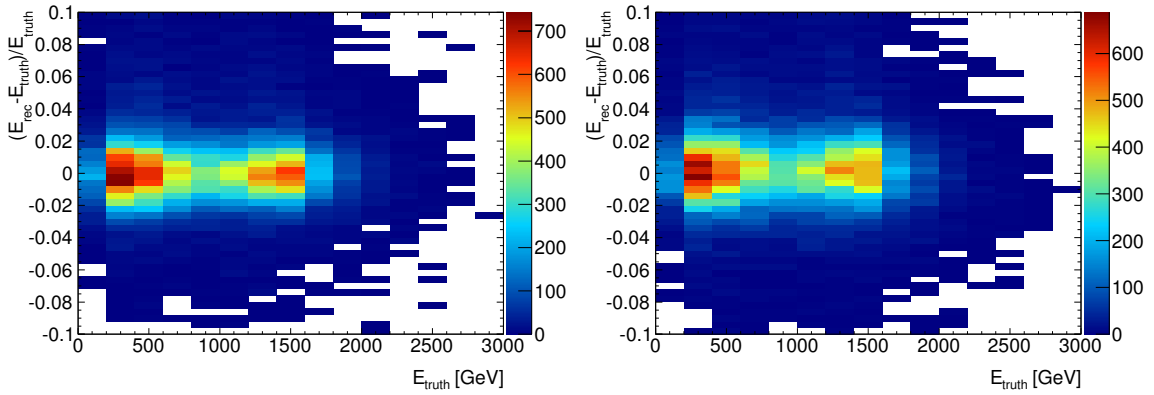

Figure 6.14.: Shown on the left (right) side is $\frac{E_{truth}-E_{rec}}{E_{truth}}$ as function of truth energy for the full (fast) simulated W' 3 TeV signal sample.

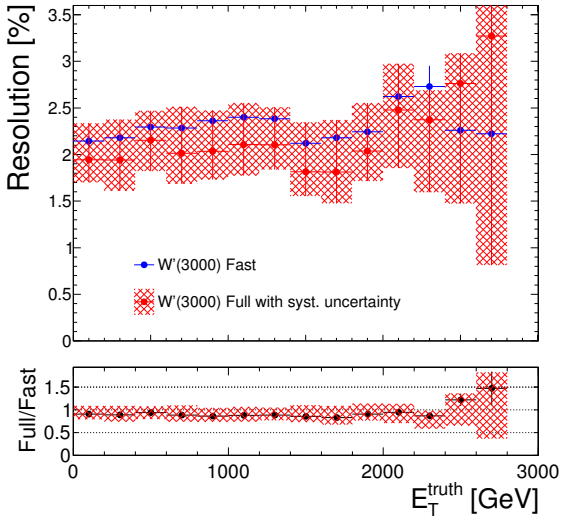

Figure 6.15.: Comparison of the resolution as function of truth energy of the W' 3 TeV signal sample between AtlfastII (blue) and Full simulation (red), including systematic uncertainties from the smearing of the electron energy.

In summary, the comparison between fast and full simulated Monte-Carlo samples shows differences in shower shape variables, isolation and resolution. The impact of these discrepancies on the selection is below 1%, because the cuts on the variables, where differences occur, are outside the range of the differences. Nevertheless differences in the isolation are corrected by using fudge factors and thus forcing the isolation of the fast simulation to agree with isolation of the full simulation. Absolute differences in the resolution of about 0.35% are covered by the systematic uncertainty of the electron energy smearing and are therefore not corrected.

7. Background estimation

In every search for new physics the ultimate goal would be to have no background. This is unfortunately not possible since there are processes, that have the same signature in the detector than the one which is searched for. Also misidentification of jets as electrons can lead to selected events, that do not origin from any signal process. Therefore it is very important to estimate this background as precise as possible.
This chapter describes the background from real electrons, meaning background from processes that leave similar signatures in the detector as a hypothetical W', and also so called fake background, which is the background from objects misidentified as electrons.

7.1. Background from real electrons

The background from real electrons is estimated with Monte-Carlo simulations, which were described in chapter 6. In the following sections an enumeration of the different processes is given, which lead to electrons, that can pass the selection. It is also possible, that the high E_T^{miss}, needed to pass the selection is "faked" from high energy particles which leave the detector acceptance and therefore leave no measurable energy in the calorimeters. For the real electron background only events are taken into account, where real electron from W bosons[1] occur. This is done by using the generator information, where the parent information of the electrons is given.

W background

The biggest background source is given by the SM W decay, because the electron and neutrino of a W decay leave the same signature in the detector as a hypothetical W' boson and thus can pass the selection cuts. Not only the electron decay channel from the W can contribute to the background, also the τ lepton channel, where the τ decays within the detector to a high energetic electron.
Since this is one of the largest backgrounds a precise description over a wide energy range is needed. To achieve this the Monte-Carlo samples used, are produced for different mass and p_T bins, as mentioned in section 6.3. The difficulty is, to avoid double counting. Applying cuts on p_T and the mass of the W boson on generator level, it is possible to gain more statistic, without double counting any events. Figure 7.1 illustrates the cuts used on mass and p_T, whereas "bulk sample" means the inclusive sample. After selection and reweighting to the data luminosity it is possible to gain complete distributions by stitching (adding) the samples together, which is

[1] Also events with a W decay to a tau lepton are considered, if the tau lepton decays into a electron.

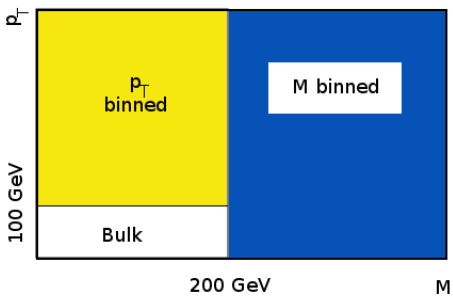

Figure 7.1.: Illustration of truth cuts, applied to W and Z Monte-Carlo samples to avoid double counting.

exemplarily shown in figure 7.2. There the stitched m_T distribution is shown for some (not all) W Monte-Carlos.

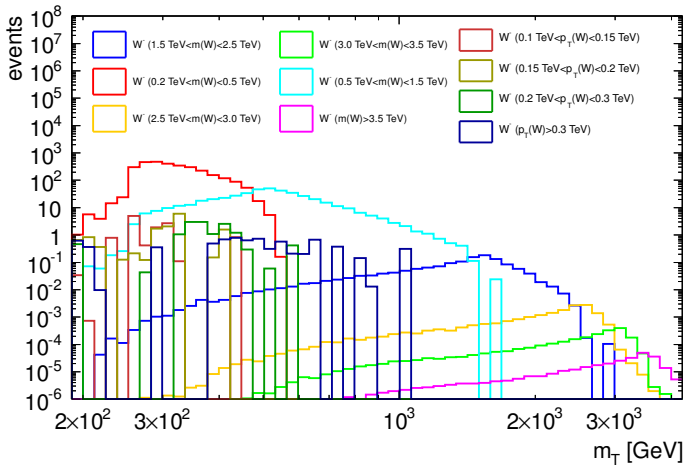

Figure 7.2.: Transverse mass spectrum for mass and p_T binned W background samples to illustrate stitching of the samples. Due to clarity reasons only the samples used for the decay into electrons are shown.

Diboson background

Events where two W bosons, two Z bosons or one W and one Z boson occur, are so called diboson events. The production processes, that can lead to such an event are shown in figure 7.3. The bosons can decay into electrons, which leads to events with up to four electrons. It is possible that some of this electrons deposit their energy in insensitive detector regions and are not reconstructed, thus faking E_T^{miss}. Given

one identified electron with high p_T, that passes the selection, the event contributes to the background. In addition events have to be taken into account where only one W decays leptonically and the other boson hadronically, which will also lead to the same signature as the signal signature. Also events where the boson decays into a τ lepton can contribute to the background, as it is possible for the τ leptons to decay into electrons. In figure 7.4 the different m_T distributions are shown for the leptonic decay channel of the WW, WZ and ZZ samples (here without the cut on m_T). It can be seen that the dominant background of this three is the WW background. The other two are suppressed because the Z decay into two electrons is suppressed by the veto of events with more than one electron, that has a p_T above 20 GeV. The sharp edge in the distribution, visible at about 250 GeV, occur due to the high p_T and E_T^{miss} cut.

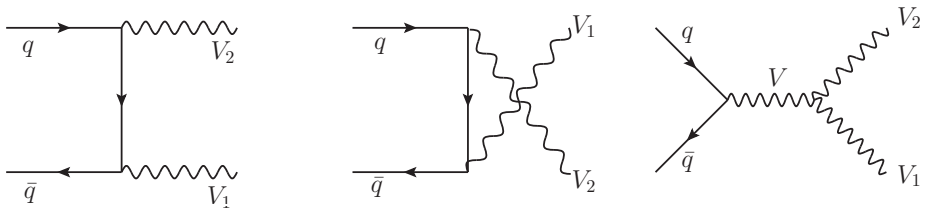

Figure 7.3.: Leading order diboson production for t-,u- and s-channel; $V, V_1, V_2 = W, Z, \gamma$. The s-channel contains only WWγ and WWZ vertices [78].

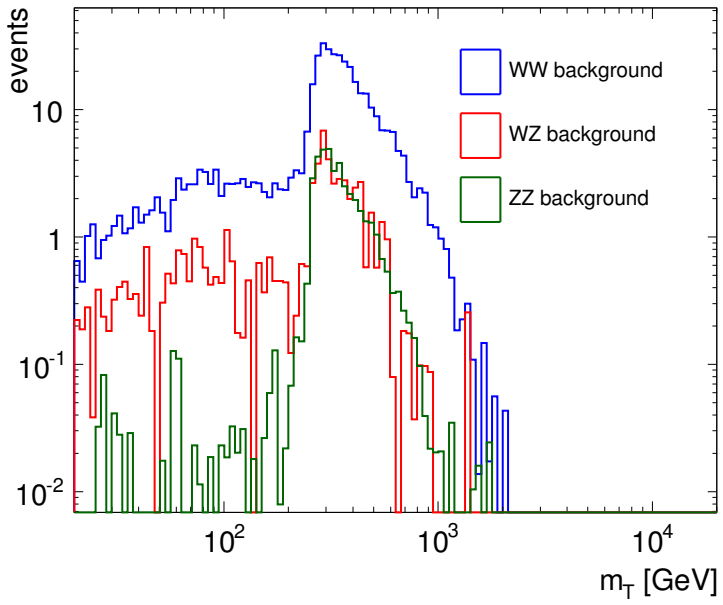

Figure 7.4.: Transverse mass distribution of the leptonically decaying diboson background split in WW, WZ and ZZ contribution.

Top backgrounds

Another background source is given by events with top decays, since the top quark decays nearly to 100 % into a bottom quark under emission of a W boson. In principle the top production can occur in pairs or in single top events. In case of the top pair production it is possible, that only one electron from a W from a top decay passes the selection and the other one does not trigger the electron veto, so that these events contribute to the background, if the W from the other top decays hadronically or leaves the detector acceptance. The single top production can be split into three different, leading order processes, that are shown in figure 7.5. In the s-channel the incoming quark-antiquark pair annihilates trough a W boson into a top-antibottom pair (or antitop-bottom pair). In the t-channel an incoming bottom quark transforms into a top quark by emitting a W boson, which is absorbed from an antiquark. In the Wt channel an incoming bottom quark absorbs a gluon and then decays into a W and top (Wt s-channel) or the bottom quark and the gluon interact over a top propagator to a W boson and top (Wt t-channel). Background contributions from the s- and t-channel occur due to the top decay into a W and b-quark, where the electron from the W boson can pass the selection. For the Wt-channel it is either directly the electron from the W boson, which passes the selection or the electron from the W boson, that comes from the top quark. In both cases only events can pass the selection, where only one identified, high p_T electron occurs in the event, since the electron veto cut would refuse events with more than one electron.
In order to have NLO contributions included, the generator used for the $t\bar{t}$ samples is `MC@NLO` which makes it important to use an additional event weight (mcevt_weight) in order to take cancelations between LO and NLO into account as it is described in section 6.1.
In figure 7.6 the m_T distribution of all top backgrounds is shown. It can be seen that the $t\bar{t}$ background has the largest contribution, due to its higher cross-section (see table 6.3). The next highest top background is the single top Wt background, since in this channel a W is produced directly, where the electrons from the W can pass the selection. The two remaining top backgrounds have nearly no events above 252 GeV because the cross-section of these decays is rather low compared with the other top backgrounds. In addition no direct produced W is present in these decays, leading to mostly low p_T electrons, that are rejected by the p_T cut.

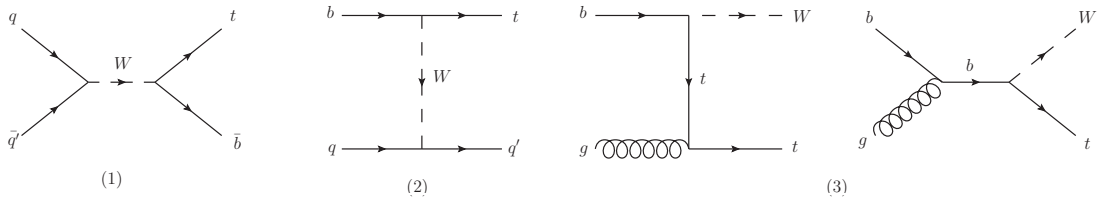

Figure 7.5.: Single top production processes in leading order. (1) s-channel. (2) t-channel. (3) Wt production

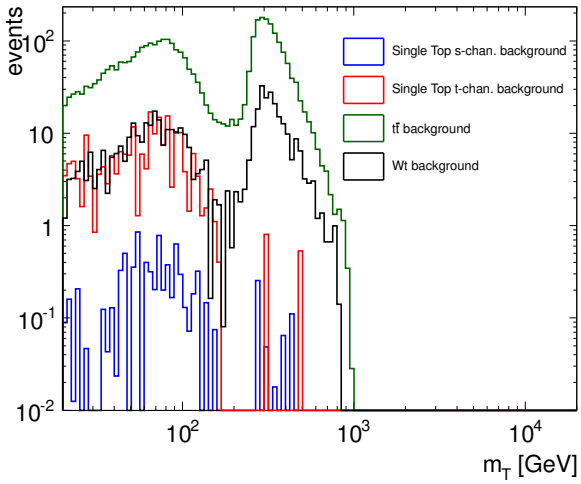

Figure 7.6.: Transverse mass distribution for top background split into different production processes. Shown is the $t\bar{t}$, single top s- and t-channel and single top Wt production.

Wγ background

Another contribution is given by the Wγ background. In principle there are two different generated processes for this background. On the one hand there is the initial state radiation of a photon from a quark, that annihilates with another quark to a W boson, on the other hand a W boson from a quark-antiquark annihilation can also radiate a photon. These two processes are not included in the W background estimation. The samples are generated with 4 different event filters. These filters only pass events with zero, one, two and three additional jets. This is another way to apply a filter for enhancing the statistics of the background.

Z background

Additional background is given through the neutral Drell-Yan process, which is the same as the charged Drell-Yan process, except that the propagator is a Z and not a W and the decay particles are two charged leptons. If one of these electrons from the Z is not reconstructed, thus faking E_T^{miss}, and the other one passes the selection, the event can contribute to the background. Not only the decay to electrons, also the decay to τ leptons is simulated, since one of the τ leptons can decay hadronically and the other one leptonically leading to an electron which can pass the selection. Nevertheless the contribution from the Z background is in the order of 1% compared to the other backgrounds.

7.2. Background from fake electrons

This section explains how the background from fake electrons is obtained using the (data-driven) matrix method. This background arises mostly due to jets which are misidentified as electrons and pass the selection, e.g. jets from multi-jet events or from top decays without real electrons. Also electrons from converted photons can contribute to this background. In the following this background will be called QCD-background, since it mostly derives from QCD processes. In principle it is conceivable that this background can also be estimated using Monte-Carlo simulations as it is done for the real electron background, but the simulation of the shower shape variables which are needed to identify these objects is very difficult due to the complexity of the hadronization. In addition this background is largely suppressed by the selection, which leads to very low statistic and a good description becomes even more difficult.

7.2.1. Description of the matrix method

The aim of the method is, to get an estimation of fake electrons, that pass the selection. The idea on how to obtain this number is to loosen some of the identification cuts for the signal selection and measure the rate for these looser objects to pass the signal selection. This rate gives a handle on the fake contribution after the signal selection. The matrix method provides a connection between the "true" number of real electrons (N_R) and the "true" number of fakes (N_F) and the measurable quantities from a loose selection (N_L) and a tight selection (N_T) via equation 7.1.

$$\begin{pmatrix} N_T \\ N_L \end{pmatrix} = \begin{pmatrix} \epsilon_R & \epsilon_F \\ 1-\epsilon_R & 1-\epsilon_F \end{pmatrix} \begin{pmatrix} N_R \\ N_F \end{pmatrix} \tag{7.1}$$

The vector on the right hand side of the equation describes the inaccessible truth quantities. The vector on the left hand side contains the measurable quantities N_L and N_T, where L indicates "pass loose but not tight" selection or short "loose fail tight" and T indicates all object, that pass the tight selection.
The entries in the matrix are called real efficiency (ϵ_R) and fake rate (ϵ_F) and denote the probability for a real (fake) electron to pass from loose to tight and are given by:

$$\epsilon_F = \frac{N_{tight}^{fake}}{N_{loose}^{fake}}, \qquad \epsilon_R = \frac{N_{tight}^{real}}{N_{loose}^{real}}\,, \tag{7.2}$$

here N_{loose} contains all objects that pass loose.
The interesting part for the QCD background is given in the first line of the matrix:

$$N_T = \epsilon_R N_R + \epsilon_F N_F\,, \tag{7.3}$$

where the first part is from the real electron contribution in the tight selection and the second part correspondents to the part from fakes. By inverting the matrix an equation for the truth variables is given by:

$$\begin{pmatrix} N_R \\ N_F \end{pmatrix} = \frac{1}{\epsilon_R(1-\epsilon_F) - \epsilon_F(1-\epsilon_R)} \begin{pmatrix} 1-\epsilon_F & -\epsilon_F \\ \epsilon_R - 1 & \epsilon_R \end{pmatrix} \begin{pmatrix} N_T \\ N_L \end{pmatrix}\,. \tag{7.4}$$

For the number of fake electrons, that pass the selection it follows then by insertion:

$$\epsilon_F N_F = \frac{\epsilon_F}{\epsilon_R - \epsilon_F} \left(\epsilon_R(N_L + N_T) - N_T\right) \tag{7.5}$$

which only contains measurable quantities.
For the loose selection all objects have to fulfill the signal selection except for the medium++ id and the isolation criteria. Instead, only loose++ without a cut on track match is required, which is similar to the criteria the trigger requires. The tight selection is the same as the signal selection.

7.2.2. Fake rate estimation

The fake rate is the probability for fake electrons to pass from the loose criteria to the tight criteria. Since, for reasons stated before, no Monte-Carlo simulations of fake electrons are available, a determination on data is done. In order to get a fake enriched sample (QCD control region) different cuts are applied:

- Suppress events from W decays:
  $\rightarrow$ $E_T^{miss} < 25$ GeV
- Suppress events from Z decays:
  $\rightarrow$ $|m_{ee} - m_Z| > 20$ GeV for electron pairs with loose++ ID and p_T >20 GeV
  $\rightarrow$ only one medium++ electron with p_T >20 GeV
- Electrons have to have matched jets [2] : ΔR <0.1
- All additional cuts are the same as in the signal selection except the E_T^{miss} and m_T cut, which are not applied in order to get enough statistics

The "real" electron contamination after applying these cuts is obtained from MC and is for the loose selection about 4% and for the tight selection up to 50%, depending on η and p_T. This contribution is subtracted for the calculation of the fake rate. The MC corrected fake rate can be seen as a function of η in figure 7.7. It is visible that the fake rate is not constant overall ranges of η. For barrel regions, $|\eta| < 1.37$ the fake rate is quite constant except a small drop in the bin before the transition region. For the endcap region three regions of different fake rates are visible. The first starting after the transition regions up to $|\eta| = 2.01$ shows also a rather flat behavior in η and comparable values as the fake rates for the barrel region, since the detector conditions are almost the same for these regions. Above $|\eta| = 2.01$ the region is no longer covered by the transition radiation detector, which leads to more fake electrons. A further increase in the fake rates is visible in the last $|\eta|$ bin because this region is additionally not covered by the most inner pixel detector. Therefore four different $|\eta|$ bins are chosen: One for the barrel region ($|\eta| < 1.37$) and three

[2] The jet algorithm used, is the anti k_T clustering algorithm, that is described in section 4.2.

for endcap regions ($1.52 < |\eta| < 2.01$, $2.01 < |\eta| < 2.37$ and $2.37 < |\eta| < 2.47$), because within these bins the fake rate has an almost flat behavior in $|\eta|$. The p_T dependence for the several η bins is shown in figure 7.8, where it can be seen that there is a decreasing behavior for higher values of p_T. The binning shown in this figure is also the binning which is used when the fake rates are applied to determine the QCD background.

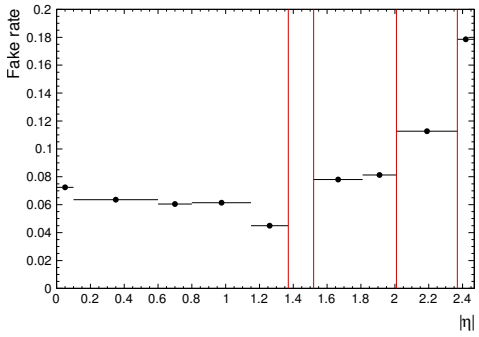

Figure 7.7.: Fake rate as a function of η determined from fake enriched data sample. Red lines indicate the chosen η binning.

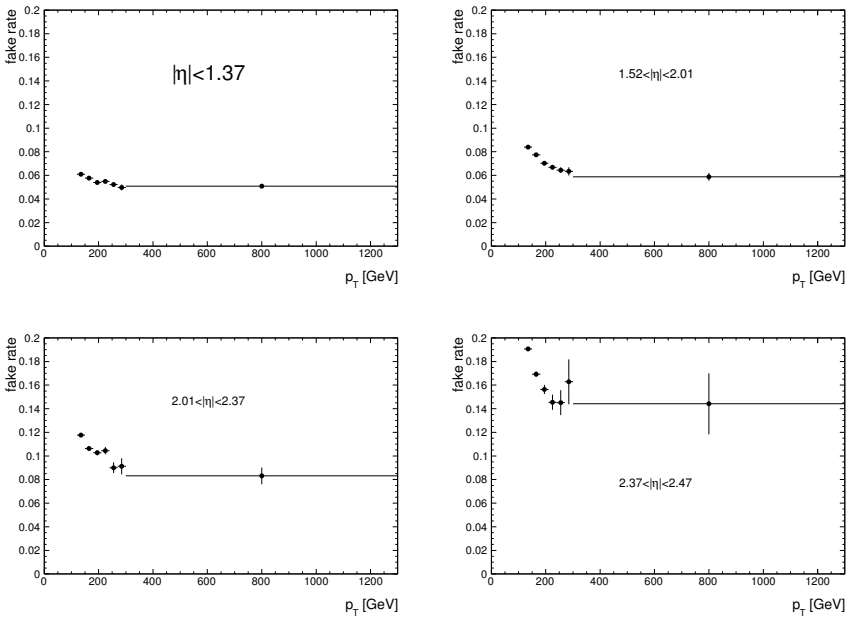

Figure 7.8.: Fake rate as a function of p_T for several η bins; determined a from fake enriched data sample.

7.2.3. Real efficiency estimation

The real efficiency is obtained by counting real electron candidates, that pass the loose selection or the tight selection (see equation 7.1). In order to make sure that only real electrons are used, the real efficiency is estimated with W Monte-Carlos and it is required that every reconstructed electron, that passes the selection has a matched real electron from the generated process without the detector simulation. For this matching it is required that $\Delta R < 0.1$. The real efficiency as a function of η can be seen in figure 7.9. The red lines indicate the bins used in η, which are the same as for the fake rate. The p_T dependence is given in figure 7.10 for two of the four η bins, the other two can be found in the appendix A.3. The drop in the real efficiency at about 230 GeV in some η bins is mostly caused due to the stitching of different W samples, where one sample runs out of statistics. Also the highest p_T bin of the lowest η bin has a high drop with large uncertainties due to low statistics. Despite of that, the real efficiency lies always between 92%-98%. These values show that the identification criteria, used in the analysis have a high efficiency, so that only maximal 8% of real electrons are rejected by the selection cuts.

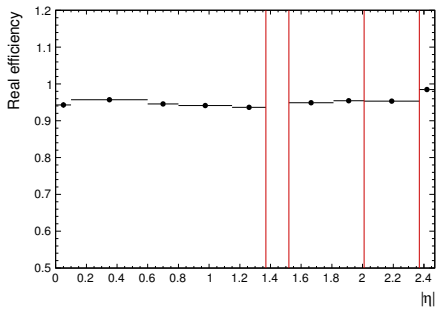

Figure 7.9.: Real efficiency as a function of η determined from W Monte-Carlo samples. Red lines indicate the chosen η binning.

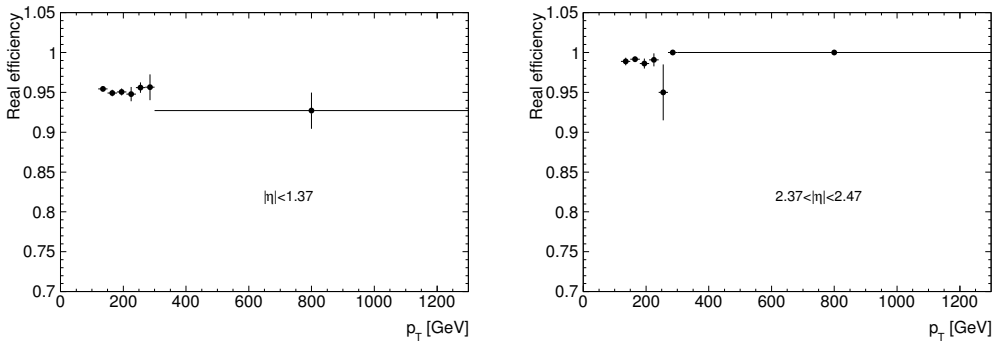

Figure 7.10.: Real efficiency as a function of p_T for two of the four η bins; determined from W Monte-Carlo samples.

7.2.4. Systematic variations for the fake rates

A main systematic uncertainty in the QCD estimate is expected to come from the choice of the fake enriched data sample. Therefore the fake rates are estimated with different variations of the cuts, used for the QCD-control region. One variation is a different E_T^{miss} cut, where the up (down) variation is done with a cut value of 35 GeV (20 GeV). Another variation is done for the Z mass window cut, where the cut is loosened (tightened) to 10 GeV (30 GeV) or completely left out. Also the veto cut, if more than one medium++ electron occurs in the event is switched off as a variation. The results for the fake rates can be seen in figure 7.11, where the default/variation ratio as function of p_T is shown for all chosen η bins. It can be seen, that the E_T^{miss} variation is with up to 22% for the last p_T and η bin dominant and all other variations are negligible. Also the statistical error of the fake rate plays an important role, especially for high p_T. Therefore only the E_T^{miss} variations and the statistical error are taken into account for the investigation of the impact on the QCD background.

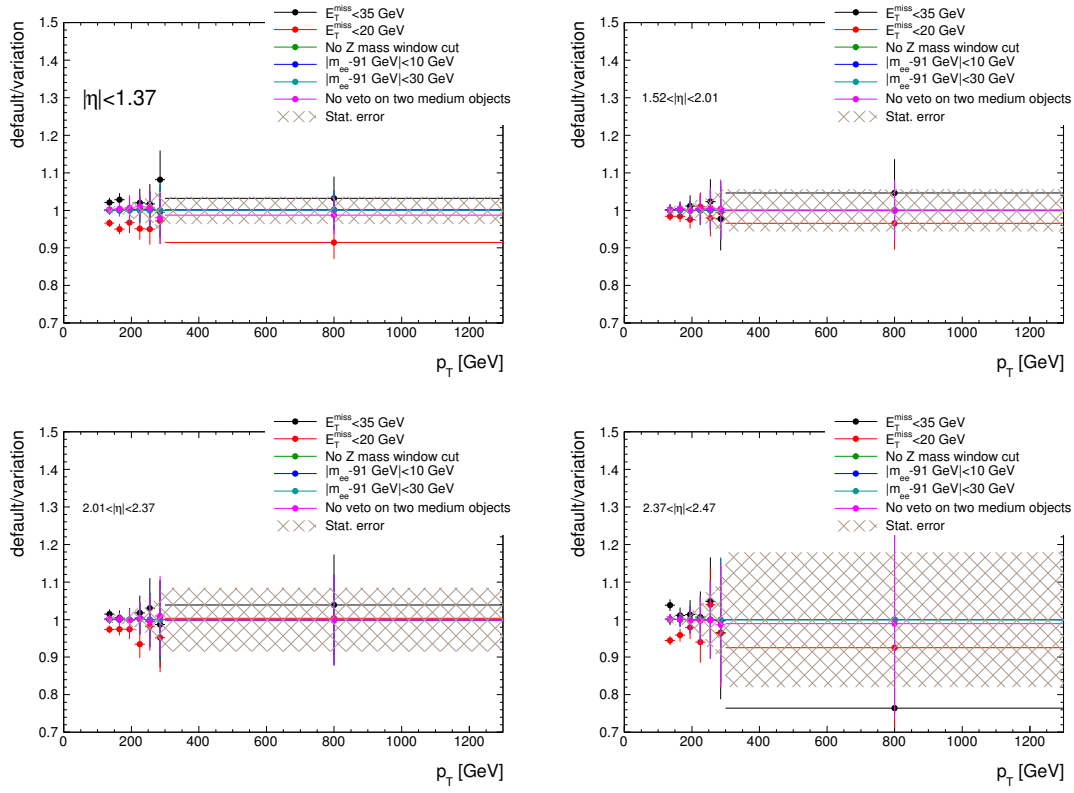

Figure 7.11.: Ratio of the default fake rate and the systematic variations as a function of p_T for different bins in η.

7.2.5. Estimation of the QCD m_T-distribution

To get the final m_T-distribution of the QCD background the calculated fake rate and real efficiencies are applied as a weight to the "loose not tight" candidates and the "tight" candidates from the main selection. These weights are given by:

$$w_L = \frac{\epsilon_F \epsilon_R}{\epsilon_R - \epsilon_F}, w_T = \frac{\epsilon_F(\epsilon_R - 1)}{\epsilon_R - \epsilon_F} \tag{7.6}$$

In figure 7.12 the final QCD m_T distribution is shown (in a logarithmic m_T binning). The distribution shows the typical falling behavior for increasing masses up to about 1 TeV where it runs out of statistics. For masses of about 250 GeV a sharp edge is visible in the spectrum, due to the p_T and E_T^{miss} cut of 125 GeV. These cuts lead also to the effect, that the slope of the distribution is getting smaller with respect to the slope at higher m_T.

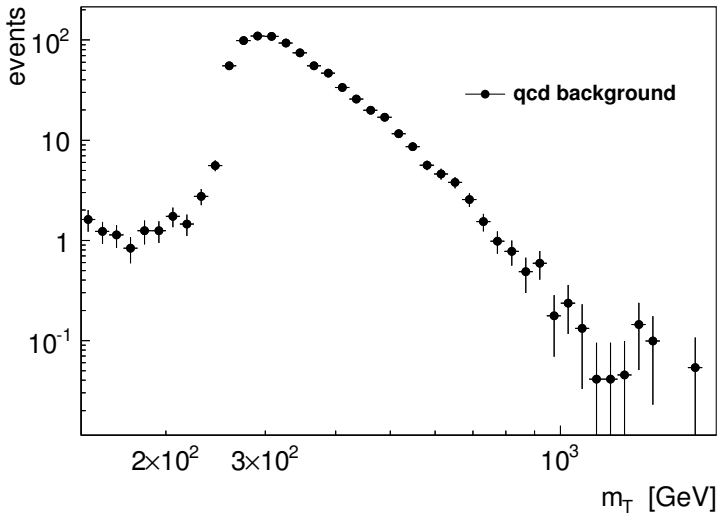

Figure 7.12.: QCD background using the matrix method.

7.2.6. Extrapolation to higher m_T

The m_T distribution of the QCD background showed in figure 7.12 runs out of statistics at about 1 TeV. It is necessary to have a background prediction for even higher masses in order to compare data with background. To achieve this an extrapolation to higher m_T is done by fitting the m_T distribution. The functions used to fit the spectrum are on the one hand a power law function (equation 7.7) as a generic function to describe falling distributions and on the other hand a so called dijet-function, see equation 7.8. The dijet-function is an empirical function, which is found to give a

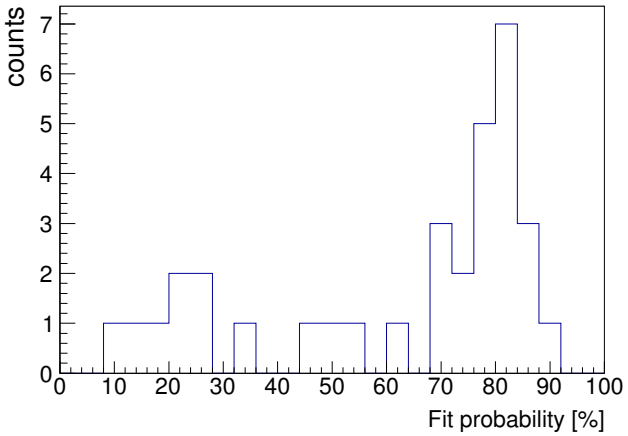

Figure 7.13.: Fit probability of converged fits used for the extrapolation of the QCD-background.

good description of QCD background [79].

$$\text{Power law: } f_1(m_T) = ax^b \tag{7.7}$$

$$\text{Dijet function: } f_2(m_T) = e^{-a}x^{b+c\log x} \tag{7.8}$$

The fit method used is the χ^2-method but it has to be taken into account that it is only a valid method if there is enough statistics inside every bin. Since the QCD distribution has the weights from equation 7.6 applied, the events on the y-axis of the distribution are not integer number of events. Therefore a second distribution, filled with the integer values of events, is chosen to decide which binning has to be chosen to have sufficient (more than 10 entries) statistic in every bin. This binning is then applied to the weighted distribution. Not only the fit functions are varied, also the fit range is varied from 395 GeV to 555 GeV for the lower border of the fit and for the upper border of the fit the range is varied from 827 GeV to 1155 GeV, which results in 33 converged fits. To ensure that the converged fits lead to a reasonable description of the QCD-background, the probability of the fits is shown figure 7.13, where it is visible, that most fits have values between 70% and 90%. The mean of all fits, with the standard deviation as uncertainty is shown in figure 7.14. It can be seen that for m_T values between about 375 GeV and 900 GeV the mean of the fits is in good agreement with the distribution, below this range the QCD-distribution levels off due to the p_T and E_T^{miss} cut. The uncertainty band (red band in the plot) is between 400 GeV and 700 GeV very narrow, since the intersection of all the fits lies in this region, so that the variance is very small. For higher values the single fits start to spread as it is reflected in the growing of the error of the mean. The final extrapolated distribution is given by stitching the pure distribution without fit with the mean of the fits at 850 GeV.

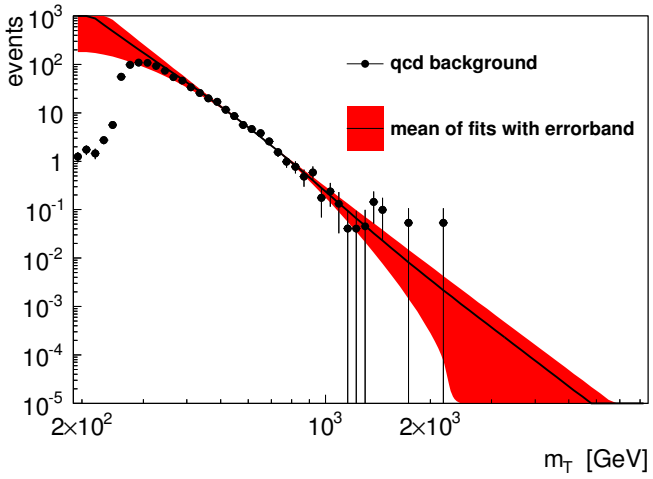

Figure 7.14.: Fitted m_T distribution with lower fit range variation from 395 GeV to 555 GeV and upper fit range variation from 827 GeV to 1155 GeV and two different fit functions.

7.3. Background uncertainties

This section focuses on the estimation of systematic uncertainties of the backgrounds described before. In the following, the influence of the systematic uncertainties are investigated for integrated numbers of events, where the integration starts at certain lower bounds (m_T^{min}). The reason, to choose these m_T^{min} thresholds is given by the search strategy, which will be explained in chapter 8.

7.3.1. Systematic uncertainties for real electron background

For the simulated background the dominant uncertainties are given by the uncertainties of the correction factors (described in section 6.4) and calibration (see chapter 4) applied to the simulation. In the following an estimation of these uncertainties is described for all single corrections.

Jet energy scale and resolution uncertainty

The jet energy calibration, which is described in section 4.2, can be varied by diversifying the nuisance parameter within their uncertainties. The jet calibration tool provides a method to get the quadratic sum of the relative uncertainties of the nuisance parameters (α_{jet}). This factor is then used to estimate an up and a down variation in a symmetric way as it is shown in equation 7.9. For both, the impact on the final background distribution is investigated and the larger deviation is taken as systematic uncertainty.

$$E^{jet}_{\frac{up}{down}} = E^{jet}_{calib.}(1 \pm \alpha_{jet}) \tag{7.9}$$

Since the jet energy resolution agrees for MC and data within the uncertainty a smearing is only applied for estimating the systematic uncertainty. This is done with a tool called `ApplyJetResolutionSmearing` [80]. The impact on the background distribution is then taken as systematic uncertainty.
Since the jets are not used directly, these variations only effect the E_T^{miss} calculation leading to a contribution to the final background uncertainty below 3%.

Electron energy scale and resolution uncertainty

The differences between MC and data in the electron energy scale are handled by rescaling the electron energies in MC as described in section 4.1.2. The *egammaAnalysis* tool, which is used for the energy scaling, also provides methods to vary these scales within their uncertainties. These variations were done separately for all sources of uncertainties. These sources are: the statistical uncertainty of the energy scale, the method, how the energy scale is determined, statistical uncertainties due to the presampler energy scale and material uncertainties. The impact of all these variations on the background is estimated and added in quadrature.
Also the smearing of the electron energy resolution (described in section 4.1.2) is varied up and down by one σ of the uncertainty, whereas the larger effect for the background distribution is taken as uncertainty.

Electron efficiency uncertainty

Also the scale factors for differences in the efficiencies (reconstruction, trigger and identification plus isolation) are varied up and down with their one σ uncertainties. The uncertainties are given mainly through a background determination, that is needed to determine the efficiencies. Again here for each efficiency variation the influence on the background is calculated and then the bigger of each efficiency is taken as systematic uncertainty.

Pileup uncertainties

In order to investigate the uncertainty of the pileup weight, the difference between the distribution with and without applied weight is taken as conservative estimate of the systematic uncertainty.

k-factor uncertainties

A further systematic uncertainty is given by the calculation of the k-factors. One part of the uncertainty is given by the PDF used to calculate the NLO and NNLO QCD cross-sections. The default PDF used for the NLO cross-section is CT10 NLO as described in section 6.3, for the NNLO cross-section the default is MSTW 2008 NNLO [26]. For the systematic uncertainties different NNLO cross-sections are taken into account. In addition, the uncertainty of the strong coupling constant, α_s, is taken into account and also variations of the renormalization scale are added. All

these uncertainties are calculated as a function of the W mass and the envelope of all variations is taken as the systematic uncertainty[3]. The final uncertainties are in the order of 3% for masses up to 1 TeV and grow for masses above 4 TeV up to about 25%.

Top cross-section uncertainties

The cross-section used to reweight the top Monte-Carlo samples to luminosity (shown in table 6.1 of section 6.3) do also have uncertainties, which are propagated to see the influence on the background. The relative uncertainties of the cross-section are given in table 7.1. It can be seen that the largest uncertainty is given, with about 7%, by the Wt process. In principle, these uncertainties are calculated as described for the k-factors namely by including α_s uncertainties and different PDFs.[4]. The impact of the cross-section uncertainty onto the background is determined by varying the m_T distribution up and down using these uncertainties and calculate the integrated number. The bigger difference to the default integral is taken as systematic uncertainty leading to a relative systematic of up to 1%.

background	cross-sec. uncertainty
$t\bar{t}$	$^{+5.3\%}_{-5.8\%}$ [82]
single top s-chan.	$\pm 3.9\%$ [83]
single top t-chan.	$^{+3.9\%}_{-2.2\%}$ [82]
Wt	$\pm 6.8\%$ [84]

Table 7.1.: Relative cross-section uncertainty of the used top samples.

7.3.2. Systematic uncertainties for fake electron background

In addition to the uncertainties on the real electron background it is also necessary to have an estimation of the QCD-background uncertainty. To get this estimate the final extrapolated QCD-distribution (see section 7.2.6) is taken and integrated for different m_T^{min} values. The uncertainty on the integrated number can be split into two parts: One for the region below the stitching point (850 GeV), that consists only of statistical uncertainties and one above the stitching point, that is only caused by the fitting, described before.
Further systematic uncertainties are resulting from the variations of the fake rate (described in section 7.2.4). This results in an additional distribution for each fake rate variation, which is shown in figure 7.15. The bottom plot in figure 7.15 shows the

[3] A detailed presentation, how this uncertainties are calculated is given in a talk in the W' analysis group [81]

[4] A more detailed description of how these uncertainties are calculated can be found in the references given in the table

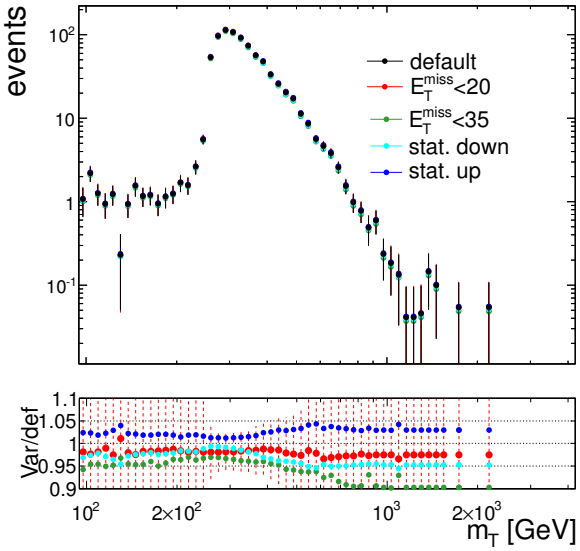

Figure 7.15.: QCD background with different fake rates for E_T^{miss} variations. Also shown is the impact of the statistical fluctuation of the fake rates.

ratio between the fake rate variations and the default method. The variations lead to a difference to the default method of up to 10% for the E_T^{miss} variations and up to 5% for the statistical variations. All four variations are also fitted and extrapolated independently as it was done for the default one. Then the integrated numbers (with different m_T^{min} thresholds) are calculated for all variations and the up and down variations are summed quadratic. In table 7.2 the integrated numbers for different m_T^{min} values are given together with the statistical and systematic uncertainties from the fit and the fake rate variations. The labels "sys_{up}" and "sys_{down}" indicate the up and down variation using the different distributions for the fake rate variation and "$\text{sys}_{\text{up}}^{\text{tot}}$" and "$\text{sys}_{\text{down}}^{\text{tot}}$" are the quadratic sum of the fit systematic and the up or down variation. An additional systematic uncertainty is applied due to differences between the default QCD-background and a QCD-background using a different method. The background done with the different method is provided by the ATLAS W' group [35]. This method, called inverse id, is based on inverting an identification cut to get a fake enriched template (also called QCD template). To remove the remaining part from real electrons, the inverted selection is also applied to the MC background and then subtracted from the QCD template. This subtracted template gives only the shape of the QCD background, the scale is calculated via a two component fit, which means that the template is compared together with the whole MC background to the data distribution. By varying the backgrounds within their uncertainties the best fitting scale factor is calculated. A comparison of the m_T and the η distribution between the inverse id method and the matrix method is given in figure 7.16 . The η distribution shows small differences for barrel regions which are growing for higher η values. For the m_T distribution the inverse id method seems to lead to a less falling behavior in m_T compared with the matrix method. These differences are mostly

$m_T^{min}[GeV]$	N_{QCD}	stat [%]	sys_{fit} [%]	sys_{up} [%]	sys_{down} [%]	$\text{sys}_{\text{up}}^{\text{tot}}$ [%]	$\text{sys}_{\text{down}}^{\text{tot}}$ [%]
252	779	1.1	0.0	4.3	2.5	4.4	2.7
336	314	1.6	0.0	5.6	2.9	5.8	3.3
399	138	2.2	0.0	6.9	3.7	7.2	4.3
502	42	3.8	0.0	8.3	4.6	9.1	6.0
564	22	5.2	0.1	8.7	4.9	10.1	7.1
843	1.9	4.3	1.0	8.7	9.8	9.8	10.7
946	0.9	0.0	1.5	9.6	12.8	9.7	12.9
1002	0.7	0.0	1.7	10.0	14.6	10.1	14.7
1416	0.08	0.0	3.0	14.3	27.4	14.6	27.5

Table 7.2.: Number of integrated events for different m_T^{min}. The uncertainties are split into statistical uncertainties (stat.), uncertainties due to fit variations (sys. Fit) and uncertainties due to different QCD background estimates (sys Up and sys Down). The last two columns are the quadratic added uncertainties.

due to the fact, that the inverse id is not tuned to any p_T or η dependence, whereas the matrix method estimates the fake rates in bins of η and p_T. For the integrated distribution the matrix method leads to an about 35% higher background which is added as further systematic.

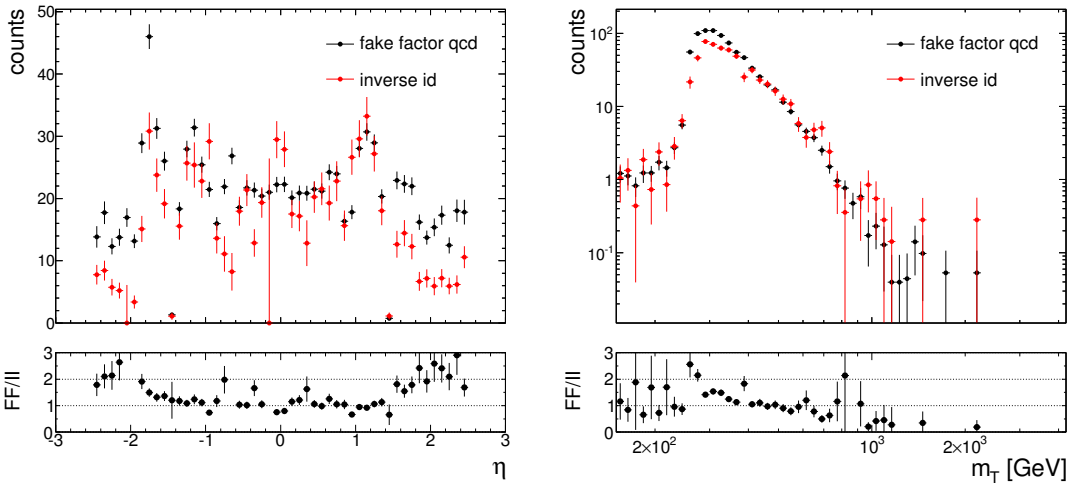

Figure 7.16.: Comparison of the QCD-background estimated with the fake factor method (FF) and the inverse id method(II) [35]. On the left panel the η distributions are compared and on the right panel the m_T distributions.

In summary, table 7.3 shows the integrated numbers of the QCD-background together with the statistical and systematic uncertainties as well as the uncertainty due to differences to the inverse id method. It should be pointed out that for m_T^{min} above 843 GeV only the extrapolation is taken to get the integrated number of events and there the statistical error, as it is defined here, goes down to zero.

$m_T^{min}[GeV]$	QCD background
252	$779 \pm 9 \quad (\text{stat})^{+275}_{-273} \quad (\text{sys})$
336	$314 \pm 5 \quad (\text{stat})^{+111}_{-110} \quad (\text{sys})$
399	$138 \pm 3 \quad (\text{stat})^{+49}_{-49} \quad (\text{sys})$
502	$42 \pm 2 \quad (\text{stat})^{+16}_{-15} \quad (\text{sys})$
564	$22 \pm 1 \quad (\text{stat})^{+8}_{-8} \quad (\text{sys})$
843	$1.9 \pm 0.1 \ (\text{stat})^{+0.7}_{-0.7} \quad (\text{sys})$
946	$0.9 \pm 0.0 \ (\text{stat})^{+0.3}_{-0.4} \quad (\text{sys})$
1002	$0.7 \pm 0.0 \ (\text{stat})^{+0.2}_{-0.3} \quad (\text{sys})$
1416	$0.08 \pm 0.00 \ (\text{stat})^{+0.03}_{-0.04} \quad (\text{sys})$

Table 7.3.: Estimated QCD contribution and uncertainties for different m_T^{min}.

7.3.3. Comparison of all backgrounds and their uncertainties

The impact of the systematic uncertainties on the final integrated number of background events is shown in table 7.4. The numbers shown here are the relative difference of a certain source of uncertainty to the default number of integrated background events. The column labeled with "scale factor" is the quadratic sum of the reconstruction, trigger and identification plus isolation efficiency uncertainty. On the experimental side it is noticeable that the energy scale uncertainty is with up to about 4% the highest systematic uncertainty. The jet resolution and energy scale uncertainty

	m_T^{min} [GeV]								
Source	252	336	399	502	564	843	946	1002	1416
Scale factor	2.3%	2.4%	2.4%	2.4%	2.4%	2.4%	2.3%	2.3%	2.4%
Resolution	0.1%	0.3%	0.6%	0.5%	0.3%	1.3%	0.6%	0.7%	1.1%
Energy scale	2.7%	3.2%	3.5%	3.8%	3%	3.5%	3.6%	3.4%	3.5%
Jet resolution	0.3%	0.2%	0.2%	0.1%	0.0%	0.1%	0.1%	0.2%	0.9%
Jet scale	0.9%	0.3%	0.4%	0.4%	0.3%	0.7%	0.3%	0.7%	0.9%
Pileup	1%	0.7%	0.1%	0.3%	0.6%	0.6%	0.4%	1.1%	3.8%
QCD	2.1%	2.1%	1.8%	1.5%	1.3%	0.8%	0.7%	0.6%	0.7%
All exp.	4.4%	4.5%	4.7%	4.8%	4.1%	4.6%	4.4%	4.4%	6%
MC stats	0.95%	1.3%	1.4%	1.1%	1.1%	2.2%	3.1%	3.6%	8.6%
k-factor	3.4%	3.2%	3.2%	4.1%	4.7%	7.2%	7.8%	7.9%	9.3%
top cross-sec.	1.0%	0.8%	0.7%	0.5%	0.4%	0.2%	0.0%	0.0%	0.0%
All added	5.7%	5.8%	5.9%	6.4%	6.4%	8.9%	9.7%	10.1%	14.0%

Table 7.4.: Overview of all systematic uncertainties on background level. The shown numbers are relative to the complete background, including all simulated background as well as QCD background.

have only a small (up to 1%) contribution to the experimental uncertainty.
On the theory side the largest contribution is given by the k-factor uncertainty with values of up to 9.3 %. The top cross-section uncertainty decreases for higher m_T^{min} since it is just a constant up or down variation of the m_T distribution. The influence of the statistical uncertainty is on the order of 1% for low m_T^{min} values which rises to about 9% for the last m_T^{min} bin. All added up quadratic, it can be seen that the systematic uncertainty is in the order of 6%, which rises with m_T up to 14%. In figure 7.17 the uncertainties are shown as a function of m_T^{min}. It can be seen that the MC statistic uncertainty and the k-factor uncertainty do have a strong dependence of m_T^{min}, whereas the other sources of systematic uncertainties are almost flat in m_T^{min}.
The final numbers of integrated background events split into the different sources can be seen in table 7.5. Added in this table are also the final uncertainties. It can be seen that the W background has the largest contribution to the background for all m_T^{min} values. The next higher background is the top background which falls very rapid with increasing the m_T^{min} threshold. The QCD background has the third largest contribution to the integrated number of events followed by the $W\gamma$ background. The lowest contribution is given by the Z background, which is highly suppressed due to the electron veto.

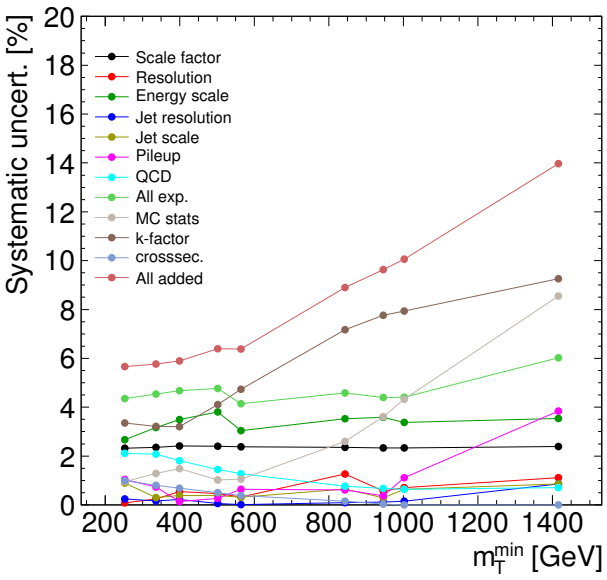

Figure 7.17.: Estimated systematic uncertainties as a function of m_T^{min} for all considered sources.

m_T^{min}	N_W	N_{top}	N_{QCD}
252	10007 ± 783 (77.1%)	1501 ± 110 (11.6%)	779 ± 275 (6.0%)
336	4072 ± 319 (75.9%)	601 ± 48 (11.2%)	314 ± 111 (5.8%)
399	2094 ± 168 (76.9%)	262 ± 21 (9.6%)	138 ± 50 (5.1%)
502	821 ± 79 (78.3%)	76 ± 7 (7.3%)	42 ± 15 (4.0%)
564	494 ± 51 (78.4%)	40 ± 4 (6.3%)	22 ± 8 (3.5%)
843	75 ± 11 (80.6%)	2 ± 1 (1.6%)	1.9 ± 0.7 (2.1%)
946	42 ± 7 (80.2%)	0.03 ± 0.17 (0.1%)	0.9 ± 0.4 (1.8%)
1002	31 ± 5 (79.0%)	0.0 ±0.0 (0.0%)	0.7 ± 0.3 (1.7%)
1416	3.9 ± 0.9 (77.7%)	0.0 ±0.0 (0.0%)	0.08 ± 0.04 (1.6%)
m_T^{min}	$N_{diboson}$	$N_{W\gamma}$	N_Z
252	448 ± 19 (3.5%)	206 ± 12 (1.6%)	42 ± 8 (0.3%)
336	251 ± 11 (4.7%)	110 ± 7 (2.1%)	23 ± 5 (0.4%)
399	151 ± 7 (5.5%)	65 ± 5 (2.4%)	13 ± 3 (0.5%)
502	75 ± 4 (7.1%)	29 ± 3 (2.8%)	5 ± 1 (0.5%)
564	52 ± 4 (8.2%)	21 ± 2 (3.3%)	2 ± 1 (0.4%)
843	12 ± 2 (12.9%)	3 ± 1 (2.7%)	0.1 ± 0.2 (0.1%)
946	8 ± 2 (15.1%)	2 ± 1 (2.8%)	0.03 ± 0.01 (0.1%)
1002	7 ± 2 (17.1%)	0.9 ± 0.4 (2.2%)	0.0 ± 0.0 (0.0%)
1416	0.7 ± 0.3 (14.3%)	0.3 ± 0.3 (6.5%)	0.0 ± 0.0 (0.0%)

Table 7.5.: Overview of integrated backgrounds for different lower integration borders (m_T^{min}). The number in braces show the relative contribution compared to the total background. The uncertainties shown include all systematic uncertainties, that are described in section 7.3.

7.4. Kinematic distributions

In this section the background distributions are compared with data. The following plots contain all recorded data from 2012 with an integrated luminosity of 20.3 fb^{-1}. The background is split into the different processes described in section 7.1 and is shown in the plots as stacked histograms, which means, that every background is added up on the previous one. The lower panel will show the ratio between data and background, to illustrate the differences. The uncertainties shown there are only including the statistical uncertainties from data and Monte-Carlo simulation. It is also important to mention that at this point only events are taken into account, where the transverse mass is below 500 GeV ("blinding"). This m_T region contains only background events and no new physics is expected there. Significant differences between background and data, in this m_T region, are more likely to come from miscalibrations, mismodeling of the simulation or mistakes done in the analysis. It is important to have such a check and to be sure that the background estimation leads to reasonable agreement with the data, because otherwise differences between background and data in high m_T regions can be interpreted as new physics, but are in reality only caused by other sources, e.g. mismodeling of the simulated background. Furthermore the kinematic distributions are investigated with and without an m_T cut of 252 GeV.

7.4.1. Resolution and binning

It is important to choose a binning, that is not smaller than the resolution and ensures enough statistic in each bin over a large range. Therefore an investigation of the resolution for the three quantities (p_T, E_T^{miss} and m_T), sensible to new physics, is done. At the left panel of figure 7.18 the relative electron p_T resolution is shown and at the right panel, the relative E_T^{miss} resolution. The resolution is determined using W Monte-Carlo simulations. It can be seen that the resolution of the transverse momentum is about 1.9% at 120 GeV and increases to about 1.6% at 500 GeV, where it remains constant. The p_T resolution is getting better for higher values, because the energy resolution increases with higher energies. The large uncertainties for bins between 500 GeV to about 800 GeV are caused by low statistics from the W Monte-Carlos samples in this region.
The E_T^{miss} resolution, shown at the right of figure 7.18, starts with a resolution of about 9% at 120 GeV and increases rapidly to about 2% at 2 TeV. The increase in the resolution is also here caused by the increasing energy resolution with higher energies.
The resolution of the transverse mass is given by a combination of the electron p_T and E_T^{miss} resolution. In figure 7.19 the m_T resolution is shown for truth transverse masses from 250 GeV to 4 TeV. It can be seen that it starts at about 5% and increases to resolutions of 2% at 2 TeV. At this point the constant term of the resolution (see equation 6.15) dominates.
The binning, that is later chosen for the p_T, E_T^{miss} and m_T distributions is provided

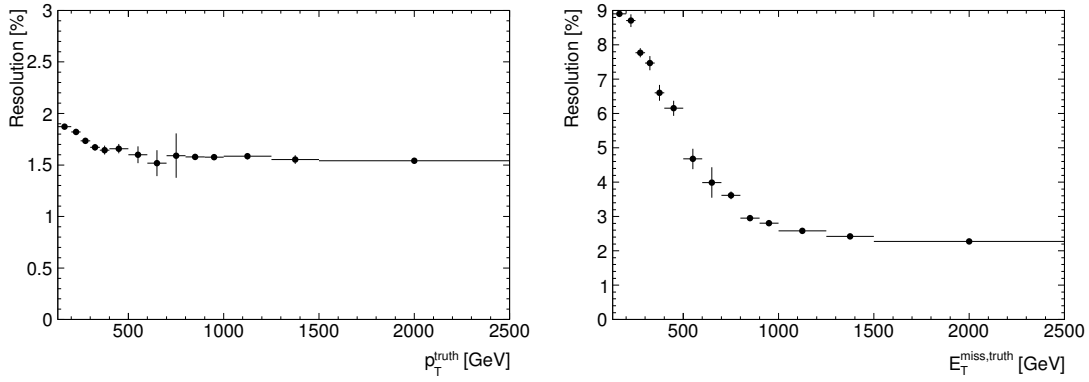

Figure 7.18.: Left: Relative p_T resolution as a function of the truth transverse momentum. Right: Relative E_T^{miss} resolution as a function of the truth E_T^{miss} (transverse momentum of the neutrino on generator level). The resolution is determined using the W Monte-Carlo simulations.

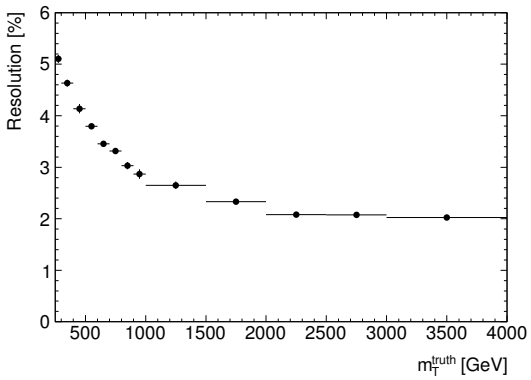

Figure 7.19.: Relative m_T resolution as a function of the truth transverse mass. The resolution is determined using the W Monte-Carlo simulations.

by the ATLAS W' group. It is a logarithmic binning, so that the relative width[5] of each bin stays the same, but the absolute width enlarges with higher values to ensure sufficient statistic in each bin. The relative bin width of the p_T, E_T^{miss} and m_T distribution is about 5.5%. Compared to the lowest electron p_T resolution, shown in figure 7.18, this is quite sufficient, but compared to the the E_T^{miss} resolution this is to small for E_T^{miss} values below 500 GeV. Nevertheless the E_T^{miss} binning is not changed for this thesis, in order to have comparable distributions with other members of the W' group. The comparison of the relative bin width with the m_T resolution shows, that the resolution is better over the whole range.

[5]The relative bin with is the bin width, normalized to the bin center: $x_{i,max} - x_{i,min}/x_{i,center}$, where x_i is the i-th bin of the particular distribution.

7.4.2. Angular properties of the selected electron

The angular information of the selected electron, given by φ, is shown with and without m_T cut in figure 7.20 . The φ distributions show an overall flat behavior for data as well as for background. Visible spikes in the W background distribution, for example at about -0.2, arise from low statistics of the inclusive $W \to \tau\nu$ sample. The ratio, shown in the bottom, shows good agreement between data and background, within the given statistical fluctuations.
The η distributions, which are given in figure 7.21, show most events in the barrel region ($|\eta| < 1.37$). For the endcap region ($1.52 < |\eta| < 2.47$) the shape shows a falling behavior. Also visible is the transition region at $1.37 < |\eta| < 1.52$, that is cut away for data and background. The falling behavior of the η distribution in endcap regions is caused by the non-linear η dependence of θ:

$$\theta(\eta) = 2\tan^{-1}\left(e^{-\eta}\right) \tag{7.10}$$

This dependence is shown in the appendix A.4. It is visible, that for barrel regions of η the dependence is approximate linear. For endcap regions, bins in η include only a very small θ range. Thus taken into account, it results, that a falling behavior in η does not imply the same behavior in θ. The comparison between data and background shows no sizable differences, with respect to the statistical fluctuations. [h]

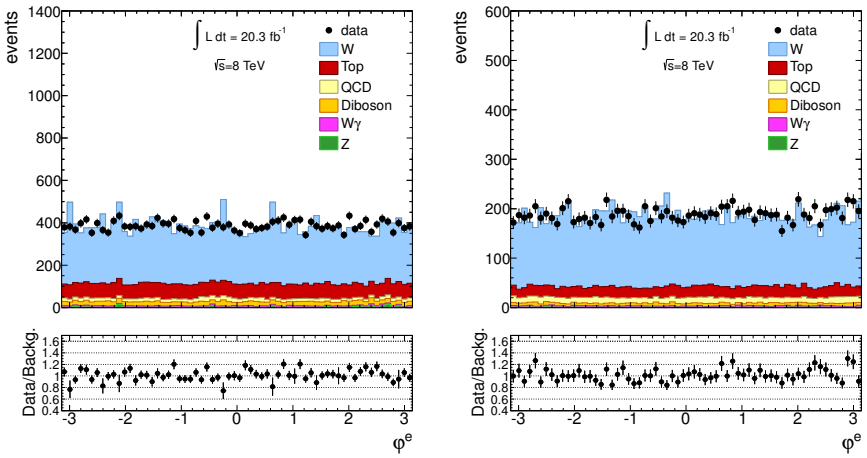

Figure 7.20.: Comparison of the electron φ distribution between data and background without (left panel) and with (right panel) minimal m_T cut, as well as their ratios.

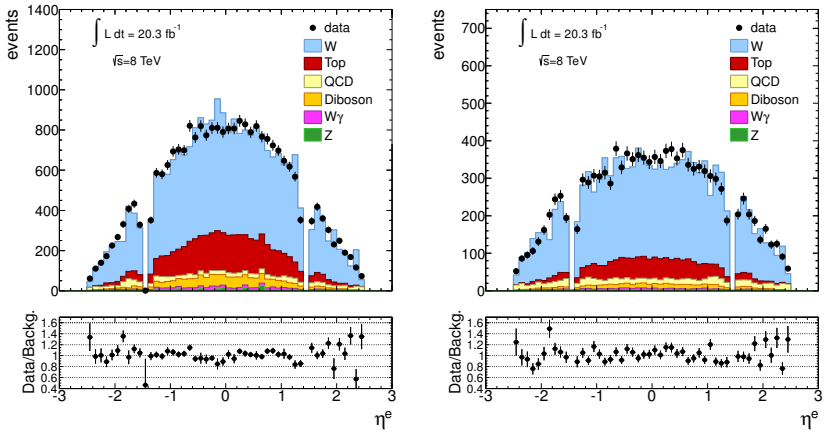

Figure 7.21.: Comparison of the electron η distribution between data and background without (left panel) and with (right panel) minimal m_T cut, as well as their ratios.

7.4.3. Transverse momentum

In figure 7.22 the p_T distributions of the selected electrons are shown in the logarithmic binning, explained in section 7.4.1. In both distributions (with and without m_T cut) the spectrum starts at 125 GeV, correspondent to the p_T cut. The first bin has fewer events than the second, because the first bin does not align with the cut. From 125 GeV on the typical strongly falling shape is visible.
It can be seen on the top left panel, that the background starts to diverge from data at about 300 GeV. This discrepancies decrease if the m_T cut is applied, as it is shown on the top right panel. In order to get a better understanding the events, that are cut away with the m_T cut, an inverse of this cut is done. The resulting p_T distribution for these events is shown in in the bottom panel of figure 7.22. It can be seen, that the agreement between data and background drops down to 40% beyond 400 GeV. This leads to the suspicion that the p_T dependence is not well described in the Monte-Carlo simulation for the m_T region below 252 GeV. In order to clarify the properties of the W bosons, contributing to this low m_T region, the p_T^W of the W bosons is estimated by:

$$p_T^W = \left| E_T^{miss} \begin{pmatrix} \cos(\varphi_\nu) \\ \sin(\varphi_\nu) \end{pmatrix} + p_T^e \begin{pmatrix} \cos(\varphi_e) \\ \sin(\varphi_e) \end{pmatrix} \right| \tag{7.11}$$

$$= \sqrt{(E_T^{miss})^2 + p_T^2 + 2E_T^{miss} p_T \cos(\varphi_\nu - \varphi_e)}\,, \tag{7.12}$$

where φ_e is the azimuth angle of the electron and φ_ν the reconstructed azimuth angle of the missing transverse energy. In figure 7.23 the p_T^W distribution is shown without the m_T cut on the top left panel and with m_T cut on the top right panel. It can be seen that there is a peak in the distribution without m_T cut at 252 GeV, which vanishes if the m_T cut is applied. This means that there are basically two types of W

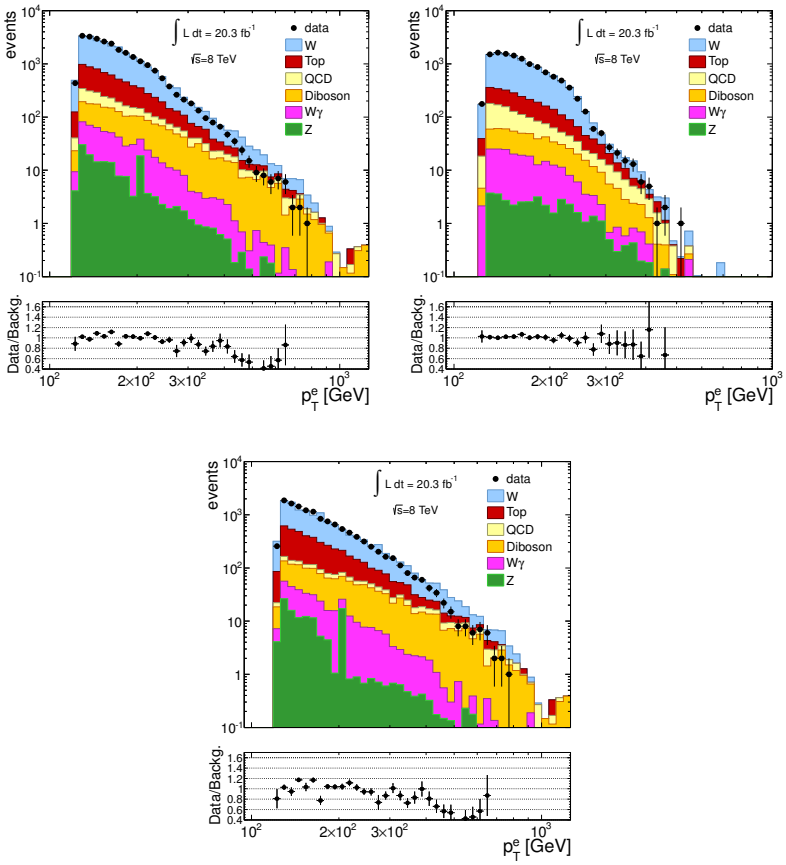

Figure 7.22.: Comparison of the electron p_T distribution between data and background without (top left panel) m_T cut, with $m_T > 252$ GeV cut (top right panel) and with $m_T < 252$ GeV cut (bottom panel); as well as their ratios.

bosons which contribute to the distributions without m_T cut: On the one hand there are heavy W bosons with masses above 252 GeV, that decay into an electron and a neutrino with a p_T >125 GeV and thus pass the selection. These W bosons have only a small boost in the transverse plain and thus populate mostly the region up to a $p_T^W = 252$ GeV. On the other hand there are light W bosons, with masses below 252 GeV but a strongly boost in the transverse plain. These W bosons are visible above a p_T^W of 252 GeV and cause a very sharp rising edge. By applying the m_T cut the strong boosted W bosons with low masses are cut away, which is visible at the top right panel of figure 7.23.
The ratio between data and background shows for the distribution without m_T cut a significant drop at p_T^W values above 600 GeV. To investigate this region of high disagreement further, the bottom panel of figure 7.23 shows the p_T^W distribution with the inverse m_T cut. As expected most low p_T^W W bosons are cut away but also here it can be seen that the difference between data and background increases above 600 GeV. With the appliance of the m_T cut these disagreements degrease, with respect to the

statistical uncertainty, as it is shown in the ratio at the top right panel of figure 7.23. It has to be taken into account that all shown distributions are only including events with transverse masses below 500 GeV but higher m_T contribute mostly to the low p_T^W region, as it was shown for the p_T^W distributions.
A reason for this visible discrepancies in the p_T^W spectrum can be the modeling of transverse momentum of the W boson in the Monte-Carlo simulation. A proper simulation is very complicated. Studies within the W' group show that there are significant differences between different generators and also other analysis groups, e.g. Z' analysis group discovered differences between generators for the p_T^Z distribution [85]. An additional contribution to the discrepancies in the p_T^W distribution could be given by the diboson background, that has a less falling shape compared with the other backgrounds. Currently ongoing studies, for example comparisons between different generators of the diboson background, show first indications that there are differences in the p_T^W distribution for different generators.

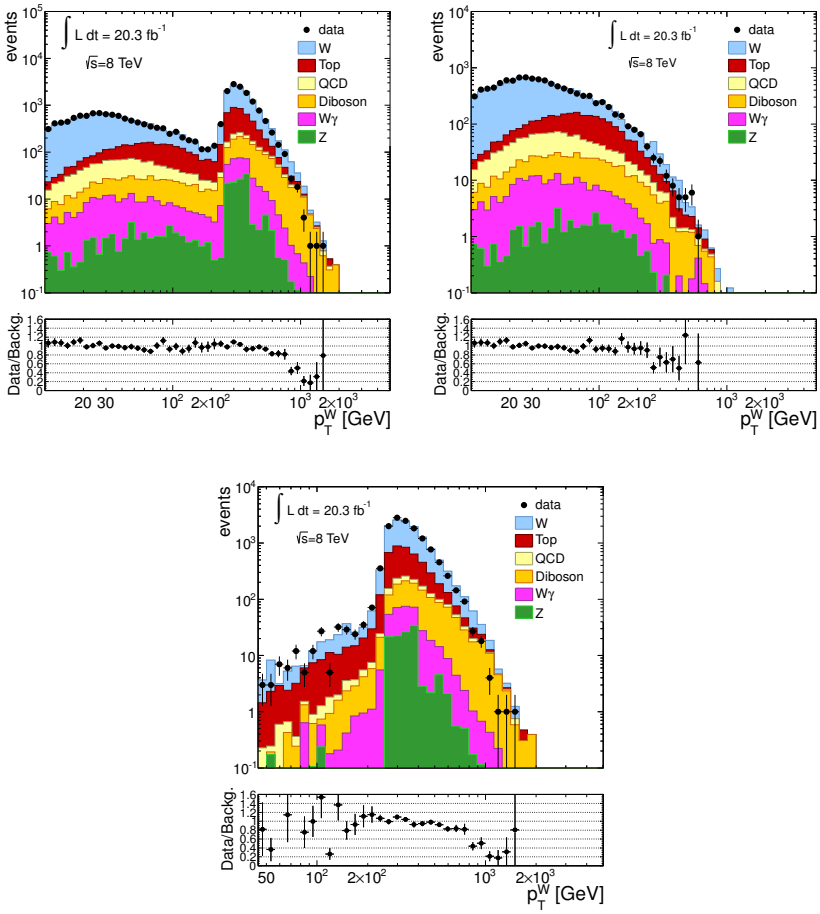

Figure 7.23.: Comparison of the W boson p_T^W distribution between data and background without m_T cut (top left panel), with $m_T > 252$ GeV cut (top right panel) and with $m_T < 252\ GeV$ cut (bottom panel); as well as their ratios.

7.4.4. Kinematic properties based on event variables

The E_T^{miss} distributions, shown in figure 7.24, on the right panel without m_T cut and on the left panel with m_T cut, show a very similar shape as the p_T distribution of the electron, since the kinematic properties of the dominant W background predicts the same transverse momentum dependence for the electron and the neutrino. The agreement between data and background is better than for the p_T distribution. There is a region at about 400 GeV where the background overestimates the data but this can also be a statistical fluctuation. The angle between the selected electron and the

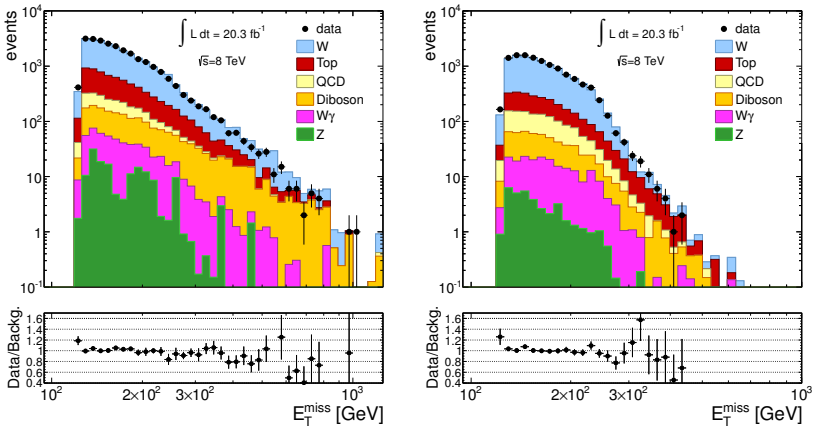

Figure 7.24.: Comparison of the E_T^{miss} distribution between data and background without (left panel) and with (right panel) minimal m_T cut, as well as their ratios.

azimuthal angle of the reconstructed missing energy is shown in figure 7.25, again without m_T cut on the left panel and with m_T cut on the right panel. In the former it is visible, that the W bosons with an m_T below 252 GeV are well distinguishable from the ones above 252 GeV. The W bosons above 252 GeV prefer to have small transverse boost, as it was shown before, which results in a back-to-back decay of the electron and neutrino. The W bosons below 252 GeV are highly boosted, which is leading to a small angle between the electron and the neutrino. After applying the m_T cut all strongly boosted, low m_T, W bosons are cut away as it is shown in figure 7.25 on the right panel. The data-background comparison shows, that the background is in good agreement with data.

The blinded m_T distribution without m_T cut is shown in figure 7.26. The distribution can be split in two parts, one above 252 GeV and one below. The sharp edge at this point is given by the p_T and E_T^{miss} cut, because at this point the W boson, produced at rest in the transverse plain, can decay into an electron and neutrino, that have p_T above 125 GeV. From this point on the distribution shows the typical strongly decreasing behavior for off shell W production. Below 252 GeV the "remains" of the Jacobian W peak at about 80 GeV are visible. As mentioned before these W bosons have to have a strong transverse boost so that the p_T and E_T^{miss} threshold can be passed, which is leading to a strong suppression. The comparison of background and

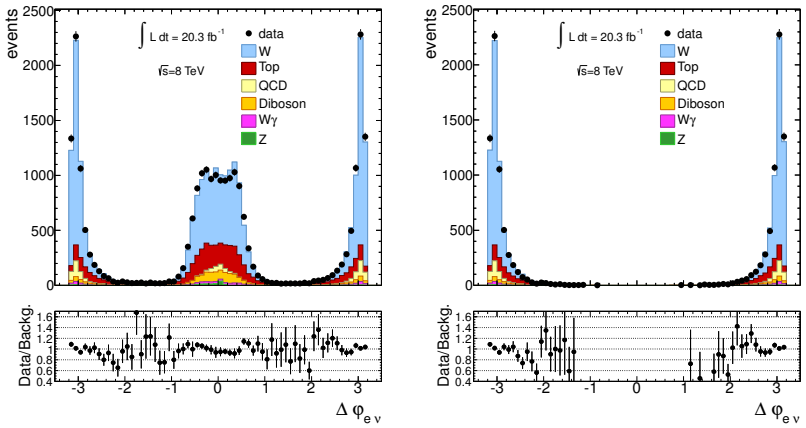

Figure 7.25.: Comparison of the $\Delta\varphi_{e\nu}$ distribution between data and background without (left panel) and with (right panel) minimal m_T cut, as well as their ratios.

data shows for regions above 252 GeV good agreement, whereas for low m_T regions statistical fluctuations dominate but within these no systematic trends occur.
In conclusion it is shown that in most investigated distributions no significant differences between background and data occur. Sizable deviations were visible in the p_T distributions from the electron and W boson, that are probably caused by a mismodeling of the p_T^W in the simulation. These differences are reduced if events below $m_T = 252$ GeV are cut away. Therefore the blinding is removed in the following and a search in high m_T regions for differences between data and background due to new physics is performed.

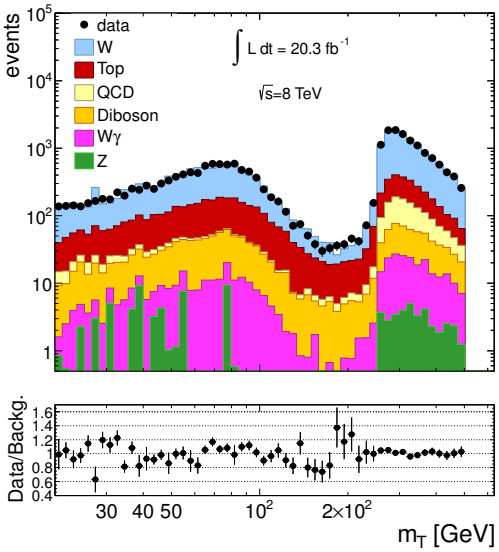

Figure 7.26.: Comparison of the m_T distribution between data and background, as well as their ratio.

8. Limit setting

In this chapter the kinematic distributions are presented without the restriction ob events with an m_T <500 GeV. The most relevant distribution is the transverse mass since signals forming a W' would appear in data as an excess above the background. Since no excess of new physics is found, it is explained how an exclusion limit on the mass of an hypothetical SSM W' is calculated.

8.1. Unblinded kinematic distributions

In order to look for differences between the background prediction and data, the unblinded transverse mass distribution is shown in figure 8.1. In the bottom of the figure the ratio between data and background is shown together with the systematic uncertainties. These uncertainties include all sources described in section 7.3. It can be seen, that the ratio of data and background is in good agreement up to about 580 GeV. At this point the data drops about 20% below the background estimation which corresponds to a 3 σ deviation if only the statistical uncertainty of the data is taken into account. Since this strong difference only appears in this bin, it is expected to be a statisticalal fluctuation. For the next three bins a falling behavior can be seen in the ratio, that is likely to be caused from the differences in the p_T spectrum of the

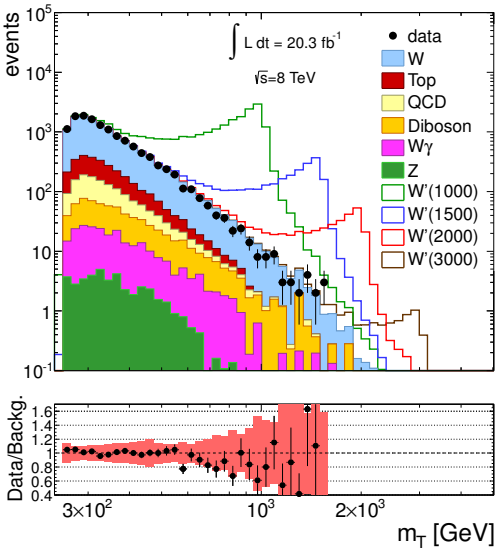

Figure 8.1.: Comparison of the m_T distribution between data and background, as well as their ratio. The red band, shown in the ratio, includes all systematic uncertainties described in section 7.3.3.

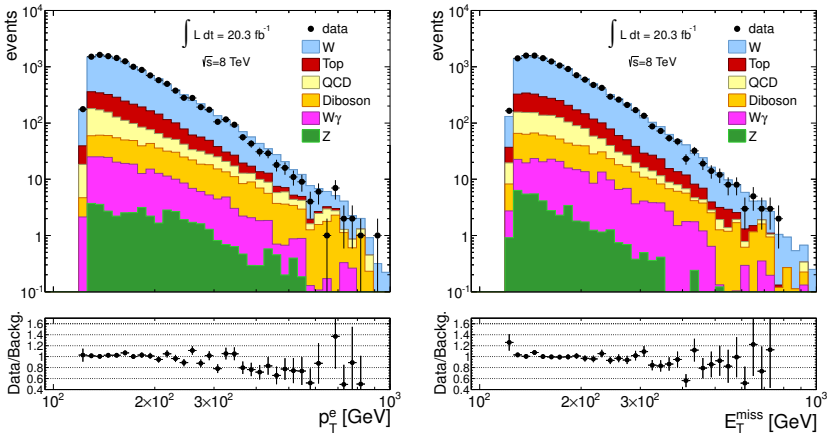

Figure 8.2.: Comparison of the electron p_T (E_T^{miss}) distribution between data and background on the left (right) panel, as well as their ratios.

electron, as discussed in section 7.4.3. In addition the plot contains also hypothetical W' signals with three different pole masses. In the data distribution it can be seen, that there are 5 events in the highest m_T bin at about 1.5 TeV. An event display of one of these events with m_T =1551.46 GeV is shown in the appendix A.6.
The unblinded electron p_T distribution can be seen on the left side of figure 8.2 with only statistical uncertainties. The differences between data and background start to increase at about 300 GeV, which shows that even with the applied m_T cut, the differences between data and background are not completely gone for high p_T. The p_T dependence of the diboson background shows also a different shape at high p_T, compared to the other backgrounds, as it was seen for the blinded distribution with $m_T < 252$ GeV.
In the right of figure 8.2 the unblinded E_T^{miss} distribution is shown. It can be seen that also for E_T^{miss} the data-background differences start to rise at about 300 GeV, whereas here the effect is not as big as for the p_T distribution. In addition it is also a significant drop of data at about 400 GeV visible, that can lead to the outlier in the m_T distribution at about 600 GeV mentioned before.
Nevertheless the discrepancies between data and background, visible in the final m_T distribution, are all covered by the systematic uncertainties (except the bin at about 580 GeV). It has to be taken into account, that the systematic uncertainties are correlated, so that it is not possible to very the bins independent within these uncertainties. The comparisons between data and background for η, ϕ, $\Delta\varphi_{e\nu}$ and p_T^W are shown without a blinding in the appendix A.5, where it can be seen that no significant differences between data and background occur. With the absence of a significant difference between data and background, in the following sections it is explained, how an exclusion limit is set on the mass of an hypothetical (SSM) W' boson.

8.2. Principle of Bayesian limits

Since no significant difference between data and background was found it is possible to set a limit on the cross-section times branching ratio (σB) for different masses of a hypothetical W'. Overall 16 different hypothetical W' pole masses are chosen and for each a limit on σB is calculated. In this analysis a Bayesian approach [86] is chosen. In principle this method is based on a "counting experiment". This is done by counting the observed number of events (N_{obs}) and the number of expected background events (N_{bg}) with $m_T > m_T^{min}$. These m_T^{min} values were provided by the official W' analysis group and are optimized to lead to best limits on σB for each different W' pole mass if only the background estimation is taken into account. Therefore every W' pole mass has a m_T^{min} assigned. For the limit calculation the expected number of events is needed. This is given by:

$$N_{exp} = N_{sig} + N_{bg}\,, \tag{8.1}$$

where N_{sig} is the number of signal events and can be expressed trough the luminosity (L_{int}), the signal efficiency (ϵ_{sig}) and the product of cross-section times branching ratio (σB):

$$N_{sig} = \epsilon_{sig} L_{int} \sigma B\ . \tag{8.2}$$

The signal efficiency is the fraction of signal events that fall within the detector acceptance, pass the event selection and have $m_T > m_T^{min}$.
Using Poisson statistics, it is possible with this information to calculate the probability, also called likelihood [87], to observe N_{obs} events given a number of expected events:

$$\mathcal{L}(N_{obs}|N_{exp}) = \frac{(N_{exp})^{N_{obs}} e^{-N_{exp}}}{N_{obs}!} \tag{8.3}$$

$$\Leftrightarrow \mathcal{L}(N_{obs}|N_{exp}) = \frac{(\epsilon_{sig} L_{int} \sigma B + N_{bg})^{N_{obs}} e^{-(\epsilon_{sig} L_{int} \sigma B + N_{bg})}}{N_{obs}!} =: \mathcal{L}(N_{obs}|\sigma B) \tag{8.4}$$

The only unknown variable in the likelihood is the signal strength σB on which the limit will be set. Therefore the parameters, that have to be determined, are the number of observed events and the number of background events, that are given by counting data, respectively background events with the different m_T^{min} thresholds, the signal efficiency and the luminosity. Since all of the parameters, except N_{obs}, have systematic uncertainties, it is important to include these into the likelihood. This is done by introducing nuisance parameters θ_i for each of these parameters. These nuisance parameters are here chosen to follow a Gaussian pdf[1]:

$$g_i(\theta_i) = \frac{1}{\sqrt{2\pi}\sigma_i} e^{-\frac{(\theta_i - \bar{\theta_i})^2}{2\sigma_i^2}} \tag{8.5}$$

[1] **p**robability **d**ensity **f**unction

where $\bar{\theta_i}$ is the central value of the parameter and σ_i is the uncertainty assigned to that parameter. For example the luminosity would have a central value of 20.3 fb^{-1} with an uncertainty of 2.8%. Multiplying the pdfs of N different nuisance parameters to the likelihood, it follows:

$$\mathcal{L}_n(N_{obs}|\sigma B, \theta_1, ..., \theta_N) = \mathcal{L}(N_{obs}|\sigma B) \prod_i g_i(\theta_i) \tag{8.6}$$

This dependency on the nuisance parameters θ_i is then integrated out (with numerical procedures) leading to a new likelihood:

$$\mathcal{L}_B(N_{obs}|\sigma B) = \int d\theta_1 ... d\theta_N \mathcal{L}(N_{obs}|\sigma B, \theta_1, ..., \theta_N)\,. \tag{8.7}$$

In this analysis three different nuisance parameters are taken into account, one for L_{int}, one for ϵ_{sig} and one for N_{bg}.
The central question of the limit setting is: How strong can a signal (σB) be, under the condition to be consistent with the number of observed events. To obtain this it is necessary to have the probability to get N_{exp} events under the condition of N_{obs} events, which is also called posterior probability. Bayes theorem [88] provides an answer for this:

$$P(B|A) = \frac{P(A|B)P(B)}{P(A)}\,. \tag{8.8}$$

In words this theorem says, that the probability of B under the condition of A is given by the probability of A under the condition of B multiplied with the probability of B divided by the probability of A. In terms of limit setting it yields:

$$P(A|B) \hat{=} \mathcal{L}_B(N_{obs}|\sigma B)\,. \tag{8.9}$$

Furthermore a probability of the data being true is needed ($P(A)$) which is here set to one. The corresponding probability to $P(B)$ is the probability of the expectation to be true, which is also called prior ($P_{prior}(\sigma B)$). For this analysis the prior is chosen to be constant in order to be consistent with other analyses [89] but it has to be taken into account that different priors can lead to different results. Summarizing, the posterior probability is given by:

$$P_{post}(\sigma B|N_{obs}) = N\mathcal{L}_B(N_{obs}|\sigma B)P_{prior}(\sigma B)\,, \tag{8.10}$$

where N is a normalization constant defined as:

$$\int_0^\infty P_{post}(\sigma B|N_{obs})d(\sigma B) = 1\,. \tag{8.11}$$

With the posterior probability it is possible to calculate a limit on σB by integration:

$$CL_{bayes} = \int_0^{\sigma B} P_{post}((\sigma B)'|N_{obs})d(\sigma B)'\,, \tag{8.12}$$

where CL_{bayes} is the predefined credibility level, which is chosen to 95% for this analysis. In other words this means that a σB found this way is with a probability of 95% consistent with the expected number of events.

8.3. Signal efficiency estimation

One input parameter needed for the limit setting is the signal efficiency. It is calculated by dividing the number of events, that pass the selection and have a $m_T > m_T^{min}$ by the generated number of signal events for each different W' pole mass. The formula is given by:

$$\epsilon_{eff} = \frac{N_{rec}}{N_{gen}} \ , \tag{8.13}$$

where N_{gen} is calculated by the complete integral of the m_T distribution for the different W' pole masses and N_{rec} is the integrated m_T distribution with the m_T^{min} cut assigned to the W' pole mass.

To get these numbers and m_T distributions for several W' pole masses, the flat signal Monte-Carlo sample is used as it is mentioned in section 6.3. The sample is only generated up to a mass of 4 TeV. In figure 8.3 the m_T distributions[2] of two W' bosons with different pole masses are shown. The left panel shows a W' with a pole mass of 1000 GeV and the right panel with 3750 GeV. For both plots the truth distribution (without any detector simulation) as well as the reconstructed distribution (with detector simulation) are shown. In addition each plot shows the ratio of reconstructed

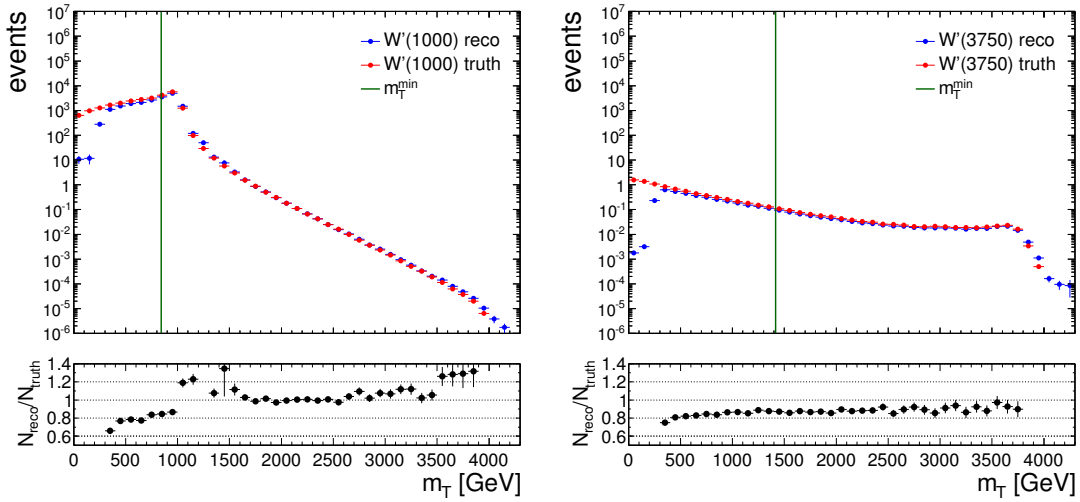

Figure 8.3.: Left: m_T distributions of a simulated W' signal with a pole mass of 1000 GeV. Right: m_T distribution of a simulated W' signal with a pole mass of 3750 GeV. Both plots include the distribution without any detector simulation (truth distribution) as well as the one from the simulated detector response (reconstructed distribution). In addition, below both plots the ratio of the truth and the reconstructed distribution is given as a function of m_T.

[2]The distributions are scaled to data luminosity.

and truth events. For the distribution of the W' boson with a pole mass of 1000 GeV the Jacobian peak at about 1000 GeV can be seen. For the reconstructed distribution, this peak is smeared due to the detector resolution, as described in section 2.2.2. The sharp edge in the reconstructed distribution at 252 GeV is caused by the p_T and E_T^{miss} of the selection. The reason that the ratio has an increasing behavior in m_T is given by bin migration: It happens that events generated in certain m_T bin migrate to a neighboring bin due to the detector resolution. In principle it is equally probable for an event to migrate to lower or higher m_T, but in a strong falling spectrum migrations to lower bins are less visible than migration to higher bins, which leads overall to a different slope for the reconstructed distribution.
The distribution on the right panel of figure 8.3 shows an high low mass tail, as explained in section 2.3. For this pole mass it is also visible that the high m_T tail of the Jacobian peak, above 4 TeV, is not simulated.
This cutoff has an small effect on the integrated numbers, used for the signal efficiency calculation, if the W' pole mass is low. To get an estimate of the impact on the highest (4000 GeV) and and second highest (3750 GeV) pole mass, the signal efficiency of the 2500 GeV sample is calculated two times with different maximal integration borders. First the integration border is set directly to the pole mass of 2500 GeV, to see the effect of cutting away the complete high mass tail. Another signal efficiency is estimated for a maximal integration border of 2750 GeV to see the effect of cutting away the tail 250 GeV above the pole mass. Former signal efficiency leads to a difference of about 5% to the default case and second to a difference of about 1%. Therefore it is decided to exclude the last two pole masses for the limit calculation, leading to the highest pole mass used of 3500 GeV.
Sixteen different pole masses are taken into account for the limit setting. The corrections, mentioned in section 6.4, also have to be applied. Most of the corrections are done, due to correct differences between Monte-Carlo and data, and thus only applied to the reconstructed m_T distribution, except the pileup weight, the k-factor and the mc_event weight which is also applied to the generated m_T distributions. Since the mc_event has no mass dependence these corrections will cancel if building the ratio :

$$\epsilon_{sig} = \frac{\int_{m_T^{min}}^{8\ \mathrm{TeV}} N_{reco}(m_T)k(m_T)w_{pileup}(m_T)w_{mc\_event}w_{reco}(m_T)dm_T}{\int_0^{8\ \mathrm{TeV}} N_{truth}(m_T)k(m_T)w_{pileup}(m_T)w_{mc\_event}dm_T} \tag{8.14}$$

$$= \frac{\int_{m_T^{min}}^{8\ \mathrm{TeV}} N_{reco}(m_T)k(m_T)w_{pileup}(m_T)w_{reco}(m_T)dm_T}{\int_0^{8\ \mathrm{TeV}} N_{truth}(m_T)w_{pileup}(m_T)k(m_T)dm_T}\,, \tag{8.15}$$

where w_{reco} stands for the weights due to differences in reconstruction, selection efficiencies and energy scale variations.
As explained in detail for the background (see section 7.3) all these corrections have uncertainties, which also lead to an uncertainty for the signal efficiency. In order to calculate this uncertainty, the m_T distribution is calculated by using the up and down varied[3] weight. These varied m_T distributions are then integrated and divided by the

[3]The variations are given by the 68%C.L. uncertainty

	$m_{W'}$ [GeV]								
	300	400	500	600	750	1000	1250	1500	1750
	m_T^{min} [GeV]								
	252	336	399	502	564	843	946	1002	1416
Scale factor	2.9	2.5	2.3	3.1	2.3	2.2	2.2	2.4	2.2
Resolution	0.4	0.2	0.4	0.2	0.1	0.4	0.3	0.2	0.3
Energy scale	3.4	2.6	1.8	1.9	1.2	2	1.1	0.8	1.8
Jet resolution	0.2	0.1	0.2	0.1	0.1	0.2	0.2	0.1	0.1
Jet Scale	0.5	0.2	0.2	0.1	0.1	0.2	0.2	0.1	0.1
Pileup	1.9	1.1	0.4	2.0	0.4	0.1	0.4	1.0	0.3
All exp.	4.9	3.8	3.0	4.1	2.6	3.0	2.6	2.7	2.9
MC stats	2.2	2.0	1.9	2.0	1.7	1.9	1.6	1.4	1.7
k-factor	0.4	0.6	0.5	0.5	0.3	1.2	0.9	1.5	2.4
All added	5.4	4.3	3.6	4.6	3.1	3.7	3.1	3.4	4.1

	$m_{W'}$ [GeV]							
	2000	2250	2500	2750	3000	3250	3500	
	m_T^{min} [GeV]							
	1416	1416	1416	1416	1416	1416	1416	
Scale factor	2.2	2.2	2.2	2.2	2.3	2.2	2.4	
Resolution	0.2	0.2	0.1	0.1	0.0	0.0	0.1	
Energy scale	1.0	1	0.7	0.8	0.8	0.9	1.0	
Jet resolution	0.0	0.1	0.0	0.0	0.0	0.0	0.0	
Jet Scale	0.0	0.1	0.0	0.0	0.1	0.0	0.1	
Pileup	0.1	0.2	0.2	0.5	0.6	0.1	1.0	
All exp.	2.4	2.4	2.3	2.4	2.4	2.3	2.7	
MC stats	1.4	1.3	1.2	1.2	1.1	1.0	1.0	
k-factor	2.7	3.9	6.6	13.0	21.0	31.0	38.0	
All added	3.9	4.8	7.1	13.0	21.0	31.0	38.0	

Table 8.1.: Signal efficiency uncertainties for different W' pole masses and m_T^{min} values. The shown uncertainty sources are the same as for background, except for the top cross-section uncertainty, which cancels by building the ratio. The uncertainties are shown relative to the default value in %.

number of generated events. The higher deviation from the default is then taken as systematic uncertainty for the signal efficiency.
An overview over all estimated relative systematic uncertainties is shown in table 8.1 and graphically in figure 8.4. It can be seen that on the experimental side the largest contributions are given by the scale factor uncertainty[4] and the electron energy scale uncertainty. On the theory side it can be seen that the k-factor uncertainty is only about 0.38% for low W' pole masses and rises with the W' pole mass to about 38%. This very large increase of the uncertainty is caused by the fact, that the integration from m_T^{min} is only done for the distribution of the reconstructed events and not for the generated ones.

To clarify this, figure 8.5 shows the ratio of the k-factor up, respectively down variation and the default case, for a W' pole mass of 1000 GeV on the left panel and a

[4]Scale factor uncertainties include uncertainties from reconstruction, trigger and identification plus isolation scale factors, as it is described for the background uncertainties in section 7.3.3.

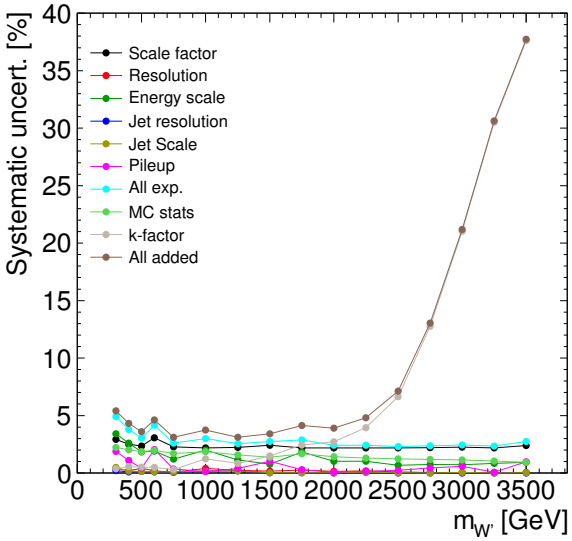

Figure 8.4.: Relative systematic uncertainties of the signal efficiency for different generated pole masses of a hypothetical W'.

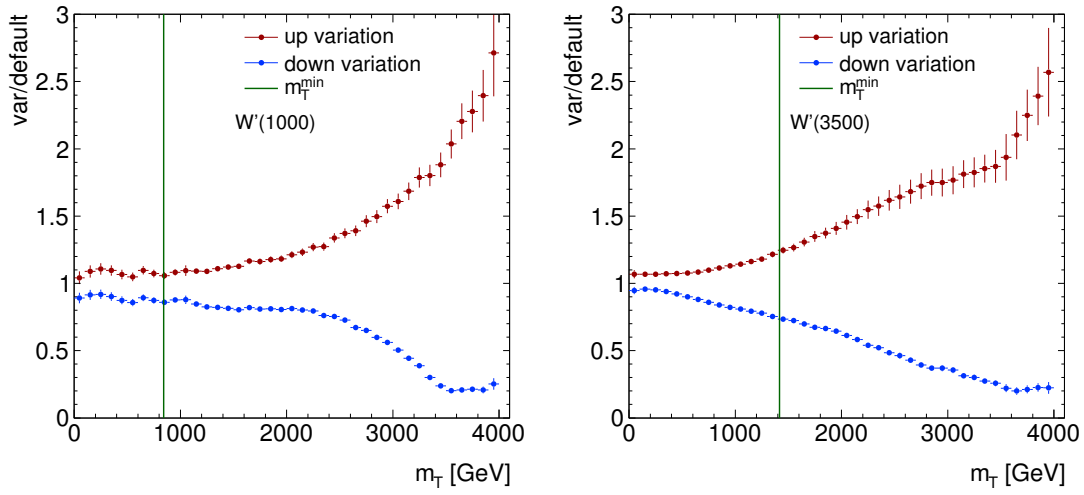

Figure 8.5.: Systematic up and down variation of the k-factor as a function of m_T. The left side shows the ratio of variation and default for a W' with a pole mass of 1000 GeV and the right side for a pole mass of 3500 GeV.

pole mass of 3500 GeV on the right panel. Also shown in these plots is the integration border m_T^{min} from which the reconstructed distribution is integrated. In order to understand the rise of the efficiency uncertainty due to the k-factor variation it is helpful to look at numerator and denominator of the signal efficiency separated. For low pole masses most of the events lay in small m_T regions, where the k-factor uncertainty is small ($< 10\%$). The k-factor variations lead therefore only to small variations of the numerator and denominator. Going now to higher pole masses the peak of the m_T distribution will also shift, leading to bigger variation of the numerator and denominator due to higher k-factor uncertainties. With bigger pole masses also the integration border m_T^{min} shifts, so that the relative variation of the numerator is slightly bigger than the one of the denominator, as shown in figure 8.6. There, the relative change between default and variation is shown for the numerator and denominator as a function of the W' pole masses. It can be seen that the differences between numerator and denominator grow slightly up to 2000 GeV due to the change of the m_T^{min} cut. At his point the numerator rises very strongly, whereas the denominator stays more about the same. The m_T^{min} does not change anymore for pole masses above 1750 GeV, but as it was explained before, a further rising of the pole mass leads to a low m_T dominated distribution. Since the numerator is not sensitive to this low m_T region, due to the m_T^{min} threshold, the difference between default and varied nominator rises strongly. The denominator is sensitive to the low m_T regions so that the k-factor variation leads to a small effect compared to the default denominator. In conclusion this shows that the numerator of the signal efficiency diverges from the denominator due to the k-factor uncertainty, leading to a high uncertainty on the signal efficiency for high pole masses. The resulting calculated signal efficiencies, with the uncertainties

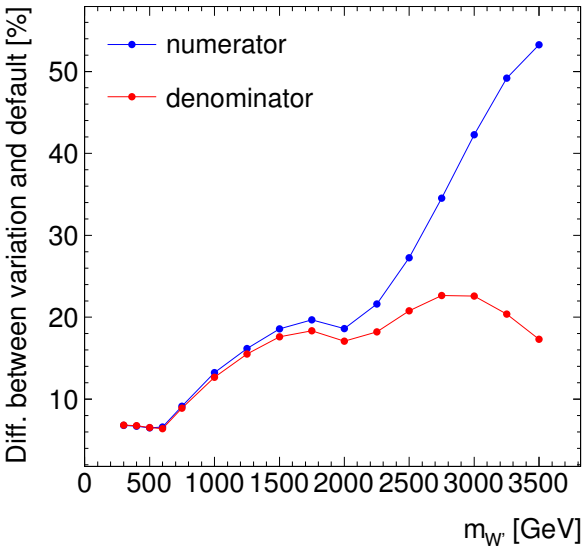

Figure 8.6.: Relative difference between the default numerator (denominator) and the varied one due to the k-factor uncertainties as a function of W' pole masses.

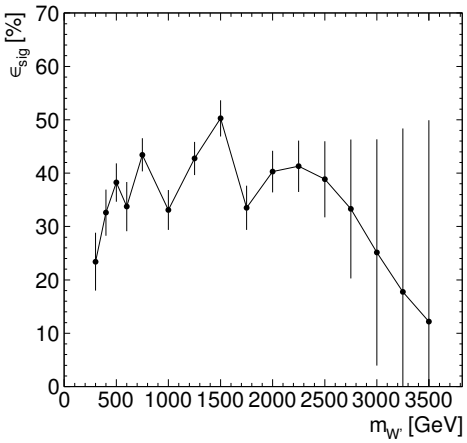

Figure 8.7.: Signal efficiency as a function of W' pole mass. The shown error bars include statistical and systematic uncertainties.

mentioned before, can be seen in table 8.2 and graphically, as a function of the W' pole masses, in figure 8.7.

In the table also the resulting number of signal events, used for the numerator of the efficiency calculation, are shown. It can be seen for $m_{W'}$ below 1750 GeV, that the signal efficiency fluctuates between 20-50%, due to the changes of the m_T^{min}. For the W' masses of constant m_T^{min}, above 1750 GeV, the signal efficiency decreases to about 12% due to the fact that for this high W' pole masses the low mass region, below the m_T^{min} cut is highly populated and such not contributing to the numerator of the efficiency.

$m_{W'}$ (m_T^{min}) [GeV]	ϵ_{sig}	N_{sig}	N_{bg}	N_{obs}
300(252)	0.234 ± 0.013	$7.62{\cdot}10^5$ ± $4.4{\cdot}10^4$	12982 ± 723	13050
400(336)	0.326 ± 0.014	$3.66{\cdot}10^5$ ± $1.7{\cdot}10^4$	5369 ± 307	5287
500(399)	0.382 ± 0.014	$1.82{\cdot}10^5$ ± $6.6{\cdot}10^3$	2722 ± 161	2633
600(502)	0.337 ± 0.016	$7.92{\cdot}10^4$ ± $4.0{\cdot}10^3$	1048 ± 67	967
750(564)	0.434 ± 0.014	$4.01{\cdot}10^4$ ± $1.3{\cdot}10^3$	630 ± 40	532
1000(843)	0.331 ± 0.012	$8.71{\cdot}10^3$ ± 326	93 ± 8	81
1250(946)	0.427 ± 0.013	$3.76{\cdot}10^3$ ± 118	52 ± 5	43
1500(1002)	0.503 ± 0.017	$1.68{\cdot}10^3$ ± 60	39 ± 4	34
1750(1416)	0.335 ± 0.014	445 ± 18	5 ± 0.7	5
2000(1416)	0.403 ± 0.016	223 ± 9	5 ± 0.7	5
2250(1416)	0.413 ± 0.023	102 ± 5	5 ± 0.7	5
2500(1416)	0.389 ± 0.028	44.5± 3.2	5 ± 0.7	5
2750(1416)	0.333 ± 0.043	19.3± 2.5	5 ± 0.7	5
3000(1416)	0.251 ± 0.053	8.0± 1.7	5 ± 0.7	5
3250(1416)	0.177 ± 0.054	3.4± 1.1	5 ± 0.7	5
3500(1416)	0.122 ± 0.046	1.6± 0.6	5 ± 0.7	5

Table 8.2.: Input parameter for limit setting with uncertainties.

8.4. Limit calculation

All parameters used for the limit setting are shown with their uncertainties in table 8.2, except the luminosity, which is 20.3 fb^{-1} with an uncertainty of 2.8%. With these parameters the calculation of the posterior probability, see equation 8.10, is performed. This is done using the official W' limit setting tool, that was used before, to produce results with 2011 data [89]. This tool provides the calculation of a limit on σB for each W' mass, based on the Bayesian approach explained in section 8.2. In the following the functionality of the tool is explained a bit more in detail.
The first step is the calculation of the likelihood $\mathcal{L}_B$ as defined in equation 8.7. Since the likelihood is a function of σB, a σB range and step size is defined to sample the likelihood. Each σB value is used together with the other input parameters to calculate one value of the likelihood function. As it was mentioned before, the uncertainties are treated as a Gaussian distribution with the mean as the parameter value and the standard deviation as the systematic uncertainty of the input parameter. In the tool this is done by multiplying the default input parameter, for example the signal efficiency, with a random number, that follows a Gaussian shape with mean one and the systematic uncertainty as standard deviation. The resulting likelihood values with these "smeared" input parameters is calculated multiple times and the mean value is taken as one point of the likelihood. This procedure is done for all σB in the "sampling range" resulting in a smooth function. In order to have the posterior probability, the likelihood values are simply multiplied by the prior probability (see equation 8.10), which is in the case of an flat prior, one.
An example for a resulting posterior probability function can be seen in figure 8.8, where the posterior is shown as a function of σB for a W' pole mass of 2750 GeV. It can be seen that it has a Gaussian like shape with the mean at zero, since the data is in this m_T region in good agreement with the background and such there is no much "room" for a signal. The 95% C.L. limit on σB can then be calculated by

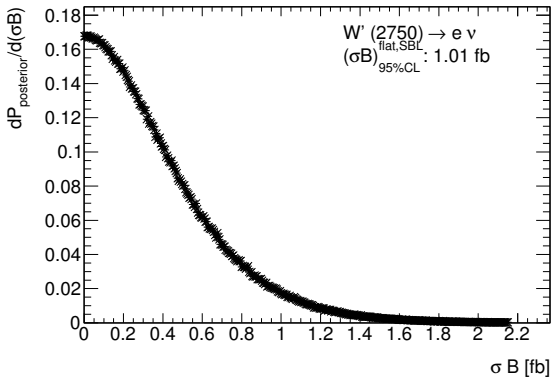

Figure 8.8.: Posterior probability as a function of σB for a W' pole mass of 2750 GeV. The shown label, $\sigma^{flat,SBL}_{95\%CL}$, indicates that the 95%C.L. on σB is estimated with a flat prior and uncertainties for the **S**ignal efficiency, **B**ackground and **L**uminosity (SBL).

integrating from 0 to higher σB, until the point where the integrated area is at 95% of the complete area under the function. For the shown example this is the case at 1.01 fb^{-1}. This value is then the final limit on σB for one W' pole mass and can be done for all other W' pole masses in an analog way. If this procedure is done by using the number of observed events from data, the resulting limit is called observed limit. In order to have a comparison with a limit where only background estimations are included, a so called expected limit is calculated. In principle this is done exactly the same way as described before, except that for the number of observed events, the number of expected background events is used. To estimate the uncertainty of the limit on σB, "toy Monte-Carlos" are used. They are obtained by calculating a random number following a Poisson distribution, where the mean is given by the "smeared" number of expected background events. In this context "smeared" means again the multiplication of the default number of background events with a random variable following a Gaussian distribution with mean one and the background uncertainty as standard deviation. Altogether 1000 "toy Monte-Carlos" are calculated for each W' pole mass and the mean of the resulting limit on σB is taken as default value together with the one and two σ errors as uncertainty.
In figure 8.9 the final expected and observed limits on σB are shown together with the one and two σ variations of the expected limit for all used W' pole masses. Added in this figure is also the theory prediction cross-section for a sequential standard model W'. It can be seen that for values between 600 GeV and about 1250 GeV the observed

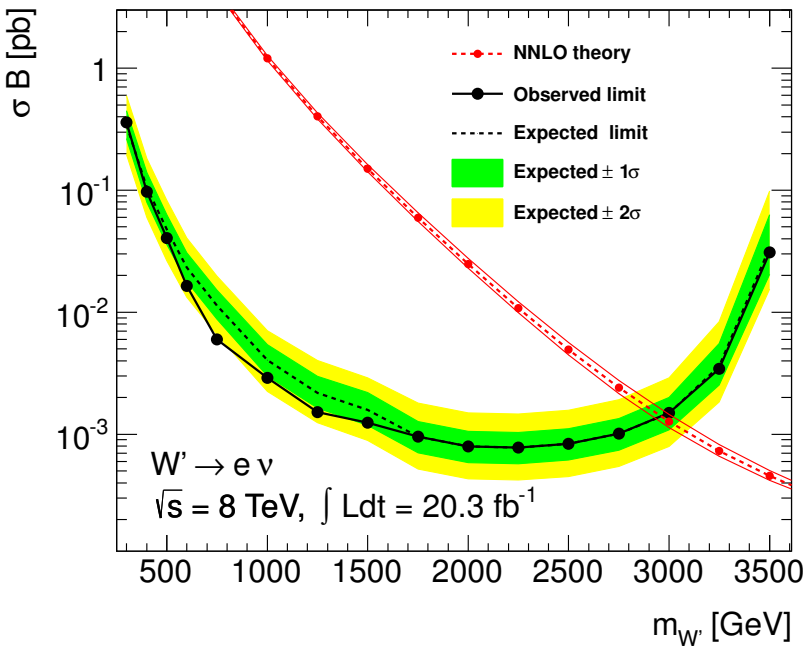

Figure 8.9.: Limit on σB as function of $m_{W'}$. The expected limit (only through SM background predictions) is shown as well as the observed limit given by data input. The theory of a hypothetical W' SSM is also shown.

limit is lower as the expected limit but still inside the 2σ band of the expected limit, except the point at a pole mass of 600 GeV. The reason for that is given by the differences seen in the m_T distribution starting at about 560 GeV (figure 8.1). Above W' pole masses of 1250 GeV, background and data are in good agreement but it has to be taken into account that there is almost no data left for these high m_T^{min} thresholds. Furthermore a strongly rising behavior of the limit distribution can be seen for pole masses above 3250 GeV, which is mainly caused from the rise of the efficiency uncertainty due to the high k-factor uncertainty and such this behavior can be seen for expected and observed limit.
In summary no significant differences between expected and observed limit can be seen. Therefore it is possible to set an exclusion limit to the mass of the SSM W' boson. This can be done by calculating the intersection point of the theory curve and the expected or observed limit curve, which leads to an observed and expected exclusion of a sequential standard model W' up to an mass of 2.97 TeV, with a credibility level of 95%.

8.4.1. Comparison with other results and outlook

The latest public ATLAS W' mass limit is done with 2011 data at $\sqrt{s} = 7$ TeV and an integrated luminosity of about 5 fb^{-1}. The resulting limit excludes SSM W'-bosons, for the electron decay channel, below 2.5 TeV [89]. Comparing this result with the calculated limit of this analysis, using 2012 data with $\sqrt{s} = 8$ TeV and 20 fb^{-1}, the mass limit is about 470 GeV higher due to the higher luminosity and center of mass energy.
Compared with the latest limit from the CMS experiment, 3.35 TeV [5], including all data from 2012 with $\sqrt{s} = 8$ TeV, the limit of this analysis is about 380 GeV lower. This is not expected, since the beam conditions during the data taking time were the same and thus the amount of data collected. In order to test if the estimated systematic uncertainties are the reason of the discrepancy, a new calculation of the expected limit is done without taking any systematic uncertainty into account. The blue line in figure 8.10 shows the result. It can be seen that it has lower values for low pole masses compared to the expected limit including all systematic uncertainties (black line), due to the background uncertainty for low pole masses. For the highest pole mass of 3500 GeV the difference between the limit without systematic uncertainty and default is about an order of magnitude. The reason why this difference is this high, even though the systematic uncertainty is "only" 35%, is given by the non-linear behavior of the limit on σB as a function of the signal efficiency uncertainty, as it is shown in figure 8.11 for a pole mass of 3500 GeV. It can be seen that the limit on σB has an almost exponential increase for uncertainties above 25%. However, the intersection point between SSM-theory and expected limit without uncertainties changes only a little, leading to a mass limit of 3.01 TeV. So the uncertainties do not explain the difference to the result of the CMS-experiment.

[5] Only electron channel

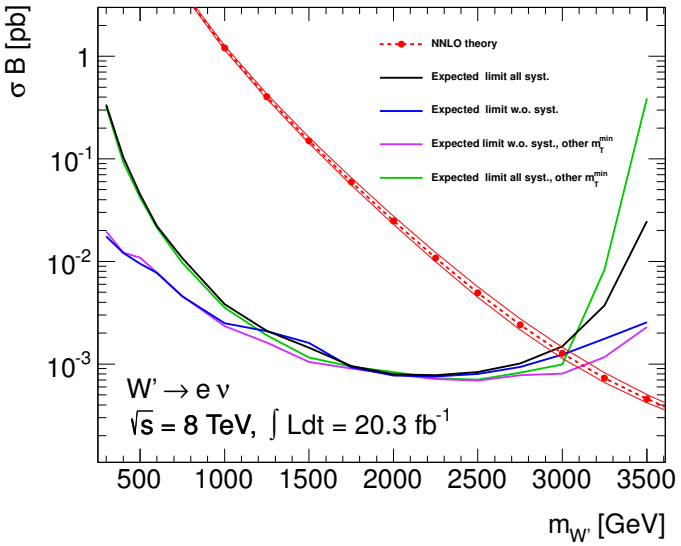

Figure 8.10.: Different expected limits on σB as function of the W' pole mass. Also shown is the NNLO theory cross-section for a hypothetical (SSM) W'. The black curve shows the expected limit including all systematic uncertainties. The blue line shows the exclusion limit without including any systematic uncertainty. The same is shown for the purple and green line, wheres for these limits a different set of m_T^{min} values is used.

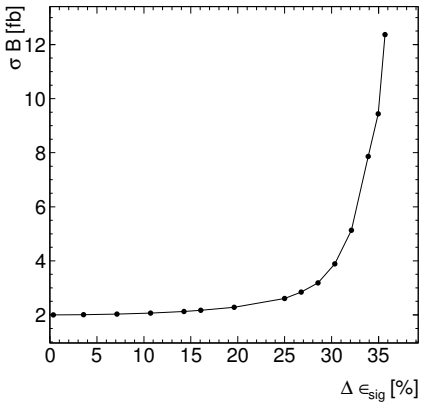

Figure 8.11.: Expected limit on σB as function of the signal efficiency uncertainty.

On selection level the CMS analysis uses an additional cut on the ratio p_T^e/E_T^{miss}, because it is expected that the momentum of the neutrino and the electron is balanced in the transverse plane. Additionally, CMS cuts also on $\Delta\varphi_{e\nu}$, which is also not done in this analysis. These two cuts would further reduce the background, mainly the QCD-background. This would lead to a statistical problem for the data-driven QCD-

background estimation[6] where a jet enriched control region is needed. Therefore these two cuts are not used for this analysis.
CMS uses also a Bayesian approach with the same method. The optimization of the m_T^{min} is in both analysis done to lead to the best expected limit on σB, as it is described in the publication of CMS including 3.7 fb^{-1} of data collected in 2012 [90]. When comparing these optimized m_T^{min} thresholds it is noticeable that for this analysis the highest m_T^{min} threshold is at 1416 GeV and for the CMS analysis it is at about 2500 GeV. There are known problems with this optimization of the m_T^{min}, that are used in this analysis and which are provided by the ATLAS W' group. In order to study the impact of changing the m_T^{min} border, the the expected limit is recalculated using recently re-optimized m_T^{min} thresholds from the muon-channel analysis group [7]. The resulting expected limit on σB as function of the W' pole masses is also shown in 8.10. Again the limits are shown with systematic uncertainties (green line) and without (blue line). For the case without uncertainties it can be seen that the mass limit is increased to 3.13 TeV compared to the limit with the other m_T^{min} threshold and no uncertainty. If the uncertainties are taken into account the limit on σB increases strongly (green line), due to the k-factor uncertainty, which is higher using the m_T^{min} thresholds from the muon-channel. Therefore the resulting mass exclusion limit is only at 3.01 TeV. It has to be taken into account, that CMS does not apply a k-factor uncertainty [8] to the signal efficiency, since the uncertainty of the signal events for a W' with a pole mass of 3 TeV and an m_T^{min} threshold of 1.5 TeV is only about 3% [90], which is significant lower than the 21% uncertainty for a 3 TeV W' with an m_T^{min} of 1.4 TeV, shown in table 8.2. Therefore it is expected that the difference in the m_T^{min} optimization and the not including k-factor uncertainty is the main reason of the difference in the mass exclusion limit.
At the moment the LHC and the ATLAS experiment are going to be upgraded. The goal is to start data taking in the beginning of 2015, with $\sqrt{s} = 13 - 14$ TeV. In figure 8.12 the ratio of the $q\bar{q}$-luminosity with 7 TeV and 14 TeV is shown as function of mass. Considering a mass of 1 TeV, it can be seen that the $q\bar{q}$-luminosity, and thus the cross-section[9], will rise about a factor of five. This means, that it is possible to observe five times more events at a mass of 1 TeV, when increasing $\sqrt{s}$ from 7 TeV to 14 TeV by recording the same amount of data. The ratio of the gluon-gluon luminosity, also given in figure 8.12, shows, that the cross-section for processes from gluon-gluon annihilation will rise with an approximate factor of 12. Therefore the $t\bar{t}$-background and to some degree also the QCD-background will increase stronger for higher $\sqrt{s}$ than the other backgrounds, since these two background can be produced via gg-annihilation, whereas the others can not. That is why it might be important

[6] CMS uses Monte-Carlo simulation for the QCD-background and therefore are able to apply these cuts.
[7] A list of these thresholds is given in the appendix A.1
[8] Referring to the publication [90] they only include electron and E_T^{miss} energy scale and resolution uncertainties.
[9] If only processes with quark and antiquarks in the initial state are considered, like the W-boson production.

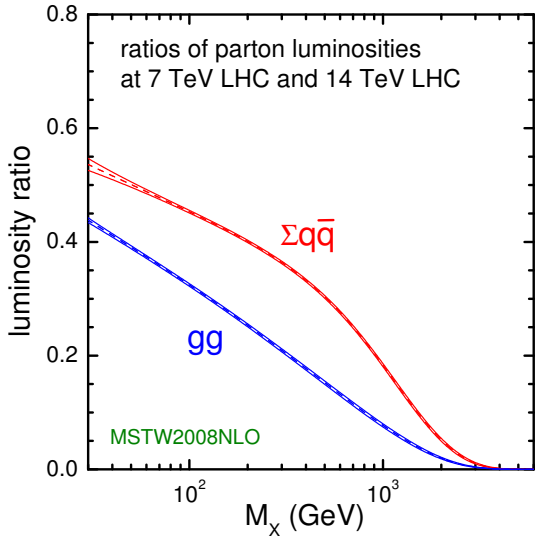

Figure 8.12.: Quark antiquark, as well as gluon-gluon luminosity with 7 TeV divided by the luminosity with 14 TeV as a function of mass [91].

to apply further selection criteria to reduce top and QCD-background.

The impact of a higher center of mass energy on the mass limit is investigated via simulations [92]. It is shown, that the expected mass limit of a hypothetical SSM Z' (the neutral partner of the SSM W') can be increased from currently 2.79 TeV ($\sqrt{s}$ = 8 TeV [93], $\int \mathcal{L}$=20 fb^{-1}) to 6.5 TeV, assuming a center of mass energy of $\sqrt{s}$ = 14 TeV and an integrated luminosity of 300 fb^{-1}.

9. Conclusion

At the moment the Standard Model of particle physics is the best description for the fundamental structure of matter. It also describes the interaction between the elementary constituents of particles. Predictions, that are based on the Standard Model (SM), are tested to high precision and so far no deviation is found. However, the standard model leaves some open questions. One of these open questions is the unification of the strong force with the other two forces, analogue to the electro-weak unification. Some of these theories predict new, heavy, charged gauge bosons beyond the, up to now investigated, energy scale. Regarding to the "sequential standard model" (SSM) this charged boson has the same charge, spin and other quantum numbers as the SM W boson, except of a higher mass. It is also predicted to have the same couplings as the W-bosons, but a potential interference between the W and the hypothetical W' is not taken into account in this theory.
This thesis presented a search of a W'-boson by looking for resonance-like differences between SM background and data in the transverse mass distribution. The analysed data, from proton-proton collisions, were taken with the ATLAS-detector at $\sqrt{s} = 8$ TeV and an integrated luminosity of 20 fb^{-1}. The focus was set on the decay of a hypothetical W' into an electron and neutrino. The background of Standard Model processes was split into two different sources. On the one hand there is background from real electrons, that was determined with Monte-Carlo simulations and on the other hand there is background from other objects, e.g. jets, that fake electrons and thus pass the selection, which was estimated by using the data-driven matrix method.
The Monte-Carlo samples used were produced with two different methods of detector simulation. Samples using these different methods were compared and differences in the shower shape, isolation and resolution were found. The impact of differences in the shower shape on the selection were about 0.1% and therefore neglectable for this analysis. Differences in the isolation were minimized by applying correction factors. Differences in the resolution were covered by systematic variations of one simulation and therefore no further corrections were applied.
A detailed comparison between data and background estimation was performed and no significant differences were observed. Therefore an exclusion limit on cross-section times branching ratio (σB) of a SSM W' was set for several W' pole masses, using a Bayesian method. For each pole mass the number of observed and background events where calculated by integration from a certain m_T thresholds (m_T^{min}). Comparing these numbers with the number of expected (signal + background)events, a limit on σB, with a 95% C.L., was set for each investigated W' pole mass. The resulting observed and expected mass limit is 2.97 TeV. Compared to previous ATLAS results, done with $\sqrt{s} = 7$ TeV data and an integrated luminosity of 4.7 fb^{-1} [89], the limit

was increased about 470 GeV due to the higher center of mass energy and luminosity. The comparison with results from CMS [36] shows that the mass limit, estimated in this thesis, is about 300 GeV lower for the electron channel. This differences can probably be reduced to some improvements of the analysis, that are listed in the following.
It might be necessary to re-optimize the m_T^{min} thresholds, used for the integration to calculate the number of observed and background events. It was shown, that a different set of m_T^{min} thresholds leads to better results, if no systematic uncertainty is taken into account. Including the systematic uncertainties, the limit on σB gets significant higher for high pole masses, leading to a lower mass exclusion limit. Therefore it is to consider if it might be necessary to use a complete different method for the limit setting, which is not as sensitive to the uncertainties as the method presented in this thesis.
Additional room for improvements, that do not directly influence the mass exclusion limit, was seen in the p_T^W distribution. It has been shown that there are differences between background and data in the shape of the transverse momentum of the reconstructed W-boson, which are most likely caused by mismodelings in the W Monte-Carlo samples. Also the background from diboson events seem to have a wrong modeling of the transverse momentum. Currently ongoing studies give first indications that there are differences in the p_T shape for different generators. A further improvement can be achieved if the background distributions are extrapolated with fits to higher m_T, not to suffer from low statistics of the Monte-Carlo samples. Also a different method for the estimation of the fake rates, needed for the QCD-background, would be good, in order to have an estimate of the uncertainty due to different methods.

Currently an upgrade of the LHC and the ATLAS-detector is in progress. It is planned to start data taking in 2015 with a center of mass energy of 13 to 14 TeV. With these energies it is possible to reach higher cross-sections and thus populate higher transverse masses. Due to a different behavior for the gg- and $q\bar{q}$ luminosity for higher $\sqrt{s}$ it might be necessary to introduce additional selection criteria to reduce the $t\bar{t}$-background. Nevertheless due to higher reachable transverse masses the exclusion limit will increase significantly or a new heavy, charged vector boson will be found.

A. Appendix

In order to get transverse mass distributions for a W' with a certain pole mass out of the flat simulated distribution, weights ($f_{rew}(m_{flat}, m_{pole})$) are used, which can be calculated in the following way.

$$w = \frac{1 \cdot 10^{-12}}{(m_{flat}^2 - m_{pole}^2)^2 + (m_{pole}^2 \cdot \Gamma)^2} \,, \tag{A.1}$$

$$\text{with: } \Gamma = 0.0095 \cdot (3 + (1 + 0.5 \cdot m_{rel}) \cdot (1 - m_{rel})^2) \,, \tag{A.2}$$

$$\text{with: } m_{rel} = \left(\frac{174.3 \text{ GeV}}{m_{pole}}\right)^2 \tag{A.3}$$

$$m_{flat}^{norm} = \frac{m_{rel}}{8000} \tag{A.4}$$

$$\Rightarrow f_{rew}(m_{flat}, m_{pole}) = \begin{cases} m_{flat}^{norm} < 0.0375 \ : & \frac{w}{121.88 \exp(13 \cdot m_{flat}^{norm})} \\ m_{flat}^{norm} > 0.0375 \ : & \frac{w}{\exp(18.5 \cdot m_{flat}^{norm} - 1.4 \log(m_{flat}^{norm}))} \end{cases} \tag{A.5}$$

$$\text{with: } m_{flat}^{norm} = m_{flat}/8000 \,, \tag{A.6}$$

where m_{pole} is the pole mass of the W' and m_{flat} the mass of the flat sample.

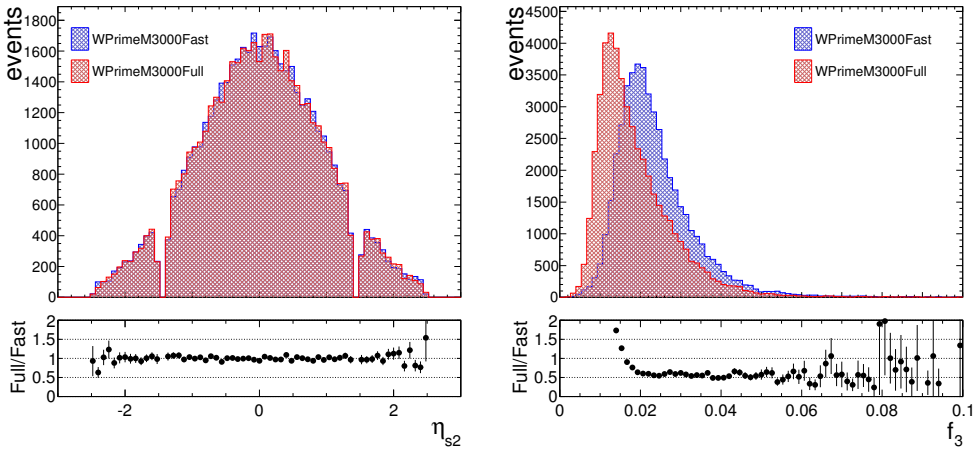

Figure A.1.: Comparison of η_{S2} and f_3 between fast simulation and full simulation for the W' (3 TeV) signal sample.

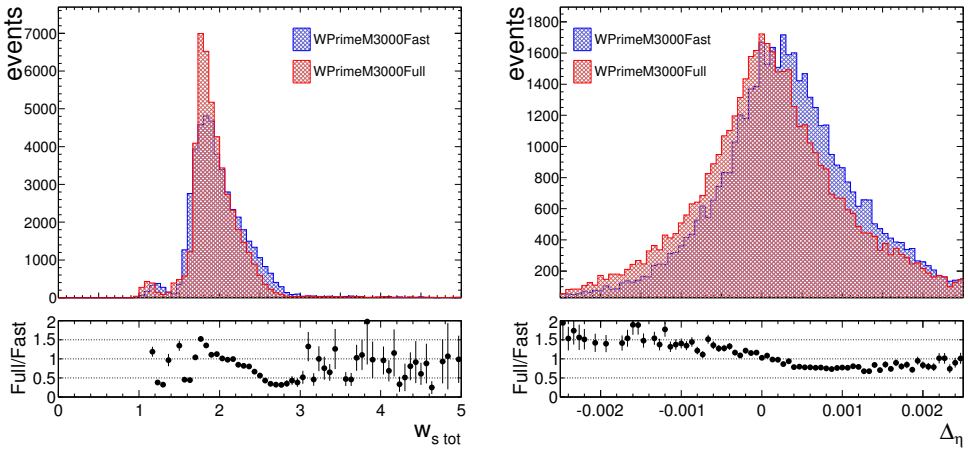

Figure A.2.: Comparison of $w_{s\,tot}$ and Δ_η between fast simulation and full simulation for the W' (3 TeV) signal sample.

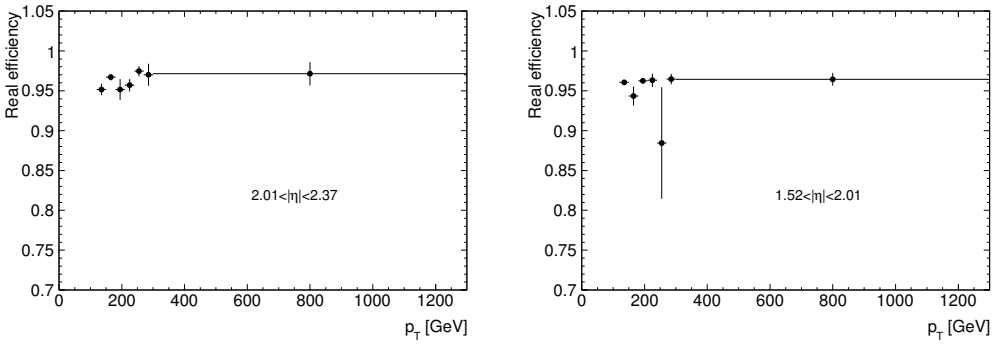

Figure A.3.: Real efficiency as a function of p_T for two of the four η bins; determined from W Monte-Carlo samples.

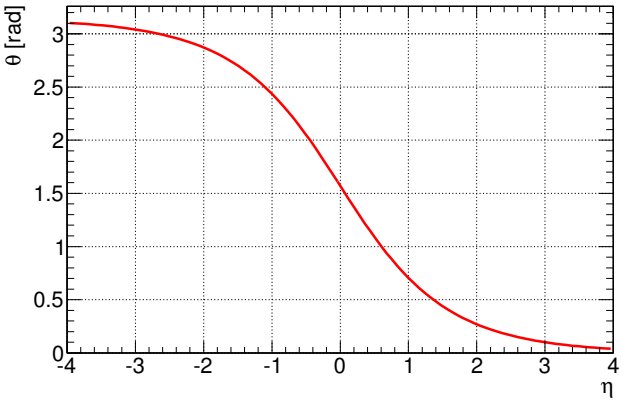

Figure A.4.: θ dependence of η.

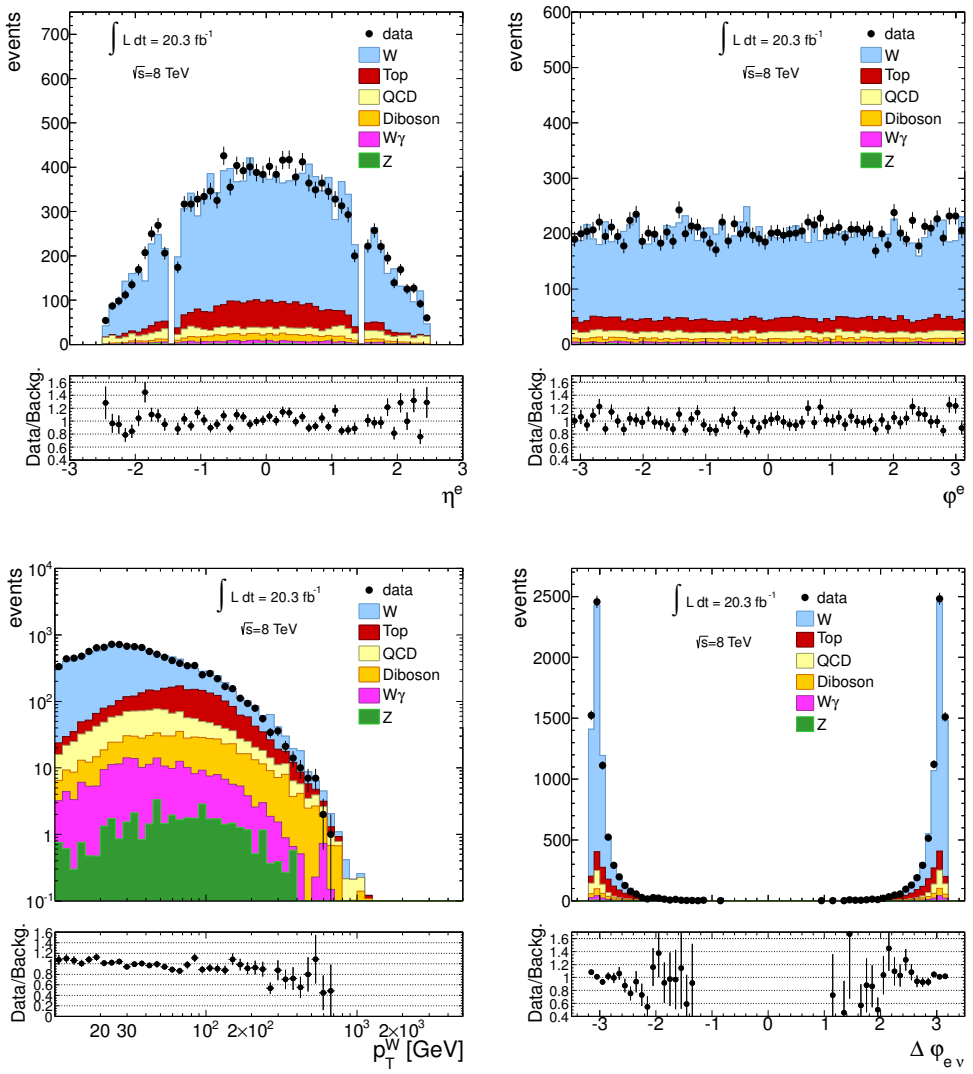

Figure A.5.: Comparison of data and background distributions for different kinematic distributions, as well as their ratios.

$m(W')$	300	400	500	600	750	1000	1250	1500	1750
m_T^{min}	267	336	423	502	597	796	1002	1191	1337
$m(W')$	2000	2250	2500	2750	3000	3250	3500		
m_T^{min}	1337	1783	1783	1783	1888	1888	1783		

Table A.1.: Re-optimized m_T^{min} thresholds from the analyse group of the muon channel.

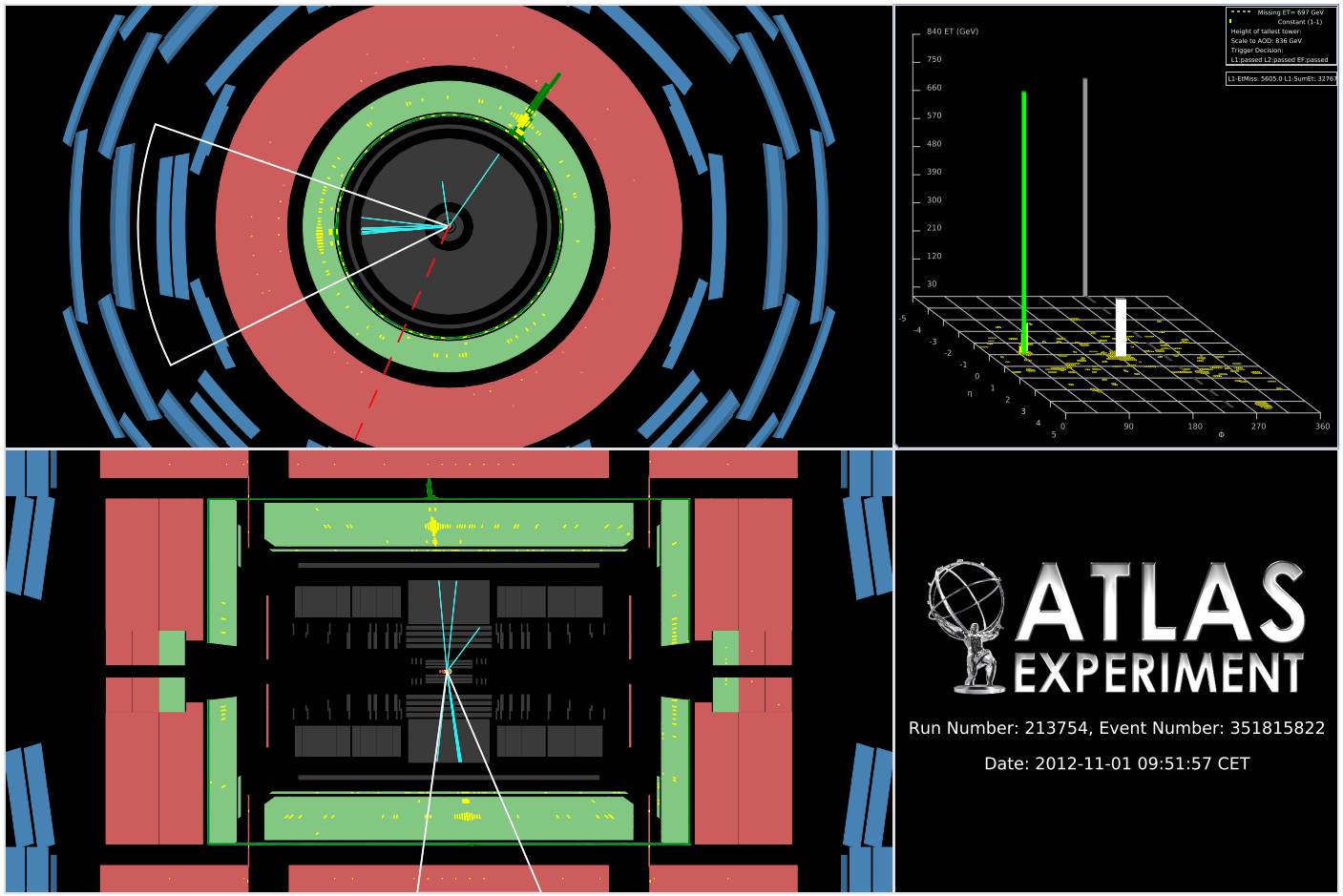

Figure A.6.: Event display of an event with $m_T = 1551.46$ GeV, created with ATLANTIS [94]. All tracks above 5 GeV are shown. It can be seen that the electron (track marked in blue) has an high energy deposition in the electromagnetic calorimeter. The missing transverse energy is visible at the opposite direction. Also it can be seen that the decay of the W-boson is not exact back to back, which indicates a boost of the W-boson. Due to momentum conversation also a recoil jet (marked as a white cone) occurs.

$m_{W'}$ [GeV]	observed limit [pb]	exp. limit -2σ [pb]	exp. limit -1σ [pb]	exp. limit [pb]	exp. Limit +1σ [pb]	exp. Limit +2σ [pb]
300	$3.59 \cdot 10^{-1}$	$1.97 \cdot 10^{-1}$	$2.65 \cdot 10^{-1}$	$3.42 \cdot 10^{-1}$	$4.50 \cdot 10^{-1}$	$5.98 \cdot 10^{-1}$
400	$9.74 \cdot 10^{-2}$	$5.99 \cdot 10^{-2}$	$7.99 \cdot 10^{-2}$	$1.05 \cdot 10^{-1}$	$1.40 \cdot 10^{-1}$	$1.81 \cdot 10^{-1}$
500	$4.07 \cdot 10^{-2}$	$2.64 \cdot 10^{-2}$	$3.59 \cdot 10^{-2}$	$4.78 \cdot 10^{-2}$	$6.30 \cdot 10^{-2}$	$8.26 \cdot 10^{-2}$
600	$1.64 \cdot 10^{-2}$	$1.32 \cdot 10^{-2}$	$1.78 \cdot 10^{-2}$	$2.34 \cdot 10^{-2}$	$3.08 \cdot 10^{-2}$	$4.06 \cdot 10^{-2}$
750	$6.00 \cdot 10^{-3}$	$6.55 \cdot 10^{-3}$	$8.77 \cdot 10^{-3}$	$1.14 \cdot 10^{-2}$	$1.51 \cdot 10^{-2}$	$1.98 \cdot 10^{-2}$
1000	$2.90 \cdot 10^{-3}$	$2.24 \cdot 10^{-3}$	$3.00 \cdot 10^{-3}$	$4.04 \cdot 10^{-3}$	$5.42 \cdot 10^{-3}$	$7.03 \cdot 10^{-3}$
1250	$1.52 \cdot 10^{-3}$	$1.24 \cdot 10^{-3}$	$1.65 \cdot 10^{-3}$	$2.19 \cdot 10^{-3}$	$2.98 \cdot 10^{-3}$	$4.03 \cdot 10^{-3}$
1500	$0.13 \cdot 10^{-4}$	$8.93 \cdot 10^{-4}$	$1.19 \cdot 10^{-3}$	$1.59 \cdot 10^{-3}$	$2.20 \cdot 10^{-3}$	$2.90 \cdot 10^{-3}$
1750	$9.58 \cdot 10^{-4}$	$5.17 \cdot 10^{-4}$	$7.05 \cdot 10^{-4}$	$9.58 \cdot 10^{-4}$	$1.27 \cdot 10^{-3}$	$1.80 \cdot 10^{-3}$
2000	$7.96 \cdot 10^{-4}$	$4.30 \cdot 10^{-4}$	$5.86 \cdot 10^{-4}$	$7.96 \cdot 10^{-4}$	$1.06 \cdot 10^{-3}$	$1.49 \cdot 10^{-3}$
2250	$7.78 \cdot 10^{-4}$	$4.20 \cdot 10^{-4}$	$5.73 \cdot 10^{-4}$	$7.79 \cdot 10^{-4}$	$1.03 \cdot 10^{-3}$	$1.46 \cdot 10^{-3}$
2500	$8.34 \cdot 10^{-4}$	$4.50 \cdot 10^{-4}$	$6.14 \cdot 10^{-4}$	$8.34 \cdot 10^{-4}$	$1.11 \cdot 10^{-3}$	$1.57 \cdot 10^{-3}$
2750	$1.01 \cdot 10^{-3}$	$5.43 \cdot 10^{-4}$	$7.42 \cdot 10^{-4}$	$1.01 \cdot 10^{-3}$	$1.34 \cdot 10^{-3}$	$1.92 \cdot 10^{-3}$
3000	$1.49 \cdot 10^{-3}$	$7.94 \cdot 10^{-4}$	$1.09 \cdot 10^{-3}$	$1.49 \cdot 10^{-3}$	$2.01 \cdot 10^{-3}$	$2.90 \cdot 10^{-3}$
3250	$3.43 \cdot 10^{-3}$	$1.84 \cdot 10^{-3}$	$2.54 \cdot 10^{-3}$	$3.62 \cdot 10^{-3}$	$5.53 \cdot 10^{-3}$	$8.35 \cdot 10^{-3}$
3500	$3.09 \cdot 10^{-2}$	$1.56 \cdot 10^{-2}$	$2.05 \cdot 10^{-2}$	$3.38 \cdot 10^{-2}$	$6.28 \cdot 10^{-2}$	$9.86 \cdot 10^{-2}$

Table A.2.: Observed and expected limit on σB. Also added is the one and two σ uncertainty of the expected limit.

Bibliography

[1] J. W. v. Goethe, *Faust. Der Tragoedie erster Teil, V. 382 f.*
Reclam.
Translation from: `http://www.poetryintranslation.com/PITBR/German/FaustIScenesItoIII.htm`.

[2] F. Halzen and A. Martin, *Quarks and leptons: an introductory course in modern particle physics.*
Wiley, 1984.

[3] M. Fukugita, M. Tanimoto, and T. Yanagida, *Atmospheric neutrino oscillation and a phenomenological lepton mass matrix*, Phys.Rev. **D57** (1998) 4429–4432, `arXiv:hep-ph/9709388 [hep-ph]`.

[4] Particle Data Group Collaboration, J. Beringer et al., *Review of Particle Physics (RPP)*, Phys.Rev. **D86** (2012) 010001.

[5] R. P. Feynman, *The Theory of Positrons*, Phys. Rev. **76** (1949) .

[6] S. Weinberg, *A Model of Leptons*, Phys.Rev.Lett. **19** (1967) 1264–1266.

[7] Wu, C. S. and Ambler, E. and Hayward, R. W. and Hoppes, D. D. and Hudson, R. P., *Experimental Test of Parity Conservation in Beta Decay*, Phys. Rev. **105** (1957) 1413–1415.
`http://link.aps.org/doi/10.1103/PhysRev.105.1413`.

[8] D. Griffiths, *Introduction to Elementary Particles.*
Wiley, New York, 2008.

[9] W. Hollik, *Electroweak theory*, J.Phys.Conf.Ser. **53** (2006) 7–43.

[10] P. W. Higgs, *Broken symmetries, massless particles and gauge fields*, Phys.Lett. **12** (1964) 132–133.

[11] ATLAS Collaboration, G. Aad et al., *Observation of a new particle in the search for the Standard Model Higgs boson with the ATLAS detector at the LHC*, Phys.Lett. **B716** (2012) 1–29, `arXiv:1207.7214 [hep-ex]`.

[12] CMS Collaboration Collaboration, S. Chatrchyan et al., *Observation of a new boson at a mass of 125 GeV with the CMS experiment at the LHC*, Phys.Lett. **B716** (2012) 30–61, `arXiv:1207.7235 [hep-ex]`.

[13] M. Woods, *Review of weak mixing angle results at SLC and LEP*, .

[14] H. Yukawa, *Quantum Theory of Non-Local Fields. Part I. Free Fields*, Phys. Rev. **77** (1950) 219–226.
`http://link.aps.org/doi/10.1103/PhysRev.77.219`.

[15] A. Pich, *Quantum chromodynamics*, arXiv:hep-ph/9505231 [hep-ph].

[16] G. 't Hooft and M. Veltman, *Regularization and renormalization of gauge fields*, Nuclear Physics B **44** (1972) no. 1, 189–213. http://www.sciencedirect.com/science/article/pii/0550321372902799.

[17] QCDSF-UKQCD Collaboration, Göckeler, M. and Horsley, R. and Irving, A. C. and Pleiter, D. and Rakow, P. E. L. and Schierholz, G. and Stüben, H., *Determination of the Lambda parameter from full lattice QCD*, Phys. Rev. D **73** (2006) 014513. http://link.aps.org/doi/10.1103/PhysRevD.73.014513.

[18] J. M. Campbell, J. Huston, and W. Stirling, *Hard Interactions of Quarks and Gluons: A Primer for LHC Physics*, Rept.Prog.Phys. **70** (2007) 89, arXiv:hep-ph/0611148 [hep-ph].

[19] S. Drell and T.-M. Yan, *Partons and their Applications at High-Energies*, Annals Phys. **66** (1971) 578.

[20] G. Altarelli and G. Parisi, *Asymptotic Freedom in Parton Language*, Nucl.Phys. **B126** (1977) 298.

[21] Y. L. Dokshitzer, *Calculation of the Structure Functions for Deep Inelastic Scattering and e+ e- Annihilation by Perturbation Theory in Quantum Chromodynamics.*, Sov.Phys.JETP **46** (1977) 641–653.

[22] V. Gribov and L. Lipatov, *Deep inelastic e p scattering in perturbation theory*, Sov.J.Nucl.Phys. **15** (1972) 438–450.

[23] H1 Collaboration Collaboration, C. Adloff et al., *Measurement of neutral and charged current cross-sections in positron proton collisions at large momentum transfer*, Eur.Phys.J. **C13** (2000) 609–639, arXiv:hep-ex/9908059 [hep-ex].

[24] ZEUS Collaboration Collaboration, S. Chekanov et al., *Measurement of the neutral current cross-section and F(2) structure function for deep inelastic e + p scattering at HERA*, Eur.Phys.J. **C21** (2001) 443–471, arXiv:hep-ex/0105090 [hep-ex].

[25] Lai, H. L. and Huston, J. and Kuhlmann, S. and Olness, F. and Owens, J. and Soper, D. and Tung, W. K. and Weerts, H., *Improved parton distributions from global analysis of recent deep inelastic scattering and inclusive jet data*, Phys. Rev. D **55** (1997) 1280–1296. http://link.aps.org/doi/10.1103/PhysRevD.55.1280.

[26] S. Forte and G. Watt, *Progress in the Determination of the Partonic Structure of the Proton*, arXiv:1301.6754 [hep-ph].

[27] H.-L. Lai, M. Guzzi, J. Huston, Z. Li, P. M. Nadolsky, et al., *New parton distributions for collider physics*, Phys.Rev. **D82** (2010) 074024, arXiv:1007.2241 [hep-ph].

[28] J. Pumplin, D. Stump, R. Brock, D. Casey, J. Huston, et al., *Uncertainties of predictions from parton distribution functions. 2. The Hessian method*, Phys.Rev. **D65** (2001) 014013, arXiv:hep-ph/0101032 [hep-ph].

[29] C. Berger, *Elementarteilchenphysik*. Springer, 2006.

[30] P. Langacker, R. W. Robinett, and J. L. Rosner, *New heavy gauge bosons in* pp *and* $p\bar{p}$ *collisions*, Phys. Rev. D **30** (1984) 1470–1487. http://link.aps.org/doi/10.1103/PhysRevD.30.1470.

[31] S. J. Huber, C.-A. Lee, and Q. Shafi, *Kaluza-Klein excitations of W and Z at the LHC?*, Phys.Lett. **B531** (2002) 112–118, arXiv:hep-ph/0111465 [hep-ph].

[32] G. Altarelli, B. Mele, and M. Ruiz-Altaba, *SEARCHING FOR NEW HEAVY VECTOR BOSONS IN p anti-p COLLIDERS*, Z.Phys. **C45** (1989) 109.

[33] CDF Collaboration Collaboration, T. Aaltonen et al., *Search for a New Heavy Gauge Boson W' with Electron + missing ET Event Signature in $p\bar{p}$ collisions at $\sqrt{s} = 1.96$ TeV*, Phys.Rev. **D83** (2011) 031102, arXiv:1012.5145 [hep-ex].

[34] D0 Collaboration Collaboration, V. Abazov et al., *Search for W' bosons decaying to an electron and a neutrino with the D0 detector*, Phys.Rev.Lett. **100** (2008) 031804, arXiv:0710.2966 [hep-ex].

[35] *ATLAS search for a heavy gauge boson decaying to a charged lepton and a neutrino in* 4.7 fb^{-1} *of pp collisions at* $\sqrt{s} = 7$ TeV, Tech. Rep. ATLAS-CONF-2012-086, CERN, Geneva, Jul, 2012.

[36] CMS Collaboration, *Search for new physics in the final states with a lepton and missing transverse energy at sqrts = 8 TeV*, https://twiki.cern.ch/twiki/bin/view/CMSPublic/PhysicsResultsEXO12060, Mar., 2013.

[37] L. Evans and P. Bryant, *LHC Machine*, Journal of Instrumentation **3** (2008) no. 08, S08001. http://stacks.iop.org/1748-0221/3/i=08/a=S08001.

[38] S. Holmes, R. S. Moore, and V. Shiltsev, *Overview of the Tevatron collider complex: goals, operations and performance*, Journal of Instrumentation **6** (2011) no. 08, T08001. http://stacks.iop.org/1748-0221/6/i=08/a=T08001.

[39] V. Balagura, *Notes on van der Meer Scan for Absolute Luminosity Measurement*, Nucl.Instrum.Meth. **A654** (2011) 634–638, arXiv:1103.1129 [physics.ins-det].

[40] ATLAS Collaboration, G. Aad et al., *The ATLAS Experiment at the CERN Large Hadron Collider*, JINST **3** (2008) S08003.

[41] *ATLAS magnet system: Technical Design Report, 1.*
Technical Design Report ATLAS. CERN, Geneva, 1997.

[42] J. P. Badiou, J. Beltramelli, J. M. Maze, and J. Belorgey, *ATLAS barrel toroid: Technical Design Report.*
Technical Design Report ATLAS. CERN, Geneva, 1997.
Electronic version not available.

[43] *ATLAS end-cap toroids: Technical Design Report.*
Technical Design Report ATLAS. CERN, Geneva, 1997.
Electronic version not available.

[44] *ATLAS muon spectrometer: Technical Design Report.*
Technical Design Report ATLAS. CERN, Geneva, 1997.
distribution.

[45] A. Salvucci, *Measurement of muon momentum resolution of the ATLAS detector*, `arXiv:1201.4704`.

[46] *ATLAS level-1 trigger: Technical Design Report.*
Technical Design Report ATLAS. CERN, Geneva, 1998.

[47] I. Bird, K. Bos, N. Brook, D. Duellmann, C. Eck, et al., *LHC computing Grid. Technical design report*, .

[48] R. Jones, *ATLAS computing and the GRID*, Nucl.Instrum.Meth. **A502** (2003) 372–375.

[49] R. Brun and F. Rademakers, *ROOT: An object oriented data analysis framework*, Nucl.Instrum.Meth. **A389** (1997) 81–86.

[50] *Electron and photon reconstruction and identification in ATLAS: expected performance at high energy and results at 900 GeV*, Tech. Rep. ATLAS-CONF-2010-005, CERN, Geneva, Jun, 2010.

[51] ATLAS Collaboration, G. Aad et al., *Expected Performance of the ATLAS Experiment - Detector, Trigger and Physics*, `arXiv:0901.0512 [hep-ex]`.

[52] Electron performance group, *Egamma2012Analyses*, `https://twiki.cern.ch/twiki/bin/viewauth~/AtlasProtected/Egamma2012Analyses`.

[53] W. Lampl, S. Laplace, D. Lelas, P. Loch, H. Ma, S. Menke, S. Rajagopalan, D. Rousseau, S. Snyder, and G. Unal, *Calorimeter Clustering Algorithms: Description and Performance*, Tech. Rep. ATL-LARG-PUB-2008-002. ATL-COM-LARG-2008-003, CERN, Geneva, Apr, 2008.

[54] M. Cacciari, G. P. Salam, and G. Soyez, *The Anti-k(t) jet clustering algorithm*, JHEP **0804** (2008) 063, `arXiv:0802.1189 [hep-ph]`.

[55] ATLAS Jet and Missing Et Group, *ApplyJetCalibration2012*, `https://twiki.cern.ch/twiki/bin/viewauth/~AtlasProtected/ApplyJetCalibration2012`.

[56] ATLAS Collaboration Collaboration, G. Aad et al., *Performance of Missing Transverse Momentum Reconstruction in Proton-Proton Collisions at 7 TeV with ATLAS*, Eur.Phys.J. **C72** (2012) 1844, arXiv:1108.5602 [hep-ex].

[57] *Performance of Missing Transverse Momentum Reconstruction in ATLAS studied in Proton-Proton Collisions recorded in 2012 at 8 TeV*, Tech. Rep. ATLAS-CONF-2013-082, CERN, Geneva, Aug, 2013.

[58] ATLAS Jet and Missing Et Group, *EtMissRefFinal*, https://twiki.cern.ch/twiki/bin/viewauth/~AtlasProtected/EtMissRefFinal.

[59] A. L. WG https://twiki.cern.ch/twiki/bin/view/~AtlasPublic/LuminosityPublicResults.

[60] ATLAS, *ATLAS Luminosity Calculator*, https://atlas-lumicalc.cern.ch/.

[61] ATLAS Collaboration, G. Aad et al., *Improved luminosity determination in pp collisions at sqrt(s) = 7 TeV using the ATLAS detector at the LHC*, arXiv:1302.4393 [hep-ex].

[62] Electron performance group, *Calorimeter Isolation Corrections*, https://twiki.cern.ch/twiki/bin/viewauth/AtlasProtected/CaloIsolationCorrections.

[63] M. Hance, D. Olivito, and H. Williams, *Performance Studies for e/gamma Calorimeter Isolation*, Tech. Rep. ATL-COM-PHYS-2011-1186, CERN, Geneva, Sep, 2011.

[64] T. Sjöstrand, S. Mrenna, and P. Z. Skands, *A Brief Introduction to PYTHIA 8.1*, Comput. Phys. Commun. **178** (2008) 852–867, arXiv:0710.3820 [hep-ph].

[65] S. Alioli, P. Nason, C. Oleari, and E. Re, *A general framework for implementing NLO calculations in shower Monte Carlo programs: the POWHEG BOX*, JHEP **1006** (2010) 043, arXiv:1002.2581 [hep-ph].

[66] S. Frixione and B. R. Webber, *Matching NLO QCD computations and parton shower simulations*, JHEP **0206** (2002) 029.

[67] P. Golonka and Z. Was, *PHOTOS Monte Carlo: A Precision tool for QED corrections in Z and W decays*, Eur.Phys.J. **C45** (2006) 97–107, arXiv:hep-ph/0506026 [hep-ph].

[68] GEANT4 Collaboration, S. Agostinelli et al., *GEANT4: A Simulation toolkit*, Nucl.Instrum.Meth. **A506** (2003) 250–303.

[69] W. Lukas, *Fast Simulation for ATLAS: Atlfast-II and ISF*, Tech. Rep. ATL-SOFT-PROC-2012-065, CERN, Geneva, Jun, 2012.

[70] T. Yamanaka and the ATLAS Collaboration, *The ATLAS calorimeter simulation FastCaloSim*, Journal of Physics: Conference Series **331** (2011) no. 3, 032053. http://stacks.iop.org/1742-6596/331/i=3/a=032053.

[71] T. Gleisberg, S. Hoeche, F. Krauss, M. Schonherr, S. Schumann, et al., *Event generation with SHERPA 1.1*, JHEP **0902** (2009) 007, arXiv:0811.4622 [hep-ph].

[72] J. Butterworth, J. R. Forshaw, and M. Seymour, *Multiparton interactions in photoproduction at HERA*, Z.Phys. **C72** (1996) 637–646, arXiv:hep-ph/9601371 [hep-ph].

[73] G. Corcella et al., *HERWIG 6: an event generator for hadron emission reactions with interfering gluons (including supersymmetric processes)*, JHEP **0101** (2001) 010.

[74] B. P. Kersevan and E. Richter-Was, *The Monte Carlo event generator AcerMC version 2.0 with interfaces to PYTHIA 6.2 and HERWIG 6.5*, arXiv:hep-ph/0405247 [hep-ph].

[75] J. Pumplin, D. Stump, J. Huston, H. Lai, P. M. Nadolsky, et al., *New generation of parton distributions with uncertainties from global QCD analysis*, JHEP **0207** (2002) 012, arXiv:hep-ph/0201195 [hep-ph].

[76] M. L. Mangano, M. Moretti, F. Piccinini, R. Pittau, and A. D. Polosa, *ALPGEN, a generator for hard multiparton processes in hadronic collisions*, JHEP **0307** (2003) 001, arXiv:hep-ph/0206293 [hep-ph].

[77] Physics Analysis Tools, *Pileup Reweighting*, https://twiki.cern.ch/twiki/bin/viewauth/~AtlasProtected/ExtendedPileupReweighting.

[78] *Diboson Physics Studies*, Tech. Rep. ATL-PHYS-PUB-2009-038. ATL-COM-PHYS-2009-103, CERN, Geneva, Mar, 2009.
CSC Note from SM.

[79] ATLAS Collaboration, G. Aad et al., *Search for New Particles in Two-Jet Final States in 7 TeV Proton-Proton Collisions with the ATLAS Detector at the LHC*, Phys.Rev.Lett. **105** (2010) 161801, arXiv:1008.2461 [hep-ex].

[80] Physics Analysis Tools, *Jet resolution smearing*, https://twiki.cern.ch/twiki/bin/viewauth/~AtlasProtected/ApplyJetResolutionSmearing.

[81] Alexander Long et al., *W/W' Higher Order Corrections*, Talk given within the W' group meeting on 13th of July 2013 https://indico.cern.ch/getFile.py/access?contribId=2&resId=0&materialId=slides&confId=263353.

[82] M. Cacciari, M. Czakon, M. Mangano, A. Mitov, and P. Nason, *Top-pair production at hadron colliders with next-to-next-to-leading logarithmic soft-gluon resummation*, Phys.Lett. **B710** (2012) 612–622, arXiv:1111.5869 [hep-ph].

[83] N. Kidonakis, *NNLL resummation for s-channel single top quark production*, Phys.Rev. **D81** (2010) 054028, arXiv:1001.5034 [hep-ph].

[84] N. Kidonakis, *Two-loop soft anomalous dimensions for single top quark associated production with a W- or H-*, Phys.Rev. **D82** (2010) 054018, arXiv:1005.4451 [hep-ph].

[85] ATLAS Collaboration, G. Aad et al., *Measurement of the transverse momentum distribution of Z/gamma* bosons in proton-proton collisions at* $\sqrt{s} = 7$ *TeV with the ATLAS detector*, Phys.Lett. **B705** (2011) 415–434, arXiv:1107.2381 [hep-ex].

[86] J. M. Bernardo, *Bayesian Theory*. Wiley Series in Probability and Statistics, 1994.

[87] J. Aldrich, *R. A. Fisher and the making of maximum likelihood 1912–1922*, Statist. Sci. **12** (1997) no. 3, 162–176. http://dx.doi.org/10.1214/ss/1030037906.

[88] T. Bayes, *An essay towards solving a problem in the doctrine of chances*, Phil. Trans. of the Royal Soc. of London **53** (1763) 370–418.

[89] ATLAS Collaboration Collaboration, G. Aad et al., *ATLAS search for a heavy gauge boson decaying to a charged lepton and a neutrino in pp collisions at* $\sqrt{s} = 7$ *TeV*, Eur.Phys.J. **C72** (2012) 2241, arXiv:1209.4446 [hep-ex].

[90] CMS Collaboration Collaboration, S. Chatrchyan et al., *Search for new physics in final states with a lepton and missing transverse energy in pp collisions at the LHC*, Phys.Rev. **D87** (2013) 072005, arXiv:1302.2812 [hep-ex].

[91] W. Stirling, *private communication*.

[92] T. ATLAS-Collaboration, *Physics at a High-Luminosity LHC with ATLAS*, Tech. Rep. ATL-PHYS-PUB-2012-001, CERN, Geneva, Aug, 2012.

[93] *Search for high-mass dilepton resonances in 20* fb^{-1} *of pp collisions at* $\sqrt{s} = 8$ *TeV with the ATLAS experiment*, Tech. Rep. ATLAS-CONF-2013-017, CERN, Geneva, Mar, 2013.

[94] *ATLANTIS, event display for ATLAS*, http://www.hep.ucl.ac.uk/atlas/atlantis/.

B. Danksagung

Zu Beginn möchte ich mich bei Prof. Dr. Stefan Tapprogge bedanken, der mir ermöglicht hat die Masterarbeit in der ETAP zu schreiben. Er hatte immer ein offenes Ohr für Probleme und hat mich unterstützt, wo es nur ging. Außerdem hat er mir einen Besuch am CERN, sowie die Teilnahme an der DPG ermöglicht.

Ein Dank geht auch an Prof. Dr. Wolfgang Gradl, dass er sich als Zweitgutachter für diese Arbeit bereit gestellt hat.

Besonders danken möchte ich auch Frank Ellinghaus, der nicht nur bei Problemen geholfen hat, sondern auch immer bei den Meetings dabei war und unterstützend zur Seite gestanden hat, wenn man gerade mal nicht die richtigen Worte gefunden hat.

Einen weiteren Dank möchte ich an Markus Zinser aussprechen, der mir nicht nur während meiner Masterarbeit beratend und unterstützend zur Seite gestanden hat, sondern auch während dem Studium ein Kommilitone war, mit dem man gerne, manchmal auch die ganze Nacht, lernte oder Versuchspraktika auswertete.

Ein Dank geht auch an Natascha Schuh, die mir, gerade am Anfang immer wieder erklärt hat, auf was ich bei der Analyse achten muss und meine nervigen Fragen auch nach dem hundertsten mal immer gelassen beantwortet hat.

Natürlich will ich mich auch bei meinen weiteren Büro Kollegen und allen weiteren Mitglieder der Arbeitsgruppe bedanken für die nette Atmosphäre und auch für den, manchmal nötigen, Ausgleich zum “Arbeitsalltag”.

Ein weiterer Dank geht an meine Eltern, die es mir ermöglicht haben zu studieren und mich finanziell und mental unterstützen, wo sie nur können.

Außerdem geht ein Dank an Thomas, der immer ein offenes Ohr hatte, wenn ich gerade mal absolut keine Lust mehr hatte und für den nötigen Ausgleich zum Studium gesorgt hat.

Bedanken möchte ich mich auch bei meiner Freundin, Tina, die sich sowohl um mein leibliches, als auch mentales Wohl, besonders während der intensiven Masterarbeitsphase, gesorgt und mir soviel Verständnis entgegen gebracht hat, wenn ich wegen der Masterarbeit keine Zeit für sie hatte.